Synthesis and Investigation of Boron and Vanadium based Catalysts for the Oxidative Dehydrogenation of Light Alkanes to Olefins

By

Natalie Raquel Altvater

A dissertation submitted in partial fulfillment of

the requirements for the degree of

Doctor of philosophy

(Chemical Engineering)

at the

University of Wisconsin – Madison

2023

Date of final oral examination: August 24, 2023

This dissertation is *approved* by the following members of the Final Oral Committee

Ive Hermans, Professor,	Chemical and Biological Engineering, Chemistry
James Dumesic, Professor	Chemical and Biological Engineering
Thatcher Root, Professor	Chemical and Biological Engineering
Victor Zavala, Professor	Chemical and Biological Engineering
Thomas Brunold, Professor	Chemistry

Abstract

Light olefins like ethylene and propylene are important building blocks for the chemical industry. Production of these chemicals exceeds 100 million metric tons each year, and they are used in all areas of society including automotive, medical, textile, and food packaging. These light olefins are traditionally produced via steam cracking which is an energy intensive process. The increasing availability of natural gas in the present chemical industry has shifted the feedstock for refinery processes and impacted the production volume of certain olefins, particularly propylene. As a result, there is a growing need for on-purpose propylene production methods to meet the market demands. Oxidative dehydrogenation (ODH) of propane to propylene is one potential pathway for increasing propylene production. Propane ODH offers lower temperature operation and does not suffer from catalyst deactivation from coke. This process still suffers from over oxidation of products and does not achieve propylene yields required for industrial implementation. Propane ODH has been studied extensively for vanadium oxide catalysts and more recently for boron-based catalysts. Despite the wealth of literature on these ODH catalyst there are still several open questions on the catalyst structure and reaction mechanisms that continue to motivate research to improve the catalytic systems. The understanding on the mechanism and structural features of boron-based has been significantly developed in recent years. This work serves to build on this knowledge and improve current knowledge on structure activity relationships for this system. Vanadium oxide catalysts have been the center of propane ODH for much longer than boron, and while literature agrees generally on the surface mechanism description of this system, there are open questions on different pathways in the mechanism and their influence on performance. The goal of this work is to show how synthesis spectroscopy, reaction engineering, and computation work combine to further the understanding of boron and vanadium oxide catalyst for propane ODH.

Acknowledgements

First and foremost, I want to thank the Lord for His strength and guidance throughout this stage of my life. My family has been the one of the greatest sources of stability and constancy throughout my academic career. No matter how near or far from home I find myself, I can always count on my parents, Dana and Ines Altvater, to show their support and pride through their prayers, encouragement, and active presence. You both instilled in me the importance of education and sacrificed so much for me to succeed in my academics. I hope to carry on and live up to the values you have both helped to instill in me through your examples. I want to thank my sister, Jessica, for her humor, reassurance, and baking skills that have all helped sustain me through my PhD. I am grateful to my brother, Samuel, for his friendship and dependability. Thank you to my cousin Emilia Curtis for being a familiar person so far from home and for giving me your friendship and support. To nuhkomoss, Mary Bassett, who sadly passed before my graduation, you were the first to ever plant the idea of becoming a scientist and encouraged me that it was something I was capable of achieving. When I left home for graduate school, you told me I was going on an adventure, and I wish I could share with you all that has happened and changed over the course of this adventure.

My support system would not be complete without the friends that have been with me throughout this endeavor. I am very fortunate to have met Lauren Tingley early in my undergraduate career, and I am very blessed to have your friendship and caring/sympathetic ear throughout my time in academia. Thank you to Leida Vázquez Ramos for always being there to commiserate, laugh together, and find the little joys of living in Madison and going through grad school. I appreciate Feifan for all your kindness, creativity, and the peaceful aura that you always brought. A special mention to Brian Kehoe for giving me your time and encouragement and doing

your best to make me feel at home so far from home. Thank you for being there to explore the state with me and give me a better perspective on life outside of graduate school and academia.

I am very grateful to Professor William DeSisto, from the University of Maine, for the guidance in research and academics that you provided for me. The semesters I spent in your lab were instrumental not only in introducing me to research but also developing a respect and appreciation for research. Thank you to Professor John Hwalek, from the University of Maine, for the energy and passion that you brough to every class you taught. The dedication both professors showed to individual students and their success has made an impression on me that has lasted through my graduate career and set a high standard for academic mentors.

I also owe great gratitude to the various postdoctoral researchers in the Hermans group for their guidance and encouragement. Thank you to Dr. Lesli Mark, Dr. Victor Lo, and Dr. Taekyung Ryu for all of the time and effort you put into helping me progress through graduate school, each in your own ways/capacities.

Of all my academic mentors, I want to thank Professor Ive Hermans for taking me on in your research group and providing me with the opportunity of pursuing my PhD under your guidance. I appreciate to no end your intellect and insight that you pour into your research. You gave me a perspective on not only the methods of research but also on the academic and industrial spheres at large. While in your group was placed in the very valuable position of having independence to grow as a researcher and develop skills as a mentor and collaborator in a pure research setting. I also want to thank you for the understanding and support you gave me during more challenging and uncertain times of my PhD that were influenced by factors outside of our control. I hope to further develop the positive attributes I learned under your instruction.

I am very fortunate to have been in such a friendly and supportive work environment, and I credit the environment to each individual that I had the opportunity to work with in the Hermans group. You all have been my greatest source of growth and opportunity for learning and expanding my abilities as a scientist. Thank you to Dr. Alyssa Love, Dr. Juan Venegas, Dr. Sarah Specht, and Dr. Shao-Chun Wang for serving as mentors and examples of scientific integrity and ingenuity. Thank you to Dr. Theodore Agbi and Dr. Son Dong for being not only peers through classes and lab work but also friends who were always there to exchange stories. Thank you to Jacob Jansen, Abdullah Al Abdulghani, Unni Kurumbail and Dr. Melissa Cendejas for your comradery and scientific knowledge that you were always willing to share. This group has been more than just a place of work and for that I am very grateful to all the group members. I cannot wait to see what dreams and paths you all continue to follow and have no doubts that you will all find success in whatever you pursue.

I also what to thank the various University of Wisconsin staff that provided their expertise and support. Thank you to Tracy Drier, Steve Myers, and Blaise Thompson for all your help with designing, building, and fixing various equipment and components of equipment that were vital to my research progress. I am grateful to Jeff Nielsen for your dedication to keeping the Chemistry building open and operational under safe working conditions. Thank you to Kate Fanis and Kelly Burton for your support and understanding through the different steps of my PhD program. The sympathy and genuine concern in addition to the practical help in meeting milestones and navigating the graduate school process.

I also want to thank my various funding sources that have made it possible for me to pursue this research. The fellowship opportunity for the Graduate Engineering Research Scholars was invaluable to my funding, and the associated community has been a great source of comradery.

Table of contents

List of Figures

List of Schemes

List of Tables

Chapter 1: Introduction to the Oxidative dehydrogenation of propane as a route for the direct production of propylene.

1.1 The importance of on purpose propylene production in the chemical industry

The modern chemical industry provides commodities for numerous branches of society including but not limited to medical, automotive, food packaging, and electronics.[1] The energy field which impacts all areas of society is dependent on a narrow range of petrochemical feedstocks as is the chemical industry. The chemical landscape has shifted over the years to change the dominant feedstock, (coal, oil, natural gas) but the demand for commodities and fuels has only increased. The United States chemical industry specifically is a $486 billion operation that supports approximately 25% of the total U.S. gross domestic product (GDP) 2022.[1] The U.S. chemical industry is the world's second largest chemical producer accounting for 13% of the world's chemicals.[1] Oil and more recently shale gas are the major feed stock sources for the chemical indistry.[2] These sources are then sequentially upgraded to commodity and specialty chemicals that are applied to the wide variety of sectors mentioned previously.[3–5]

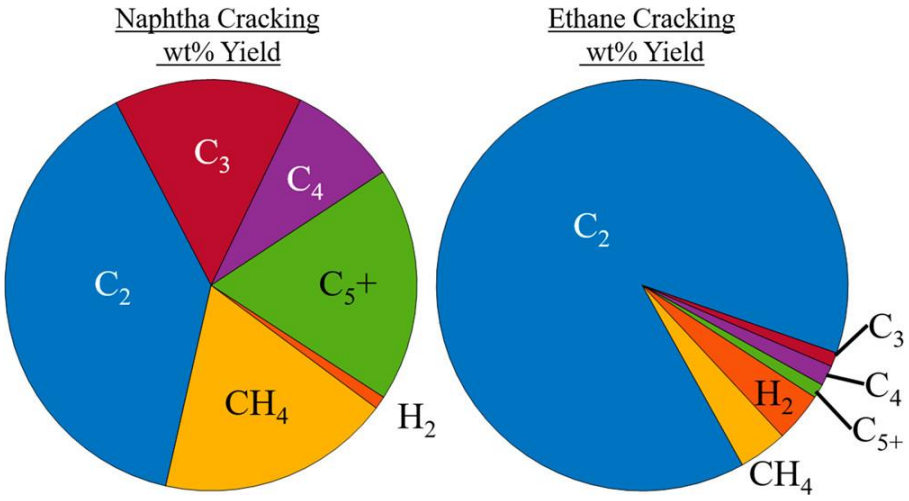

Figure 1.1 Product distribution for naphtha cracking and ethane cracking showing the difference in C_2 production depending on feedstock choice. [6,7]

Short chain alkanes ($<C_5$) are highly versatile chemicals that serve as these key building blocks in the chemical industry. The ability to upgrade these chemicals in the most efficient and economical way possible is of great interest to the scientific community related to the chemical industry.[8] Propane and its subsequent transformation to propylene is one of these important chemicals. Propylene is the second most produced chemical by volume, next to ethylene.[7] It is most converted to polypropylene and is used in a variety of industries including automotive, textile, construction, and packaging. [9,10] Propylene has traditionally been produced as a secondary product during the steam cracking of the naphtha fraction of crude oil for the production of ethylene.[11,12] With the increasing availability of shale gas, which has become a more economical feedstock due to its abundance, ethylene production has shifted to use this feedstock causing in turn a decrease in propylene production.[2,13] The difference in product distribution can be seen in Figure 1.1 Consequently, a "propylene gap" has been growing and is projected to increase in the following years as illustrated in Figure 1.2.[12,14] As a result of this projection, on-purpose propylene production is gaining interest on a global scale to meet the rising consumer demand.

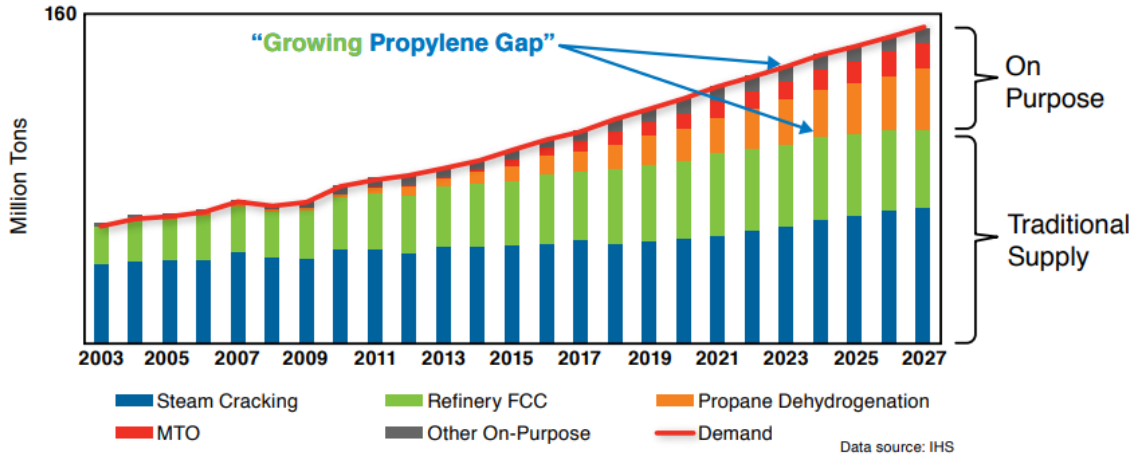

Figure 1.2 Global propylene production showing the growing change in the traditional supply and projected propylene gap. [14]

While alternatives production methods for chemical feedstocks that do not use fossil fuels are constantly being theorized or investigated, the current market and growing demand is sustained by the petroleum industry. The recent abundance of natural gas, or shale gas, has impacted propylene production. [2] This fuel source offers an abundant and inexpensive feedstock for direct production of propylene to fill the growing production gap. Currently, direct non-oxidative dehydrogenation (DH) of propane is the primary method of direct on-purpose propylene production in industry.[10,15] The other well studied method for direct propylene production is oxidative dehydrogenation (ODH) of propane.[5]

1.2 Oxidative and non-oxidative dehydrogenation of propane to propylene

Propane DH is industrially implemented via the Lummus Catofin, STAR, and UOP Oleflex processes.[11,15,16] These processes can achieve 80-90% propylene selectivity at 30-40% propane conversion which makes the processes economically viable. The reaction (Reaction 1.1) is endothermic, and equilibrium limited, so it required a large energy demand.[17] The process requires heating to > 600 °C, and the catalyst which are Cr and Pt based suffer from coke deactivation that require continuous regeneration.[10,16] Propane ODH (Reaction 1.2) offers a promising alternative to propylene production.[17] This reaction is exothermic and not equilibrium limited which lowers the energy requirement. [18] The ODH process also does not suffer from coke deactivation or need to be regenerated. The major drawback is the overoxidation of propylene to combustion products at high conversions. These combustion products, CO and CO_2 (CO_x) are more thermodynamically stable than the alkene product.[16] Both gas phase processes have been traditionally studied using metal oxide heterogeneous catalysts. Vanadium oxide catalysts and boron-based catalysts are two heavily investigated catalysts for the ODH of propane.

$$C_3H_8 \rightleftharpoons C_2H_6 + H_2 \qquad 124 \text{ kJ/mol} \qquad \text{Reaction 1.1}$$

$$2\ C_3H_8 + O_2 \rightarrow 2\ C_3H_6 + 2\ H_2O \qquad -236 \text{ kJ/mol} \qquad \text{Reaction 1.2}$$

1.3 Supported vanadium oxide catalyst for propane ODH

Supported vanadium oxide (VO_x) is one of the most investigated catalysts for ODH.[19] Vanadium is a relatively inexpensive materials that is a readily available transition metal used industrially for maleic and sulfuric acid production. Supported vanadium materials have a propylene selectivity of 60% at 10% propane conversion with CO_x as the major byprocucts.[20] The mechanism for vanadium catalyzed propane ODH is a surface mediated Mars-Van Krevelen

mechanism.[19,21] The first step of the reaction is a hydrogen abstraction, from a methyl hydrogen, which is enabled by the redox ability of the surface vanadium species. The vanadyl oxygen (V=O) is believed to perform this first hydrogen abstraction. After the first hydrogen abstraction, an alkyl radical and a reduced vanadium with a hydroxyl group form. The alkyl radical then either undergoes a second hydrogen abstraction over the same vanadium center or an adjacent vanadyl to form propylene, Scheme 1.1.[22] Next, the propylene will either desorb to the gas phase or undergo deep oxidation to form CO_x side products. There is debate whether the most selective pathway for propane formation happens over single or oligomeric vanadyl sites. Some authors claim that oligomeric sites lead to lower propylene selectivity by promoting oxidation to CO_x products.[23,24] Other authors state that isolated vanadyl structures show lower selectivity to propylene than oligomeric supported vanadium.[25] The disagreement in literature arises from both the difficulty in synthesizing truly isolated vanadyl sites and in the accurate characterization to differentia monomeric and oligomeric vanadium sites. Ultraviolet-visible spectroscopy (UV-vis) has been shown as a technique to distinguish these species.[26,27]

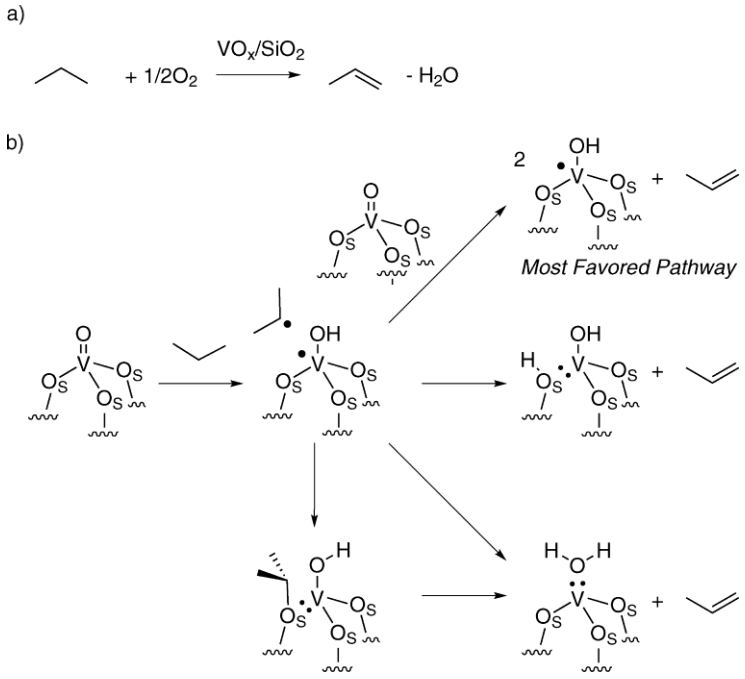

Scheme 1.1 (a) overall reaction for propane ODH over silica supported vanadium oxide, and (b) the proposed surface mechanism.[10,22]

Additionally, there is debate on which surface oxygen participates during the catalytic turnover. The different lattice oxygen species in Scheme 1.1 can be consumed during reaction and then replaced with the gas phase oxygen. The lattice oxygens and their configurations during the catalytic cycle are determined by their stability and activation barriers. The reoxidation of the catalytic surface is generally fast as the reaction order with respect to oxygen is zero. Some authors propose that a peroxo-vanadium species form during this reoxidation step while others debate the existence of this species.[28,29] This species is difficult to observe experimentally, but its role could be vital in explaining the reaction pathway of propane ODH over supported vanadium.[30]

Currently the propylene selectivity of silica supported vanadium catalysts is too low for industrial implementation. Overoxidation of the products at high conversion is responsible for the low selectivity. The addition of a second redox active metal to the supported vanadium catalyst can increase the activity and selectivity of the catalyst.[31] Addition of these metals, Ti and Ta, are

likely modifying the electronic properties of the active vanadium.[31–33] However, the promotional effect of these metal oxides is not well understood and complex due to the multiple factors impacting the system, i.e., acidity, oxidation state(s), and active site(s) accessibility. To better understand the mechanism of supported vanadium oxides a variety of synthetic, spectroscopic, kinetic, and computational techniques must be applied to the catalytic system.

1.4 Boron-containing catalysts propane ODH

In addition to vanadium oxide catalysts, boron-based materials are another more recent catalyst investigated for propane ODH.[6] Hexagonal boron nitride (h-BN) was recently shown as a highly selective and reactive catalysts for ODH (79% propane selectivity, 12% ethylene selectivity at 14% propane conversion) performing even better than vanadium supported on silica. [12,20,34–37] Instead of having CO_x as a major byproduct, another valuable olefin, ethylene, is the major byproduct. These boron-based catalysts are a promising material for development to the point of industrial implementation. Several studies have been done on boron materials to monitor how the boron surface changes during reaction.[12,38,39] After reaction the surface of these boron materials show the formation of a highly dynamic oxidized boron surface with various configurations of BO_3 units on both h-BN and silica supported boron (B/SiO_2). These experimental studies are also supported by computational studies showing varied compositions and the dynamic nature of the oxidized boron surface of the catalyst.[40,41] These studies have yielded valuable insights into the reaction mechanism and reactor design for optimizing propane ODH performance. [35,37] However, the exact nature of the boron active site is not explicitly known. There are theories on how the boron sites' characteristics are important to reactivity, but a defined active site(s) other than a general BO_x phase has not been identified .[38,39] To better understand and elucidate the mechanism of boron-based ODH catalysts a defined active site of BO_3 will be generated via controlled

synthesis to identify its contribution to catalytic system. As a result, structure-performance relationships can be generated to further characterize the catalytic system.

1.5 Thesis research goals

The goal of this work is to gain understanding of the vanadium and boron catalyzed systems for the oxidative dehydrogenation of propane. The focus of work will begin with directed synthesis to form defined active sites which must be accurately characterized by a variety of spectroscopic and analytical methods. To develop the corresponding structure-activity relationships kinetic and computational techniques will also be applied. The methods used and results obtained can then be applied to future development of these catalysts and propane ODH.

Chapter 2 shows the development of a boron containing zeolite synthesized as a way to create isolated and stable BO_3 units to be tested for propane ODH. This material was then extensively characterized by nuclear magnetic resonance spectroscopy (NMR) and catalytically tested. This study added valuable information to the mechanistic story of propane ODH in directing future studies on boron for ODH. Chapter 3 builds on the zeolite from the previous chapter and further tailors the material synthesis method to create isolated and oligomeric vanadium oxide species. The characterization and additional kinetic information gained through reactor and computational investigation adds to the mechanistic knowledge of vanadium oxide catalyzed ODH. Chapter 4 investigates complex ternary vanadium oxide materials to identify the source of the improved activity that these materials exhibit. Then mechanistic knowledge from the previous chapter will be applied to the more complex system to understand and further improve supported vanadium oxide catalysts. Finally, Chapter 5 will discuss the outlook for these areas of study in the ODH of propane.

References

1. CHEMICAL SECTOR PROFILE. https://www.cisa.gov/sites/default/files/publications/Chemical-Sector-Profile_Final%20508.pdf (Accessed August 9, 2023)
2. Amghizar, I., Vandewalle, L. A., Van Geem, K. M. & Marin, G. B. New Trends in Olefin Production. *Engineering* **3**, 171–178 (2017).
3. Monai, M., Gambino, M., Wannakao, S. & Weckhuysen, B. M. Propane to olefins tandem catalysis: A selective route towards light olefins production. *Chem Soc Rev* **50**, 11503–11529 (2021).
4. Liu, S., Zhang, B. & Liu, G. Metal-based catalysts for the non-oxidative dehydrogenation of light alkanes to light olefins. *React Chem Eng* (2021) doi:10.1039/d0re00381f.
5. Cavani, F. & Trifirò, F. *The oxidative dehydrogenation of ethane and propane as an alternative way for the production of light olefins*. *Catalysis Today* vol. 24 https://pdf.sciencedirectassets.com/271364/1-s2.0-S0920586100X00132/1-s2.0-092058619500051G/main.pdf?x-amz-security-token=AgoJb3JpZ2luX2VjEEYaCXVzLWVhc3QtMSJHMEUCIDw%2BwWDPTA4TIBx5tWdqYNmvgU6MTmcNgm7kQfQWrYNjAiEA1pWHG4n0mLSe5gNkhGes3jc6aT61%2BMdfvWpmeWw55 (1995).
6. Venegas, J. M., McDermott, W. P. & Hermans, I. Serendipity in Catalysis Research: Boron-Based Materials for Alkane Oxidative Dehydrogenation. *Acc Chem Res* **51**, 2556–2564 (2018).
7. Sundaram, K. M., Shreehan, M. M. & Olszewski, E. F. Ethylene. in *Kirk-Othmer Encyclopedia of Chemical Technology* 1–39 (John Wiley & Sons, Inc., 2010). doi:10.1002/0471238961.0520082519211404.a01.pub3.
8. Rightor, E. G. & Tway, C. L. Global energy & emissions reduction potential of chemical process improvements. *Catal Today* **258**, 226–229 (2015).
9. Propylene Market Size, Trends and Forecast to 2030. https://www.coherentmarketinsights.com/market-insight/propylene-market-1997.
10. Dong, S., Altvater, N. R., Mark, L. O. & Hermans, I. Assessment and comparison of ordered & non-ordered supported metal oxide catalysts for upgrading propane to propylene. *Appl Catal A Gen* **617**, 118121 (2021).
11. Amghizar, I., Vandewalle, L. A., Van Geem, K. M. & Marin, G. B. New Trends in Olefin Production. *Engineering* (2017) doi:10.1016/J.ENG.2017.02.006.
12. Grant, J. T. *et al.* Boron and Boron-Containing Catalysts for the Oxidative Dehydrogenation of Propane. *ChemCatChem* **9**, 3622 (2017).

13. Shell Chemicals. *Product Stewardship Summary Ethylene*. http://www.epa.gov/hpvis/index.html (2017).

14. FILLING THE PROPYLENE GAP-SHAPING THE FUTURE WITH ON-PURPOSE TECHNOLOGIES. https://pages2.honeywell.com/rs/828-DHL-685/images/Filling%20the%20Propylene%20Gap%20On%20purpose%20technologies.pdf (Accessed August 8, 2023)

15. Sattler, J. J. H. B., Ruiz-Martinez, J., Santillan-Jimenez, E. & Weckhuysen, B. M. Catalytic dehydrogenation of light alkanes on metals and metal oxides. *Chem Rev* **114**, 10613–10653 (2014).

16. The Changing Landscape of Hydrocarbon Feedstocks for Chemical Production. *The Changing Landscape of Hydrocarbon Feedstocks for Chemical Production* (2016) doi:10.17226/23555.

17. Tian, J. *et al.* Hexagonal boron nitride catalyst in a fixed-bed reactor for exothermic propane oxidation dehydrogenation. (2018) doi:10.1016/j.ces.2018.04.029.

18. Cavani, F., Ballarini, N. & Cericola, A. Oxidative dehydrogenation of ethane and propane: How far from commercial implementation? (2007) doi:10.1016/j.cattod.2007.05.009.

19. Grant, J. T., Venegas, J. M., McDermott, W. P. & Hermans, I. Aerobic Oxidations of Light Alkanes over Solid Metal Oxide Catalysts. *Chemical Reviews* vol. 118 2769–2815 Preprint at https://doi.org/10.1021/acs.chemrev.7b00236 (2018).

20. Grant, J. T. *et al.* Selective oxidative dehydrogenation of propane to propene using boron nitride catalysts. *Science (1979)* **354**, 1570–1573 (2016).

21. Carrero, C. A., Schloegl, R., Wachs, I. E. & Schomaecker, R. Critical literature review of the kinetics for the oxidative dehydrogenation of propane over well-defined supported vanadium oxide catalysts. *ACS Catal* **4**, 3357–3380 (2014).

22. Copéret, C. C-H bond activation and organometallic intermediates on isolated metal centers on oxide surfaces. *Chem Rev* **110**, 656–680 (2010).

23. Solsona, B. *et al.* Vanadium Oxide Supported on Mesoporous MCM-41 as Selective Catalysts in the Oxidative Dehydrogenation of Alkanes. *J Catal* **203**, 443–452 (2001).

24. Liu, Y.-M. *et al.* Vanadium oxide supported on mesoporous SBA-15 as highly selective catalysts in the oxidative dehydrogenation of propane. *J Catal* **224**, 417–428 (2004).

25. Barman, S. *et al.* Single-Site VOx Moieties Generated on Silica by Surface Organometallic Chemistry: A Way to Enhance the Catalytic Activity in the Oxidative Dehydrogenation of Propane. *ACS Catal* **6**, 5908–5921 (2016).

26. Gao, X. & Wachs, I. E. Investigation of Surface Structures of Supported Vanadium Oxide Catalysts by UV−vis−NIR Diffuse Reflectance Spectroscopy. *Journal of Physical Chemistry B* **104**, 1261–1268 (2000).

27. Bulánek, R., Čapek, L., Setnička, M. & Čičmanec, P. DR UV-vis study of the supported vanadium oxide catalysts. *Journal of Physical Chemistry C* **115**, 12430–12438 (2011).

28. Doornkamp, C. & Ponec, V. The universal character of the Mars and Van Krevelen mechanism. *J Mol Catal A Chem* **162**, 19–32 (2000).

29. Molinari, J. E. & Wachs, I. E. Presence of surface vanadium peroxo-oxo umbrella structures in supported vanadium oxide catalysts: Fact or fiction? *J Am Chem Soc* **132**, 12559–12561 (2010).

30. Haija, M. A. *et al.* Low temperature adsorption of oxygen on reduced V2O3(0001) surfaces. *Surf Sci* **600**, 1497–1503 (2006).

31. Carrero, C. *et al.* High performance (VOx)n–(TiOx)m/SBA-15 catalysts for the oxidative dehydrogenation of propane. *Catal Sci Technol* **4**, 786–794 (2014).

32. Grant, J. T. *et al.* Improved Supported Metal Oxides for the Oxidative Dehydrogenation of Propane. *Top Catal* **59**, 1545–1553 (2016).

33. Hamilton, N. *et al.* Topology of silica supported vanadium-titanium oxide catalysts for oxidative dehydrogenation of propane. *Catal Sci Technol* **2**, 1346–1359 (2012).

34. Venegas, J. M. *et al.* Selective Oxidation of n-Butane and Isobutane Catalyzed by Boron Nitride. *ChemCatChem* **9**, 2118–2127 (2017).

35. Venegas, J. M. & Hermans, I. The Influence of Reactor Parameters on the Boron Nitride-Catalyzed Oxidative Dehydrogenation of Propane. *Org Process Res Dev* **22**, 1644–1652 (2018).

36. McDermott, W., Venegas, J. & Hermans, I. Selective Oxidative Cracking of n-Butane to Light Olefins over Hexagonal Boron Nitride with Limited Formation of COx. *ChemSusChem* cssc.201901663 (2019) doi:10.1002/cssc.201901663.

37. Venegas, J. M. *et al.* Why Boron Nitride is such a Selective Catalyst for the Oxidative Dehydrogenation of Propane. *Angewandte Chemie - International Edition* **59**, 16527–16535 (2020).

38. Love, A. M. *et al.* Probing the Transformation of Boron Nitride Catalysts under Oxidative Dehydrogenation Conditions. *J Am Chem Soc* **141**, 182–190 (2019).

39. Love, A. M. *et al.* Synthesis and Characterization of Silica-Supported Boron Oxide Catalysts for the Oxidative Dehydrogenation of Propane. *Journal of Physical Chemistry C* **123**, 27000–27011 (2019).

40. Wheelock, P. B., Cook, B. C., Harringa, J. L. & Russell, A. M. Phase changes induced in hexagonal boron nitride by high energy mechanical milling. *J Mater Sci* **39**, 343–347 (2004).

41. Zhang, Z., Jimenez-Izal, E., Hermans, I. & Alexandrova, A. N. Dynamic Phase Diagram of Catalytic Surface of Hexagonal Boron Nitride under Conditions of Oxidative Dehydrogenation of Propane. *Journal of Physical Chemistry Letters* **10**, 20–25 (2019).

Chapter 2: Investigating single site boron catalysis for the oxidative dehydrogenation of propane.

This chapter is adapted from the publications listed below. I contributed to the material synthesis, materials characterization, experimental direction, and data interpretation.

Altvater, N. R. *et al.* B-MWW Zeolite: The Case Against Single-Site Catalysis. *Angewandte Chemie - International Edition* **59**, 6546–6550 (2020).

Dorn, R. W. *et al.* Structure Determination of Boron-Based Oxidative Dehydrogenation Heterogeneous Catalysts With Ultrahigh Field 35.2 T 11 B Solid-State NMR Spectroscopy. *ACS Catal* **10**, 13852–13866 (2020).

2.1 Background for boron containing catalysts for oxidative dehydrogenation of propane.

Boron containing materials have recently been identified as a highly selective catalyst for oxidative dehydrogenation (ODH) catalysts performing better than supported vanadium catalysts[1–7]. Hexagonal boron nitride was shown to not only have high selectivity (79%) to propylene at 14% conversion, but its major byproduct is ethylene, another high value chemical, instead of CO_x products.[2] While the activity and selectivity of these materials are higher than those of vanadium-based materials for propane ODH, they still suffer from overoxidation at high conversion. To better understand the source of this unprecedented high catalytic performance, the mechanism and active site(s) were investigated. A series of boron-based catalysts formed an oxidized/hydroxylated boron layer after being treated under propane ODH conditions. This oxidized phase forms at the surfaces of both bulk (i.e., h-BN, elemental B, and B_4C) and supported boron catalysts (i.e., B/SiO_2, and B/OAC) under catalytic conditions.[8–14] This BO_x surface contains a large distribution of boron sites which need to be better characterized spectroscopically and kinetically.

2.2 Identifying an active site for boron-based catalysts.

There have been attempts to control the addition of boron to a support, such as SiO_2, and create highly dispersed and uniform boron sites that can be better characterized and correlated with catalytic performance.[11,12,15] These studies have been done on amorphous supports and have primarily reinforced the dynamic and complex nature/behavior of the BO_x phase that forms under reaction conditions.

Both computational and experimental studies have shown that an amorphous oxyfunctionalized BO_x phase forms at the surface of these bulk and supported boron materials after an induction period.[14,16–18] This phase, generally described by $B_2(OH)_xO_{(3-x/2)}$ (x = 0–6) contains three-coordinate boron sites with varying numbers of hydroxyl and bridging-oxide groups.[12] Of the various boron site configurations in active materials, authors have suggested that the active site is a single tri-coordinate B-OH unit with connectivity to the bulk material or support.[19] Other authors have suggested that boron mobility and a degree of B-O-B connectivity is key to reactivity.[11] Therefore, there is disagreement about what the active site is and whether the catalytic can best be described or modeled over a single-site model or a multi-site model.

The dynamic nature of this active boron phase does not allow for accurate characterization of the sites during reaction when relying on spectroscopic methods on materials before and after reaction (referred to as fresh and spent). The phase composition changes under varying catalytic conditions and therefore also changes when at ambient conditions. Even the level of hydration in ambient conditions, where most spectroscopic techniques are done, can significantly change the boron surface characteristics.[20,21] Investigation using an in-situ approach which is complex and often limited in either scale or suffers from low resolution at reaction conditions that often involve high temperatures.[22,23] An alternate way to approach is to use a synthetic approach to selectively

synthesize the different boron structures and determine their kinetic contributions. [24] Previous studies have not been able to successfully isolate sites that are also stable under reaction conditions. This single site synthesis approach is not always straightforward and requires detailed synthesis.[25]

2.3 Housing stable, isolated boron sites in a zeolite framework

Here, a zeolite is used as a framework to house isolated boron sites. Zeolites are microporous crystalline materials comprised of SiO_4 tetrahedra called T-sites.[26] These T-sites can be replaced with various other atoms (Al, B, Ga, Pt, Cu, Sn, etc.) by isomorphic substitution to tune the material properties.[27] These substitutions can be achieved via direct hydrothermal synthesis or post-synthetic methods such as impregnation or ion-exchange.[28] Zeolites are widely used as catalysts in industry due to their robustness and tunability of their catalytic properties, including the Bronsted-Lewis acidity, surface area, pore size, and creating catalytic centers.[29] The uniform nature of the zeolite framework's crystal structure offers a well-defined support to allow for controlled addition of boron species on to the support. Here the zeolite Mobile Composition of Matter-twenty-two (MCM-22), also known as MWW, is used for the incorporation of boron atoms.

MWW is an industrially prepared and used zeolite as an additive to ZSM-5 applied for catalytic cracking in Mobile's Badger Cumene process for the alkylation of benzene, the alkylation of toluene, and the liquid phase epoxidation of propylene.[30–33] The borosilicate form of this zeolite (also called ERB-1 or B-MWW) is used as an intermediate for creating high Si/Al ratio frameworks and for the post-synthetic incorporation of metals into the structure. Because of the industrial applications of MWW, it can be safely concluded that this framework accommodates propylene molecules and is therefore suitable for use as a propane ODH catalyst. Additionally, B-MWW is a borosilicate zeolite. Therefore, B-MWW is compositionally analogous to B/SiO_2

materials in that there are only SiO_2 and BO_x components present. Therefore, any catalytic activity seen is the result of the boron species and not the ODH inert SiO_2 structures.

2.4 Material synthesis and catalytic testing

B-MWW was hydrothermally synthesized according to a literature procedure.[34] Boric acid was added to the synthesis gel as the boron source. To confirm the success synthesis of the zeolite powder X-ray diffraction (p-XRD) and N_2 physisorption ($S_{BET} = 498\ m^2g^{-1}$) was used. The p-XRD in Figure 2.1 showed no evidence of boron oxide formation so the presence of oxide crystals could be ruled out, and the framework matched the reference p-XRD pattern showing successful synthesis of B-MWW. The boron weight loading was measured via inductively coupled plasma mass spectrometry (ICP-MS) and found to be 1.1 ± 0.1 wt.%. Previous studies on boron supported on silica (B/SiO_2) made by incipient wetness impregnation (IWI) has a boron loading in a range of 0.23-2.20 wt.%.[11] This set of materials showed significant propane conversion to propylene under typical ODH conditions.[11] Since the boron loading of B-MWW falls within the same loading as the active B/SiO_2 materials, the zeolite is expected to be active for propane ODH.

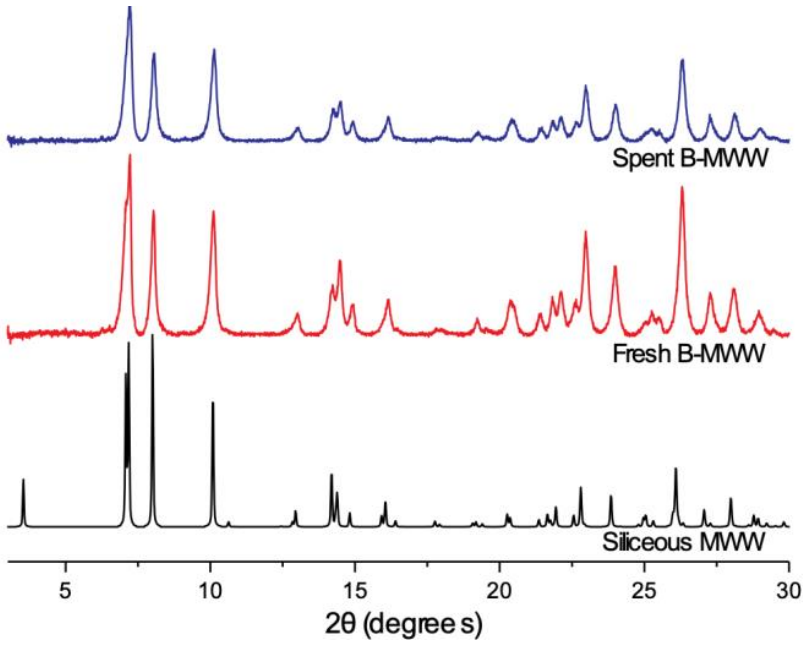

Figure 2.1 Powder X-ray diffraction (p-XRD) pattern of zeolite B-MWW before (fresh) and after (spent) treatment under propane oxidative dehydrogenation conditions.[35,36]

Catalytic testing was done at 500°C under flow of C_3H_8, O_2, and N_2 with a pretreatment at 525°C under the same gas composition. Surprisingly, B-MWW showed no propane conversion at reaction temperature above the background reactivity observed in a blank reactor at the same conditions, that is <0.5% propane conversion. This result was unexpected based on the loading since a B/SiO_2 catalyst with a boron loading of 0.23 wt.% had an olefin selectivity of 92% at 4% propane conversion under the same catalytic conditions.[11] Elemental analysis of the spent B-MWW showed that the boron content did not change within the error margin indicating that there was no significant leaching during reaction. The lack of catalytic activity over the zeolite indicated that the boron species in the framework are not active for propane ODH. Before proceeding with detailed characterization of the B-MWW an additional control material was synthesized. Boron was added via IWI to the B-MWW material using a similar procedure to B/SiO_2.[11] This material, denoted B/B-MWW had a boron loading of 1.3 ± 0.1 wt.% and showed similar catalytic activity

to B/SiO_2, with 90% olefin selectivity at 5% propane conversion. Previous studies have shown that B/SiO_2 materials have agglomerated boron species which was likely the case for B/B-MWW. B-MWW was likely inactive as an ODH catalyst because it contains stable and isolated boron species in the zeolite framework.

2.5 Detailed boron characterization via solid-state NMR

2.5.1 Characterization of as synthesized B-MWW

To determine the exact boron speciation in the above-described materials, a series of ^{1}H and ^{11}B magic angle spinning (MAS) solid-state NMR (SS-NMR) spectroscopy experiments were conducted to probe the structure and distribution of boron in the zeolite framework. As a note, ^{11}B NMR in zeolites will be impacted by the level of hydration.[20,21] Hydrated samples will have broader signals and the coordination of a fraction of the boron atoms will change from four- to three-coordinate. To avoid distortion of experiments, all samples were fully dehydrated and handled in an inert atmosphere prior to any SS-NMR measurements. ^{11}B spin echo MAS SS-NMR spectra was recorded, at 11.7 T, on a fresh and spent (after 12 h on stream) B-MWW sample. The spectra collected (Figure 2.2) were fitted to three distinct sites and when comparing each site between the fresh and spent, near identical quadrupolar fitting parameters (Table 2.1) were seen. This observation suggested that no boron restructuring occurred under reaction conditions and agrees with the elemental analysis that showed no leaching post reaction. The boron species were all trigonal-planar species as determined by their characteristic values for the ^{11}B isotropic chemical shift (δ_{iso}), electric field gradient asymmetry parameter (η), and quadrupolar coupling constant (C_Q).[12,37,38]

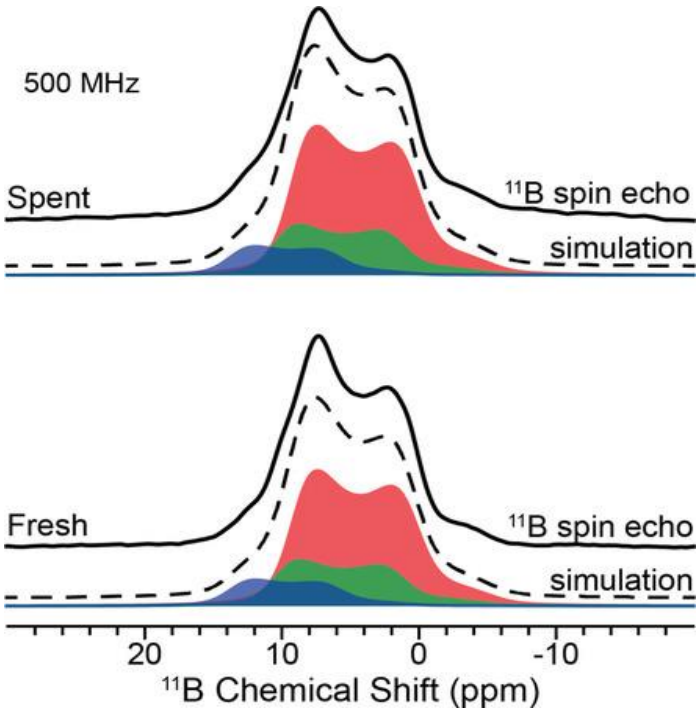

Figure 2.2 1D ^{11}B MAS SSNMR spectra of fresh and spent B-MWW. The solid lines represent the experimental spectra, and dashed lines are the analytical simulations. The analytical simulation is made of up the individually shaded sites whose parameters are reported in Table 2.1.[35]

Table 2.1 Analytical simulations parameters for Figure 2.2. Both Fresh and Spent B-MWW spectra were fitted with the same parameters.[35]

Site	**δ_{iso} (ppm)**	**C_Q (MHz)**	**η**	**Integration (%)**
red	11	2.6	0.0	66
green	12	2.4	0.0	23
blue	15	2.7	0.0	11

To further validate the three-site fit of these spectra, a series of 2-dimensional SS-NMR correlation experiments were conducted. To confirm the validity of the sties analytically fit in Figure 2.2, a 2-dimensional ^{11}B triple-quantum multiple quantum MAS (MQMAS) of fresh B-MWW was run, a 9.4 T spin echo of ^{11}B SSNMR spectrum was fitted with the same site parameters, and a 2-dimensional ^{1}H – ^{11}B heteronuclear correlation (HETCOR) experiment was performed. Since the spectrum at the lower 9.4 T magnetic field could be fit to the same parameters, the fit is validated, see Figure A.1. The two most downfield simulated sites fitted to the experimental peak were assigned to framework $B(OSi)_3$ species substituted into the zeolite based on their isotropic chemical shifts, $\delta_{iso}(^{11}B) = 11$ ppm (red peak) and $\delta_{iso}(^{11}B) = 12$ ppm (green peak). [12,20,37,38] The simulated peak fits in Figure 2.2 have a broad peak shape that indicated a distribution in the boron sites from the minor differences in the chemical environment that likely result from the eight distinct T-sites that zeolites MWW has which boron could occupy.[20,39] The fitted peak at $\delta_{iso}(^{11}B) = 15$ ppm (blue site) is assigned to a $B(OSi)_2(OH)$ species which has two bonds to the silicate framework and one bond to a terminal hydroxyl group. The blue peak is integrated to approximately 10% of the total analytical simulation. Accordingly, the integration of the simulated peaks assigned to $B(OSi)_3$ units is approximately 90% of the detected species meaning that the large majority of boron in the zeolite is fully incorporated into the zeolite framework. The previously published findings of Zones and co-workers where various boron doped zeolites, BETA, SSZ-33, and SSZ-42 were studied with ^{1}H and ^{11}B SSNMR spectroscopy reported site assignments consistent with those described above.[20] Their SSNMR experiments were done with the high field of 19.6 T for ^{11}B spin echo, 2D ^{1}H -> ^{11}B CP-HETCOR and ^{11}B MQMAS. These spectra clearly indicated that a higher fields of $\delta_{iso}(^{11}B)$ = 10.0-14.8 ppm correspond to $B(OSi)_3$ and $B(OSi)_2(OH)$ species compared to the lower field $\delta_{iso}(^{11}B) = 18.0$ ppm

of non-framework boron species.[20] The range of isotropic shifts accounts for the distribution in the different types of zeolite frameworks. The ^{11}B isotropic shifts for to $B(OSi)_3$ and $B(OSi)_2(OH)$ species reported by Zones et al. match very well our results described above. This reference study verifies that the B-MWW synthesis here contains primarily framework species.[20]

2.5.2 Characterization of boron doped B/B-MWW

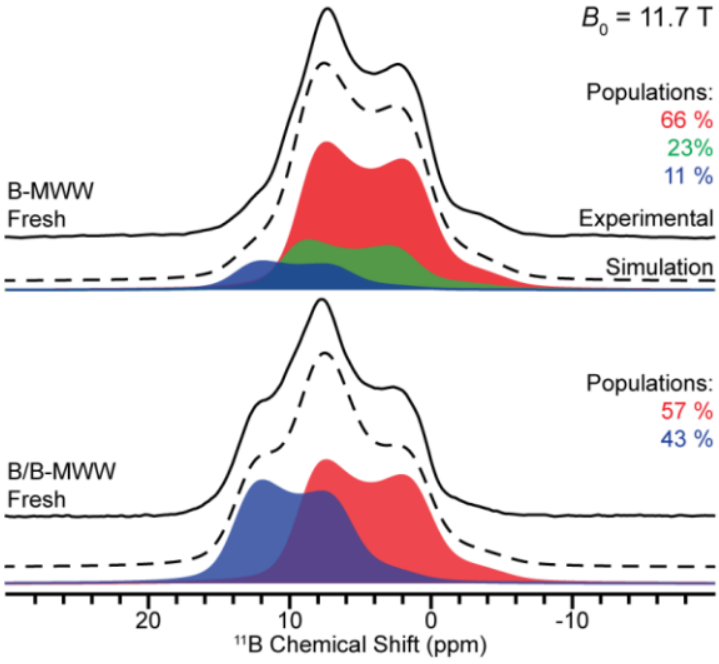

Figure 2.3 1D ^{11}B spin echo of B/B-MWW and B-MWW fresh as labeled. Spectra were recorded with 10 kHz (B-MWW) and 14 kHz (B/B-MWW) and both at 11.7 T.[35]

In Figure 2.3 and Figure A.2 the ^{11}B spin echo spectrum of the ODH active B/B-MWW catalyst shows that 57% of the boron species are framework $B(OSi)_3$ type groups at $\delta_{iso}(^{11}B)$ = 11 ppm, and 43% are B(OSi)(OH) species at $\delta_{iso}(^{11}B)$ =15 ppm. In comparison to the above discussed spin echo spectrum of B-MWW, the $B(OSi)_2(OH)$ species make up a considerably larger fraction of the boron sites in B/B-MWW. The ^{11}B spin echo of the B/B-MWW and the corresponding peak fitting parameters for their simulated sites are similar to those of the B/SiO_2 materials that are catalytically active for propane ODH.[11] The sites in B/B-MWW are assigned to framework species, $B(OSi)_3$ and $B(OSi)_2(OH)$, which correspond to the same assignment groups made for B-MWW. However, a fraction of the ^{11}B NMR signal likely arises from clustered boron sites. This possible structure will be discussed in more detail below.

2.5.3 Heteronuclear correlations of ^{11}B and ^{1}H

To better elucidate the boron speciation and bolster the site assignments given for the distinct ^{11}B NMR signals for B-MWW, ^{1}H-^{11}B correlation NMR experiments were performed. Due to the similarity of the fresh and spent spin echo spectra, the fresh B-MWW material will be the subject of these following experiments. The two-dimensional $^{11}B \rightarrow {}^{1}H$ dipolar-refocused INEPT (D-RINEPT) were recorded at a frequency of 25 kHz MAS with different total recoupling times (total $SR4^2_1$ ^{1}H heteronuclear dipolar recoupling time) of t = 0.64 ms or t = 2.56 ms represented in Figure 2.4 a in blue and red traces respectively.[40,41]

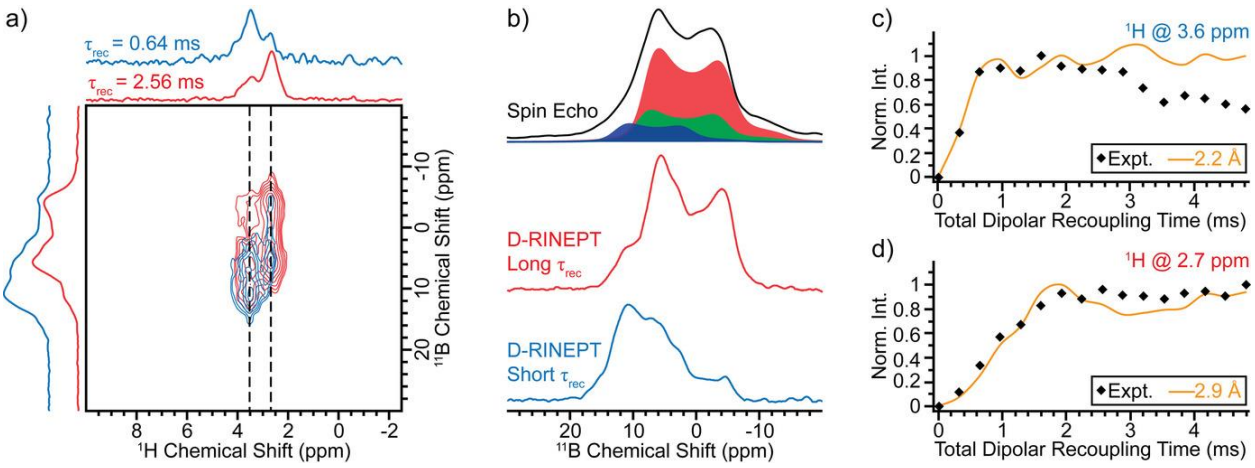

Figure 2.4 (a) 2D $^{11}B \rightarrow {}^{1}H$ D-RINEPT spectra of B-MWW acquired with 0.64 ms and 2.56 ms (blue and red respectively) of total heteronuclear dipolar recoupling time. (b) Comparison of the 1D ^{11}B spin echo spectrum and projections for the D-RINEPT spectra taken with 0.64 ms and 2.56 ms (blue and red respectively) of total heteronuclear dipolar recoupling time. The dashed lines in (a) correspond to the dipolar recoupling buildup curves for the ^{1}H slices at (c) 3.6 ppm and (d) 2.7 ppm. The solid lines are the numerical SIMPSON simulations for the experimental points (black diamonds). The simulations for heteronuclear dipolar couplings correspond to the $^{1}H - {}^{1}B$ inter-nuclear distances. Spectra were recorded at 9.4 T with 25 kHz MAS.[35]

The discreet ^{1}H and ^{11}B resonances can be seen in the 1D and 2D $^{11}B \rightarrow {}^{1}H$ D-RINEPT depending on the duration of the heteronuclear dipolar recoupling time. At a recoupling time of 0.64 ms, blue trace, the higher frequency ^{1}H NMR signal are observed at approximately 3.6 ppm. These spectra show strong correlations to the higher frequency ^{11}B NMR signal at approximately 15 ppm as seen in Figure 2.4 (b) and Figure A.3. This shorter recoupling time that corresponds with the ^{1}H NMR signal at 3.6 ppm and the ^{11}B NMR signal at 15 ppm is attributed to the $B(OSi)_2(OH)$ framework sites as depicted in Figure 2.5. The D-RINEPT recorded with the longer dipolar recoupling time of 2.56 ms has a strong correlation between the ^{11}B NMR signal at 11-12 ppm and the ^{1}H NMR signal at 2.7 ppm. Based on the strong $^{11}B \rightarrow {}^{1}H$ NMR correlation the nuclei must be in spatial proximity, but the ^{11}B NMR shift indicates that the proton likely not bonded to the boron nucleus. A more detailed structure of this isotropic shift range of ^{11}B sites will be discussed in the following sections. If the ^{11}B spin echo from Figure 2.2 is compared to the ^{11}B

NMR extracted from the 2D $^{11}B \rightarrow {}^{1}H$ NMR D-RINEPT spectrum in Figure 2.4 (b) and A.3, the two spectra are nearly identical in appearance. This similarity between spectra indicates that all boron atoms in the B-MWW material are proximate to ^{1}H spins. When the same comparison between the ^{11}B NMR spectrum from the 2D D-RINEPT and ^{11}B spin echo for the B/B-MWW material, the spectra do not show the same overlap and similarity. These observations suggest that a portion of the ^{11}B spins detected in the B/B-MWW material are not correlated to and therefore distant from proton spins. This structure is likely due to the existence of boron oxide type clusters, which are known to be present in ODH active B/SiO_2 materials that share the same activity as the B/B-MWW.[42]

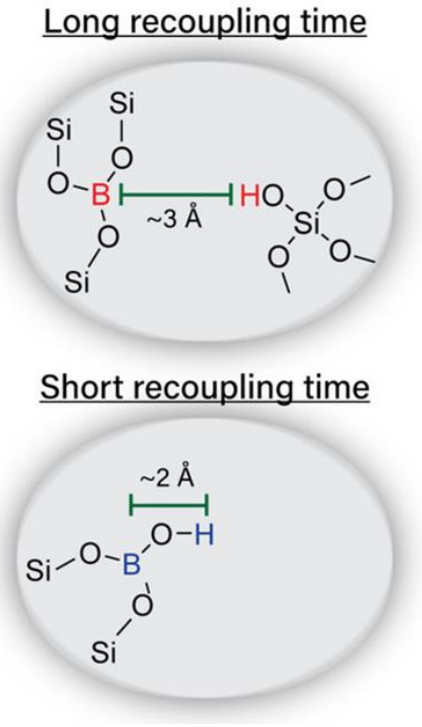

Figure 2.5 Illustration of the two types of boron structures in the zeolite framework and types of ^{11}B – ^{1}H interactions seen in the and 2D ^{11}B → ^{1}H D-RINEPT spectra.[35]

2.5.4 Dipolar recoupling buildup experiments on ^{11}B and ^{1}H

To further investigate the structure of the zeolite framework incorporated boron species, the ^{1}H - ^{11}B inter-nuclear distance for the pairs of correlated ^{1}H - ^{11}B NMR signals was estimated using ^{1}H - ^{11}B dipolar build-up curves from the 2D ^{11}B → ^{1}H D-RINEPT sequence. Figure 2.4 (c) and (d) illustrate the ^{1}H NMR signal intensity from the ^{11}B → ^{1}H D-RINEPT is recorded as a function of the heteronuclear dipolar recoupling time. The dipolar recoupling constant (D_{ij}) between spins is proportional to the inverse of the distance between spins cubed. The inter-nuclear distances between ^{1}H and ^{11}B can then be estimated by comparing the experimental build-up curves to the numerical SIMPSON simulations for different ^{1}H – ^{11}B dipolar coupling constants.[43,44] The ^{1}H NMR signal at an isotropic shift of 3.6 ppm has a D-RINEPT signal build-up that best fits to a simulated curve with a dipolar coupling constant of approximately 3.6 kHz.

This dipolar coupling constant corresponds to an inter-nuclear $^{1}H - {}^{11}B$ distance of approximately 2.2 Å, Figure 2.4 (c) and Figure A.4 (a). The proton on the isolated B-OH groups, as depicted in Figure 2.5, is not fixed and can experience a degree of rotation impacting the distance measurement. This rotation will average the $^{1}H - {}^{11}B$ dipolar coupling constant and result in a lower dipolar coupling constant measurement which will in turn mean a longer inter-nuclear distance than expected. The build-up for the 2.7 ppm ^{1}H NMR signal from the D-RINEPT best fits to a simulated curve with a $^{1}H - {}^{11}B$ dipolar coupling constant of approximately 1.6 kHz. This measurement corresponds to an inter-nuclear $^{1}H - {}^{11}B$ distance of approximately 2.9 Å, Figure 2.4 (d) and Figure A.4 (b). This relatively large inter-nuclear distance corresponds with the ^{11}B isotropic chemical shift of 11 ppm which was previously assigned to isolated $B(OSi)_3$ framework units. These observations together assign the ^{1}H NMR signal to an adjacent framework silanol group that is not directly bonded to the ^{11}B nuclei in question as shown in Figure 2.5. Previous studies on boron containing zeolites report a similar model.[20]

A proton detected $^{1}H\{^{29}Si\}$ cross polarization MAS (CPMAS) spectrum of the pristine B-MWW further shows that the 2.7 ppm signal from ^{1}H NMR arises from a silanol adjacent to a boron species, Figure A.4.[20,21,45,46] These silanol groups near a substituted, 3-coordinate boron site are expected defect sites since the boron atom is occupying a 4-coordinate T-site in place of a Si atom. The $^{1}H\{^{29}Si\}$ CPMAS spectrum was acquired by averaging the signal over the course of 10 hours. The majority of the $^{1}H\{^{29}Si\}$ CP signal seen in Figure A.4 corresponds to the same proton signal, 2.7 ppm in the longer dipolar recoupling time $^{11}B \rightarrow {}^{1}H$ D-RINEPT signal with a smaller peak shoulder at the ^{1}H NMR signal of 3.6 ppm from the shorter dipolar recoupling time $^{11}B \rightarrow {}^{1}H$ D-RINEPT. This observation indicated that the majority of the zeolite framework is pristine without major defect sites aside from the 1.1 wt.% of boron in the framework. Additionally,

infrared spectroscopy (IR) of the dehydrated B-MWW material confirms that B-OH groups (3700 cm^{-1}) and both external and defect site silanol groups (3745 cm^{-1} and 3720 cm^{-1} respectively) are present in the fresh and spent zeolite as shown in Figure 2.6.[47] The IR results confirm what the ^{11}B NMR spin echo spectra show that the fresh and spent materials are similar and do not significantly restructure under reaction conditions, so the boron sites are in a stable and isolated environment.

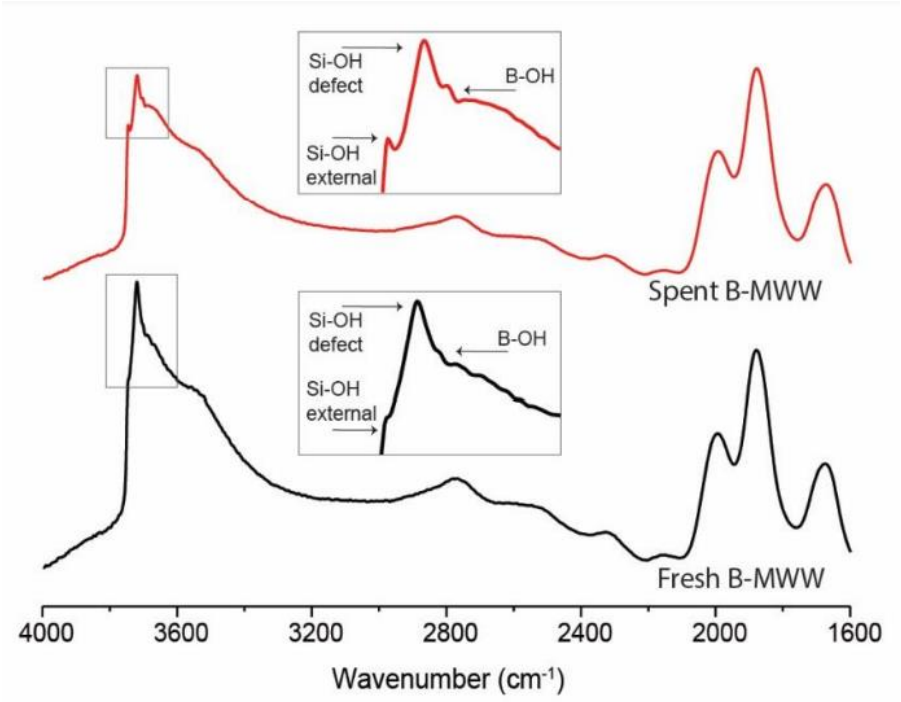

Figure 2.6 Transmission IR spectra of B-MWW fresh and spent. Arrows indicate lattice termination Si-OH (3745 cm^{-1}), defect Si-OH sites (3720 cm^{-1}), and B-OH (3700 cm^{-1}) features.[34] Materials were dehydrated at 500 °C prior to analysis, and spectra were normalized to SiO_2 overtones.[35]

2.5.5 Homonuclear NMR correlation experiments

As stated above, the isotropic chemical shifts for ^{11}B indicate that the boron atoms in the B-MWW are primarily incorporated into the zeolite framework. Another characteristic observed in the B/SiO_2 materials, is the proximity of boron sites to one another. Propane ODH active B/SiO_2 has both boroxyl rings and B-O-B moieties bonded to the silica support.[11,12] This characteristic boron aggregation is another possible factor that influences the activity or inactivity of boron containing materials. To determine whether the boron species in the B-MWW and B/B-MWW materials contain aggregated boron sites, either in the form of oxygen bonded nuclei or indirectly bonded but spatially proximate nuclei, the following SSNMR experiments were performed.

Based on the solid-state NMR data, the boron sites are at least 3-4 Å apart from each other. From the 2D $^{11}B \rightarrow {}^{1}H$ D-RINEPT experiment of B-MWW recorded at 2.56 ms recoupling time, there was a weak correlation between the ^{1}H NMR signal of $B(OSi)_2(OH)$ at 3.6 ppm and the ^{11}B NMR signal of $B(OSi)_3$. This weak correlation suggests that the incorporated boron atoms are well separated in the zeolite structure. The analysis is further supported by a 2D ^{11}H - ^{1}H double-quantum-single-quantum (DQ-SQ) homonuclear correlation experiment of B-MWW. Figure A.6 (a) shows that the proton signal assigned to silanol adjacent $B(OSi)_3$ groups at 2.7 ppm does not have any substantial signal intensity from the DQ. The lack of signal at the auto correlation of the $B(OSi)_3$ adjacent silanol indicates that these types of silanol sites are not in proximity to other protons, which indicates that the zeolite is not only mostly pristine with few defect sites, but also the $B(OSi)_3$ sites are not near one another. When the same $^{1}H - {}^{1}H$ DQ-SQ experiment is performed on B/B-MWW, these silanol adjacent $B(OSi)_3$ groups do show an observable DQ signal in ^{1}H NMR, Figure A.6 (b). This observation shows that the B/B-MWW has more aggregated boron species than the B-MWW.

Next, a 1D ^{11}B – ^{11}B DQ-SQ experiment was performed on both boron zeolite materials to determine the extent and nature of boron aggregation. The DQ-filtered ^{11}B NMR spectrum for the B/B-MWW has a signal intensity or about three times that of the B-MWW as seen in Figure A.7.[48–50] When compared with the single-quantum ^{11}B spin echo spectra, the double-quantum-filtered ^{11}B spectra both have a bias to positive isotropic chemical shifts which are associated with oxide and hydroxylated boron structures. The oxide-like boron sites are more abundant in the B/B-MWW zeolite as shown previously in the quantitative ^{11}B NMR experiments. The combination of these SSNMR experiments support the hypothesis that catalytically inactive B-MWW zeolite contains primarily isolated and stable boron sites fully incorporated into the zeolite framework. In contrast the ODH active B/B-MWW catalyst contains additional aggregated boron species. To further investigate the B-MWW discussed here and the ODH active B/SiO_2 catalyst, further SSNMR studies will be discussed below.

2.6 Ultra-high field SSNMR

The above studies were done with 11.7 T and 9.4 T and NMR spectrometers. While these instruments are sufficient and efficient at obtaining accurate characterization data, the spectral resolution is limited by the strength of the magnetic field and the characteristics of the nucleus measured. In the case of ^{11}B SSNMR spectroscopy, the resolution is limited since the ^{11}B nucleus is a half-integer quadrupolar nucleus, I = 3/2. The ^{11}B NMR signals are broadened second order quadrupolar interactions.[51–53] This broadening is related to the symmetry around the nucleus, with trigonal planar boron sites having larger broadening and tetrahedral sites having less broadening.[37,38] Signal broadening for central transition NMR spectroscopy is inversely proportional to the magnetic field strength. Increasing the magnetic field results in narrower and better resolved ^{11}B NMR signals. The following section will utilize an ultra-high magnetic field of 35.2 T to

significantly enhance the resolution of ^{11}B SSNMR spectra. This enhancement in resolution will further inform the local structure and connectivity of boron sites in B-MWW as well as other boron containing active ODH materials. For more details on the use and application of solid-state NMR of ^{11}B nuclei please refer to the associated publication.

Prior studies on boron-based ODH catalyst agree that an oxyfunctionalized surface of oxidized and hydroxylated boron sites make up the active phase. This active phase has been generally defined but there are structural details about it that remain unknown and can be further elucidated by high-resolution NMR. The ^{11}B NMR reposted here and in other works (Figure 2.2 and Figure 2.3) show ^{11}B NMR sites overlapping which can limit the resolution of 2D homonuclear and heteronuclear correlation experiments in NMR.[54] The high-resolution spectrometer will better resolve the multidimensional NMR studies reported in previous sections. The Series-Connected Hybrid magnet is operated where it was built at the National High Magnetic Field Laboratory in Tallahassee, Florida.[54]

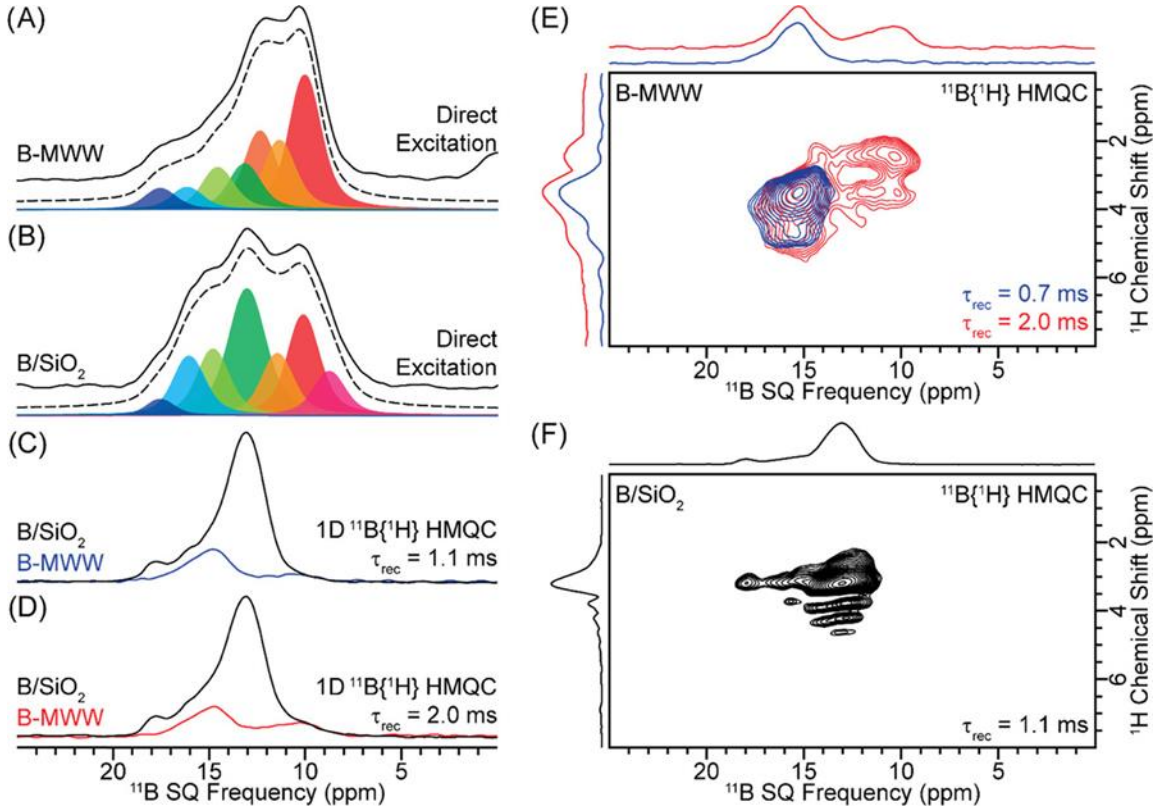

Figure 2.7 1D ^{11}B spectra of (a) B-MWW and (b) fresh B/SiO_2. 1D $^{11}B\{^1H\}$ D-HMQC spectra of B-MWW and B/SiO_2 recorded with (c) 1.1 ms or (d) 2.0 ms of total heteronuclear dipolar recoupling applied. The ^{11}B NMR spectra of B-MWW are (c) blue and (d) red, while the ^{11}B spectra of B/SiO_2 are black. (e) 2D $^{11}B\{^1H\}$ D-HMQC spectra of B-MWW acquired with either (blue) 0.7 ms or (red) 2.0 ms of total heteronuclear dipolar recoupling time. (f) 2D $^{11}B\{^1H\}$ D-HMQC spectrum of B/SiO_2 acquired with 1.1 ms total heteronuclear dipolar recoupling time. All spectra were recorded at 35.2 T with 18 kHz MAS.[55]

Here B-MWW and B/SiO_2 will be compared to determine the difference between two compositionally analogous boron containing silicate materials that have opposite catalytic performance. Figure 2.7 (a) and (b) show the ultra-high field spectra of B-MWW and B/SiO_2 respectively. The spectra were fitted to analytical simulations with their parameters shown in Table A.2. In contrast to Figure 2.3, Figure 2.7 (a) is fitted to seven different sites that have a much smaller broadening. This broader distribution of peaks is not inconsistent with the structural disorder seen in the 2D ^{11}B triple-quantum MQMAS spectrum recorded on the 9.4 T spectrometer, Figure A.8. For the B/SiO_2 material, the lower frequency signal around 12 ppm were assigned to

isolated BO_3 units and the higher-frequency signal around 16 ppm are attributed to isolated boroxly rings, linear chain metaborates, and isolated $BO_2(OH)$ units.[11] A 2D $^{11}B\{^1H\}$ D-HMQC experiment was used to determine the proximity of boron and hydrogen atoms using heteronuclear dipolar recoupling times of 0.7 and 2.0 ms applied to the proton spins, Figure 2.7 (e). At the short dipolar recoupling time of 0.7 ms (blue trace), only the higher-frequency ^{11}B NMR signals around 15 – 18 ppm are seen correlating to the ^1H NMR signals at 3.5 – 4.7 ppm. This range and correlation of signals is consistent with B-OH groups. At a higher heteronuclear dipolar recouping time of 2.0 ms, the lower-frequency ^{11}B NMR signals around 11 – 12 ppm appear and correlate with the proton signals from 2.4 – 3.5 ppm. The ^1H NMR signal at 2.4 ppm is the same previously attributed to a silanol site proximate to an isolated $B(OSi)_3$ unit. These findings are consistent with the conclusions reached using the lower magnetic field spectrometers confirming the expected boron structure. To better understand boron-boron interactions in B-MWW, a 2D ^{11}B dipolar DQ-SQ homonuclear correlation experiment was done. This experiment was recorded with 2.7 ms of total homonuclear dipolar recoupling time, and Figure A.9 (c) shows autocorrelations for ^{11}B NMR signal at 13 – 14 ppm (strong) and at 12 – 14 ppm and 15 – 17 ppm (weaker correlation). No correlation was seen at the lowest-frequency signal around 11 ppm confirming that these boron sites are isolated $B(OSi)_3$ units without boron agglomeration. The boron sites with the ^{11}B DQ-SQ NMR at 13-14 ppm did not show substantial signal in the proton - ^{11}B correlation indicating B–O–B connectivity without any proximate protons as shown in Figure 2.8. When the B^{11} homonuclear correlation signal intensity is compared to that of B/SiO_2, Figure A.9 (d) it is approximately 70-80% less which indicates that the B-MWW material has significantly less boron agglomeration than the amorphous silica supported material even though both have the same boron loading. In contrast the B/SiO_2 material is primarily oxidized boron clusters. These large boron

oxide clusters contain a variety of boron configurations that are shown in Figure 2.8 and their assignment is discussed in further detail in the associated publication.[55]

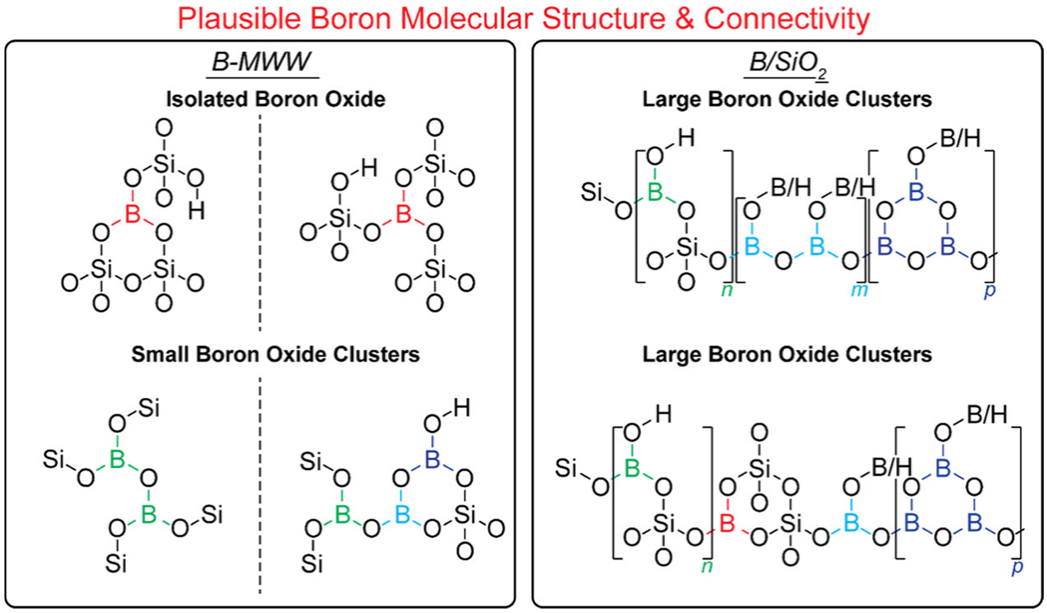

Figure 2.8 Possible boron site structures present in B-MWW and B/SiO_2. The boron atom colors correspond to the colors of the shaded site fits in the 1D ^{11}B NMR spectrum in Figure 2.7.[55]

For B-MWW the types of boron sites can be placed in three different categories shown in Figure 2.8 as boron atoms highlighted in red, green, and blue. A ^{11}B NMR shift of about 10.5 – 12 ppm (red boron atom), which makes up the majority of the boron species, is assigned to isolated $B(OSi)_3$ units in the zeolite framework with a silanol approximately 3.5 angstroms away. Next, the ^{11}B NMR signal at about 13 – 14 ppm (green boron atom), is attributed to $B(OSi)_2(OB)$. Since this region exhibited boron – boron interaction but no proton – boron interaction the structure is assigned to one B–O–B interaction and two B–O–Si bonds. Thirdly, the formation of small boron oxide clusters with multiple B–O–B and/or B–OH bonds cannot be completely ruled out. The ^{11}B NMR signal at about 15 – 18 ppm (blue boron atoms) is attributed to small, oxidized boron clusters. Boron species with more than one hydroxyl group can form but are near negligible based on the NMR data shown here.[56,57]

2.7 Conclusions

In summary, stable, isolated framework $B(OSi)_3$ and $B(OSi)_2(OH)$ species were incorporated into the zeolite MWW framework via hydrothermal synthesis. Multi-dimensional solid-state ^1H and ^{11}B NMR spectroscopy was used to characterize the zeolite structure. The majority of boron sites, approximately 90%, were non-hydroxylated $B(OSi)_3$ types that exist adjacent to a silanol group. Catalytic testing for the ODH of propane showed that the material is catalytically inactive, not exhibiting propane conversion over background levels, despite having sufficient boron loading for activity. Previous works, as well as this study have shown that catalytically active boron containing ODH catalyst including boron nitride, B/SiO_2, B/C, and B/B-MWW all have aggregated boron sites that will restructure under reaction conditions.[11–13] In contrast B-MWW does not have significant boron aggregation, does not show any boron restructuring under reaction conditions. The difference in the isolated, stable B-MWW boron sites and those in the other boron materials leads to the important conclusion that propane ODH over boron-catalyzed materials does not occur over a single BO_3 site. Instead, ODH active boron-based catalysts require boron structures with some degree of aggregation or B-O-B connectivity and/or mobility. The results of this study advance the mechanistic understanding of boron species in the propane ODH mechanism and serve to direct future work in elucidating the structural origins of activity in ODH catalyst. The exact types of boron-boron interactions still need to be investigated to better understand the source of high selectivity in boron-containing ODH catalysts.

The use of ultra-high field multidimensional ^{11}B NMR on B-MWW and B/SiO_2 enabled the more detailed identification of the molecular boron structures in these supports. It was confirmed that B-MWW contains primarily framework isolated $B(OSi)_3$ sites with nearby hydroxyl groups. Some small boron clusters are present in the zeolite. In contrast the B/SiO_2

material has large clusters of boron oxide on its surface that are dynamic under reaction conditions. Both supported boron materials have approximately 1 wt.% boron yet exhibit vastly different propane ODH performance. The stark difference in catalytic behavior, or the lack thereof, is attributed to the difference in boron agglomeration in the materials. The absence of any linear chain-type metaborates and any boroxol ring structures in the zeolite lead to the inactivity of the boron sites.

The application of detailed spectroscopy and controlled synthesis through the use of ordered supports has resulted in the formation of a controlled and highly uniform active site. The mechanistic insight gained from demonstrating that these sites are inactive will aid the design of future catalysts and direct the development of this area of study. The importance of effectively combining spectroscopic characterization and material synthesis was demonstrated in the above studies as each area of expertise independently provides little novelty to the literature. When combined, however, they can be applied to gain mechanistic understanding of an actively studies area.

2.8 Outlook

Avenues of future work include studies on the mobility of boron sites to determine how the stability of these sites influence the reactivity. In-situ and operando studies that combine spectroscopic and kinetic capabilities to see the evolution and structures of the active phase during catalysis. Here catalytic materials were spectroscopically studies pre and post kinetic treatment which are limited in what mechanistic information can be gathered. On the other hand, operando studies offer a wealth of information during the progression of the reaction that would break the next barrier for studying heterogeneous catalysis. In-situ and operando studies offer many challenges but have already been shown to be successful in several cases.

Additionally, synthesis-based studies focused on support studies to improve the performance of boron-containing materials can improve the current standard of this catalyst to bring it closer to industrial application. Amorphous supports such as activated carbon or have been shown as an active and inexpensive supports.[13] A zeolite encapsulation study could combine the high performance of h-BN with the structural control of a zeolite to improve catalytic performance. Finally, mechanistic studies are still underway to better understand the kinetic pathways so as to inform catalyst design.

References

1. Grant, J. T. *et al.* Boron and Boron-Containing Catalysts for the Oxidative Dehydrogenation of Propane. *ChemCatChem* **9**, 3622 (2017).

2. Grant, J. T. *et al.* Selective oxidative dehydrogenation of propane to propene using boron nitride catalysts. *Science (1979)* **354**, 1570–1573 (2016).

3. McDermott, W., Venegas, J. & Hermans, I. Selective Oxidative Cracking of n-Butane to Light Olefins over Hexagonal Boron Nitride with Limited Formation of COx. *ChemSusChem* cssc.201901663 (2019) doi:10.1002/cssc.201901663.

4. Huang, R. *et al.* Direct Insight into Ethane Oxidative Dehydrogenation over Boron Nitrides. *ChemCatChem* **9**, 3293–3297 (2017).

5. Shi, L. *et al.* Edge-hydroxylated Boron Nitride for Oxidative Dehydrogenation of Propane to Propylene. *ChemCatChem* **9**, 1788–1793 (2017).

6. Shi, L. *et al.* Selective oxidative dehydrogenation of ethane to ethylene over a hydroxylated boron nitride catalyst. *Cuihua Xuebao/Chinese Journal of Catalysis* **38**, 389–395 (2017).

7. Chaturbedy, P., Ahamed, M. & Eswaramoorthy, M. Oxidative Dehydrogenation of Propane over a High Surface Area Boron Nitride Catalyst: Exceptional Selectivity for Olefins at High Conversion. *ACS Omega* **3**, 369–374 (2017).

8. Venegas, J. M., McDermott, W. P. & Hermans, I. Serendipity in Catalysis Research: Boron-Based Materials for Alkane Oxidative Dehydrogenation. *Acc Chem Res* **51**, 2556–2564 (2018).

9. Grant, J. T. *et al.* Improved Supported Metal Oxides for the Oxidative Dehydrogenation of Propane. *Top Catal* **59**, 1545–1553 (2016).

10. Love, A. M. *et al.* Understanding the Synthesis of Supported Vanadium Oxide Catalysts Using Chemical Grafting. *Chemistry - A European Journal* **26**, 1052–1063 (2019).

11. Love, A. M. *et al.* Synthesis and Characterization of Silica-Supported Boron Oxide Catalysts for the Oxidative Dehydrogenation of Propane. *Journal of Physical Chemistry C* **123**, 27000–27011 (2019).

12. Love, A. M. *et al.* Probing the Transformation of Boron Nitride Catalysts under Oxidative Dehydrogenation Conditions. *J Am Chem Soc* **141**, 182–190 (2019).

13. Mark, L. O. *et al.* Highly Selective Carbon-Supported Boron for Oxidative Dehydrogenation of Propane. *ChemCatChem* **13**, 3611–3618 (2021).

14. Zhang, Z., Jimenez-Izal, E., Hermans, I. & Alexandrova, A. N. Dynamic Phase Diagram of Catalytic Surface of Hexagonal Boron Nitride under Conditions of Oxidative Dehydrogenation of Propane. *Journal of Physical Chemistry Letters* **10**, 20–25 (2019).

15. Lu, W. D. *et al.* Supported Boron Oxide Catalysts for Selective and Lowerature Oxidative Dehydrogenation of Propane. *ACS Catal* **9**, 8263–8270 (2019).

16. Zhang, X. *et al.* Radical Chemistry and Reaction Mechanisms of Propane Oxidative Dehydrogenation over Hexagonal Boron Nitride Catalysts. *Angewandte Chemie - International Edition* **59**, 8042–8046 (2020).

17. Tian, J. *et al.* Hexagonal boron nitride catalyst in a fixed-bed reactor for exothermic propane oxidation dehydrogenation. (2018) doi:10.1016/j.ces.2018.04.029.

18. Venegas, J. M. *et al.* Why Boron Nitride is such a Selective Catalyst for the Oxidative Dehydrogenation of Propane. *Angewandte Chemie - International Edition* **59**, 16527–16535 (2020).

19. Qiu, B. *et al.* Oxidative dehydrogenation of propane using layered borosilicate zeolite as the active and selective catalyst. *J Catal* **385**, 176–182 (2020).

20. Hwang, S. J., Chen, C. Y. & Zones, S. I. Boron sites in borosilicate zeolites at various stages of hydration studied by solid state NMR spectroscopy. *Journal of Physical Chemistry B* **108**, 18535–18546 (2004).

21. Scholle, K. F. M. G. J. & Veeman, W. S. The influence of hydration on the coordination state of boron in H-Boralite studied by 11B magic angle spinning n.m.r. *Zeolites* **5**, 118–122 (1985).

22. Zaera, F. In-situ and operando spectroscopies for the characterization of catalysts and of mechanisms of catalytic reactions q. (2021) doi:10.1016/j.jcat.2021.08.013.

23. Shi, X. *et al.* Dynamics of Heterogeneous Catalytic Processes at Operando Conditions. **22**, 44 (2023).

24. Copéret, C. Single-Sites and Nanoparticles at Tailored Interfaces Prepared via Surface Organometallic Chemistry from Thermolytic Molecular Precursors. *Acc Chem Res* **52**, 1697–1708 (2019).

25. Gajan, D. & Copéret, C. Silica-supported single-site catalysts: To be or not to be? A conjecture on silica surfaces. *New Journal of Chemistry* **35**, 2403–2408 (2011).

26. Dusselier, M. & Davis, M. E. Small-Pore Zeolites: Synthesis and Catalysis. *Chem Rev* **118**, 5265–5329 (2018).

27. Cundy, C. S. & Cox, P. A. The hydrothermal synthesis of zeolites: History and development from the earliest days to the present time. *Chem Rev* **103**, 663–701 (2003).

28. Wolf, P., Hammond, C., Conrad, S. & Hermans, I. Post-synthetic preparation of Sn-, Ti- and Zr-beta: A facile route to water tolerant, highly active Lewis acidic zeolites. *Dalton Transactions* **43**, 4514–4519 (2014).

29. Yilmaz, B. & Müller, U. Catalytic applications of zeolites in chemical industry. in *Topics in Catalysis* vol. 52 888–895 (2009).

30. Corma, A. & Martínez-Triguero, J. The use of MCM-22 as a cracking zeolitic additive for FCC. *J Catal* **165**, 102–120 (1997).

31. Cheng, J. C. *et al.* Us5453554a. (2011).

32. Rigoreau, J., Laforge, S., Gnep, N. S. & Guisnet, M. Alkylation of toluene with propene over H-MCM-22 zeolite. Location of the main and secondary reactions. *J Catal* **236**, 45–54 (2005).

33. Song, F. *et al.* Highly efficient epoxidation of propylene over a novel Ti-MWW catalyst. in *Studies in Surface Science and Catalysis* vol. 170 1236–1243 (Elsevier Inc., 2007).

34. Ren, L. *et al.* Pillared Sn-MWW Prepared by a Solid-State-Exchange Method and its Use as a Lewis Acid Catalyst. *ChemCatChem* **8**, 1274–1278 (2016).

35. Altvater, N. R. *et al.* B-MWW Zeolite: The Case Against Single-Site Catalysis. *Angewandte Chemie - International Edition* **59**, 6546–6550 (2020).

36. Baerlocher, Ch. & McCusker, L. B. Database of Zeolite Structures. http://www.iza-structure.org/databases/.

37. Kroeker, S. & Stebbins, J. F. Three-coordinated boron-11 chemical shifts in borates. *Inorg Chem* **40**, 6239–6246 (2001).

38. Angel Wong, Y. T. & Bryce, D. L. Recent Advances in 11 B Solid-State Nuclear Magnetic Resonance Spectroscopy of Crystalline Solids. in *Annual Reports on NMR Spectroscopy* vol. 93 213–279 (2018).

39. Leonowicz, M. E., Lawton, J. A., Lawton, S. L. & Rubin, M. K. MCM-22: A molecular sieve with two independent multidimensional channel systems. *Science (1979)* **264**, 1910–1913 (1994).

40. Trebosc, J., Hu, B., Amoureux, J. P. & Gan, Z. Through-space R3-HETCOR experiments between spin-1/2 and half-integer quadrupolar nuclei in solid-state NMR. *Journal of Magnetic Resonance* **186**, 220–227 (2007).

41. Venkatesh, A., Hanrahan, M. P. & Rossini, A. J. Proton detection of MAS solid-state NMR spectra of half-integer quadrupolar nuclei. *Solid State Nucl Magn Reson* **84**, 171–181 (2017).

42. Cunniff, C. Z. *et al.* Investigation of Supported Metal Oxide Species with Shell-Isolated Nanoparticle-Enhanced Raman Spectroscopy. *Journal of Physical Chemistry C* **123**, 25220–25227 (2019).

43. Tošner, Z. *et al.* Computer-intensive simulation of solid-state NMR experiments using SIMPSON. *Journal of Magnetic Resonance* **246**, 79–93 (2014).

44. Bak, M., Rasmussen, J. T. & Nielsen, N. C. SIMPSON: A General Simulation Program for Solid-State NMR Spectroscopy. *Journal of Magnetic Resonance* **147**, 296–330 (2000).

45. Chen, J. *et al.* Regulation of Framework Aluminum Siting and Acid Distribution in H-MCM-22 by Boron Incorporation and Its Effect on the Catalytic Performance in Methanol to Hydrocarbons. *ACS Catal* **6**, 2299–2313 (2016).

46. de Ruiter, R., Kentgens, A. P. M., Grootendorst, J., Jansen, J. C. & van Bekkum, H. Calcination and deboronation of [B]-MFI single crystals. *Zeolites* **13**, 128–138 (1993).

47. Robson, H. E. *Verified Syntheses of Zeolitic Materials*. *Verified Syntheses of Zeolitic Materials* (Elsevier, 2001). doi:10.1016/B978-044450703-7/50151-4.

48. Edén, M., Zhou, D. & Yu, J. Improved double-quantum NMR correlation spectroscopy of dipolar-coupled quadrupolar spins. *Chem Phys Lett* **431**, 397–403 (2006).

49. Wang, Q. *et al.* Double-quantum homonuclear NMR correlation spectroscopy of quadrupolar nuclei subjected to magic-angle spinning and high magnetic field. *Journal of Magnetic Resonance* **200**, 251–260 (2009).

50. Mali, G., Fink, G. & Taulelle, F. Double-quantum homonuclear correlation magic angle sample spinning nuclear magnetic resonance spectroscopy of dipolar-coupled quadrupolar nuclei. *Journal of Chemical Physics* **120**, 2835–2845 (2004).

51. Ashbrook, S. E. & Sneddon, S. New methods and applications in solid-state NMR spectroscopy of quadrupolar nuclei. *J Am Chem Soc* **136**, 15440–15456 (2014).

52. Editors, G. *et al.* Recent advances in solid-state NMR spectroscopy of quadrupolar nuclei. *Physical Chemistry Chemical Physics* **11**, 6892–6905 (2009).

53. Kentgens, A. P. M. A practical guide to solid-state NMR of half-integer quadrupolar nuclei with some applications to disordered systems. *Geoderma* **80**, 271–306 (1997).

54. Gan, Z. *et al.* NMR spectroscopy up to 35.2 T using a series-connected hybrid magnet. *Journal of Magnetic Resonance* **284**, 125–136 (2017).

55. Dorn, R. W. *et al.* Structure Determination of Boron-Based Oxidative Dehydrogenation Heterogeneous Catalysts With Ultrahigh Field 35.2 T 11 B Solid-State NMR Spectroscopy. *ACS Catal* **10**, 13852–13866 (2020).

56. Scholle, K. F. M. G. J. & Veeman, W. S. The influence of hydration on the coordination state of boron in H-Boralite studied by 11B magic angle spinning n.m.r. *Zeolites* **5**, 118–122 (1985).

57. Wiper, P. V., Amelse, J. & Mafra, L. Multinuclear solid-state NMR characterization of the Brønsted/Lewis acid properties in the BP HAMS-1B (H-[B]-ZSM-5) borosilicate molecular sieve using adsorbed TMPO and TBPO probe molecules. *J Catal* **316**, 240–250 (2014).

Chapter 3: Monomeric vs oligomeric vanadium oxide for the oxidative dehydration of propane.

This chapter will be submitted with the title "The Selectivity Controlling Role of the Fast Reoxidation of Vanadium Oxide Sites in the Oxidative Dehydrogenation of Propane". I completed the material synthesis and characterization, collected the kinetic data, and contributed to the experimental direction and data interpretation.

3.1 Introduction: disagreement on vanadium active site structure

Oxidative dehydrogenation (ODH) of propane is a developing method for the on-purpose production of propylene. As propylene is the third most produced chemical by volume, next to only ammonia and ethylene, efficient production of this building block chemical is of great interest to the chemical industry.[1] Despite its process advantages, ODH suffers from overoxidation to CO and CO_2 (CO_x) byproducts at increasing conversion.[2] To improve the performance of ODH catalysts and design materials that will mitigate the formation of byproducts in favor of the desired products, there needs to be a more fundamental understanding of the catalyst structure. These components responsible for activity in heterogeneous catalysis are referred to as active sites, and their exact structures are often debated in literature. For supported vanadium oxide, which is one of the most studied catalysts in ODH, there is still much debate on the structure and mechanism.[3,4]

Synthesis of vanadium catalysts is typically done via a bulk deposition method such as incipient wetness impregnation on an amorphous support.[4,5] This synthesis method has a lack of control in precursor deposition which results in the formation of many different vanadium oxide (vanadia) species on the surface. These species include isolated tetrahedral $(support\text{-}O)_3V{=}O$ with a vanadyl, oligomeric tetrahedral $(support\text{-}O)_{1+x}(V_y\text{-}O)_{2-x}V{=}O$ (where x = 0 or 1 and V_y describes neighboring vanadyl species), polymeric V_2O_5 nanoparticles, and $(support\text{-}O)_{1+x}(V_y\text{-}O)_{2-x}\ V^V(OO)$

(where x = 0, 1, or 2) a peroxo- species.[4,6–8] It is well known that large V_2O_5 nanoparticles lead to low propylene selectivity and preference to CO_x products.[9] These nanoparticles will begin forming at increased vanadium loading. The best performing vanadium catalysts have the highest loading of vanadium possible without forming V_2O_5 nanoparticles, Figure 3.1. This configuration will be referred to as dispersed vanadium which contains isolated and oligomeric vanadyl species. Although the active site in vanadium is identified as these vanadyl species, it is not clear if monomeric or oligomeric vanadium species perform better under reaction conditions. Two major points of disagreement in the vanadium literature to be discussed in this work include the following: 1) the structure of the vanadium active site, isolated or oligomeric vanadyl sites, and 2) the role of the vanadium peroxo species in the mechanistic cycle.

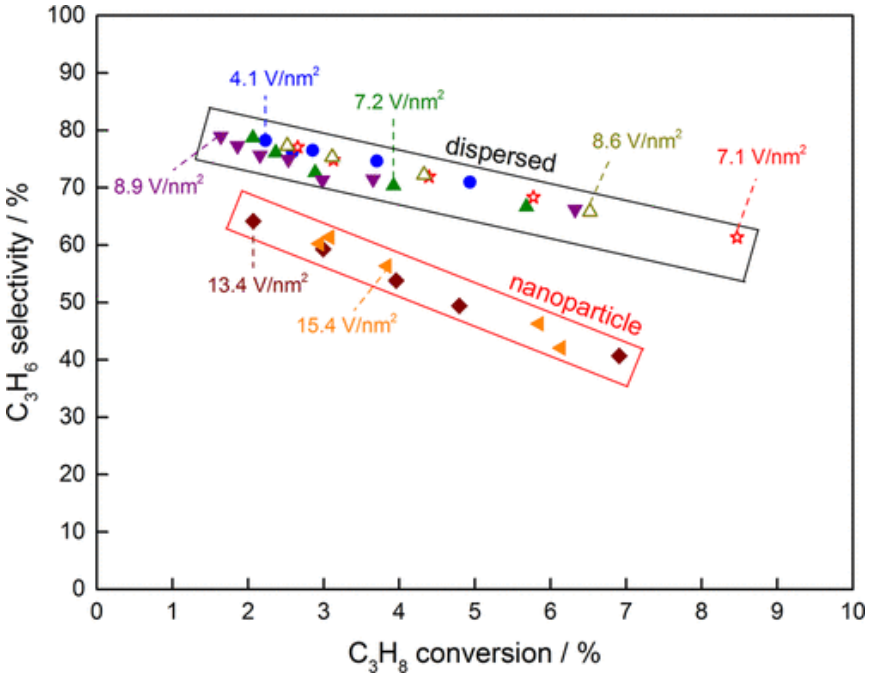

Figure 3.1 Selectivity of propylene as a function of propane conversion for vanadium supported on silica. Catalysts with open symbols are supported on sodium promoted silica. See reference for additional details.[9]

Various studies on the influence of isolated vs polymeric sites have been published in the literature. Here isolated or monomeric vanadyl sites will refer to a single (support-O)$_3$V=O site with all three non-vanadyl oxygens bonded to the support, and oligomeric or polymeric vanadyl refers to a linear chain of (support-O)$_{1+x}$(V$_y$-O)$_{2-x}$V=O sites that are connected to each other through one or two of the non-vanadyl oxygen, through a V–O–V bond as seen in Figure 3.2. Many authors have concluded that the catalytic turnover rates of isolated and oligomeric species are the same and are influenced only by the type of support.[8] The referenced studies use the same bulk synthesis methods on amorphous supports that create an undefined distribution of monomeric and oligomeric sites, so it is unsurprising that no distinction is made between the morphologies given the lack of controlled speciation.[4,5,8]

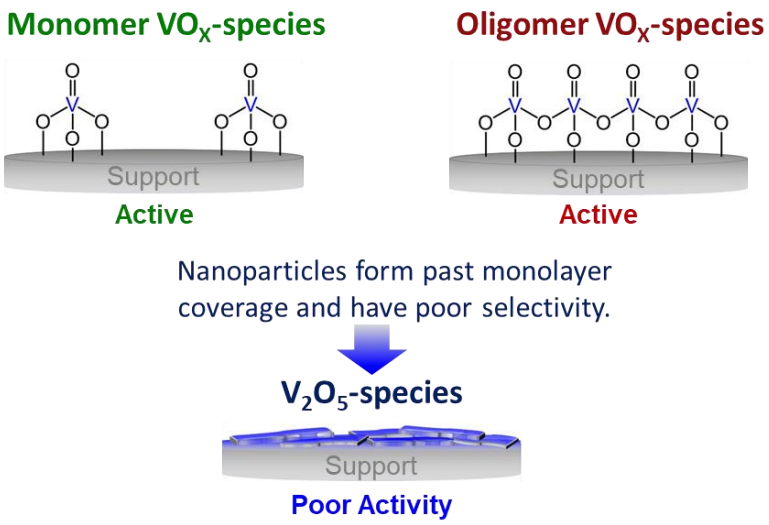

Figure 3.2 Simplified illustration of the different configurations of vanadium oxide species found on supported catalysts. The indicated activity is for the oxidative dehydrogenation of propane to propylene.

By contrast, there is a set of published works that use controlled synthesis with the goal of isolating vanadium sites on silica and high-silicate zeolites. In these studies, the different authors disagree on whether oligomeric vanadyl sites or isolated vanadyl sites have a higher ODH performance, but they do agree that there is a difference in catalytic performance.[10–13] Some studies claiming that isolated vanadium has a higher performance than oligomeric synthesize different loadings of vanadium across different supports that have distinct pore and surface area morphologies.[11,13–16] Comparing the performance of vanadium species across different supports that range from mesoporous to microporous silica materials is an effective way of discovering novel supports for vanadium.[17,18] However, since multiple characteristics of the support other than the vanadyl structure, isolated vanadyl sites cannot be conclusively responsible for differences in catalytic performance. Some studies crediting isolated vanadyl with higher propylene selectivity produce materials that are not isolated and have instead small oligomers therefore being unable to distinguish the reactivity of the two vanadium structures. [16,19] Several studies claim that oligomeric vanadium structures have a higher turnover frequency compared to isolated vanadium.[10,20–22] Sauer and coworkers observed that adjacent vanadia cooperatively dehydrogenate propane by changing oxidation state from V^{+5}/V^{+5} to V^{+4}/V^{+4} as opposed to an isolated site that would change from V^{+5} to V^{+3} to dehydrogenate the propane twice.[22] This alternate route for partial reduction of adjacent vanadium sites instead of reduction from V^{+5} to V^{+3} is a more favorable pathway, due to lower barriers and the formation of more stable products.

In addition to the active site(s) structure disagreement, an additional peroxo-vanadium species has been proposed by several authors to be a part of the mechanism.[12,20,23] As an added degree of difficulty this species is highly reactive and cannot be observed on the catalyst at ambient conditions pre- or post- reaction. The V(O–O) structure is described as more reactive than the

vanadyl bond (V=O) and potentially responsible for propylene overoxidation, water removal, and surface species reoxidation.[12,23–25] Its role in the redox ability of vanadium is of the greatest interest here and will be discussed further. The peroxo-vanadium species is short lived and in low concentrations adding to the difficulty of observing it in-situ. It has only ever been observed spectroscopically at 90 K and will easily decompose above 170 K.[25] Other well-respected names in vanadium literature, including Wachs, do not agree with the existence of the peroxo- species largely based on the lack of spectroscopic evidence at relevant reaction conditions.[26] Regardless of the varying opinions in literature, the existence of this peroxo species may play a key role in the regeneration of the supported vanadium catalyzed ODH mechanism and be a determining factor in the selectivity of propylene.

In this work, controlled synthesis of vanadium is tailored and applied to create monomeric and short chain oligomers, as evidenced by spectroscopic characterization, to then compare the catalytic performance during propane ODH. This synthesis was done using a well-characterized boron-doped zeolite, from Chapter 2, to control the vanadium speciation. To better understand the mechanism behind the different vanadium structures kinetic modeling and density functional theory will be applied. These methods and discoveries can be applied to the future work of making a better designed vanadium-containing catalyst for the ODH of propane.

3.2 Methods

3.2.1 Material synthesis

B-MWW, a boron doped MCM-22 type zeolite, was hydrothermally synthesized using the previously described method in Ch. 2.[27,28] This zeolite was then deboronated, called **deB-MWW**, by treating in nitric acid in a procedure adapted from Tsapatsis.[28] For every 1 gram of material, 50 mL of 6 M HNO_3 was used, and the mixture was stirred at room temperature for 24 hr before being

washed via centrifuge and then dried at 70 °C. The acid treatment was then repeated once. Next, **TMS/deB-MWW** was synthesized using vapor phase grafting. First, the deB-MWW was dehydrated overnight under dynamic vacuum on a Schlenk line at 200 °C to remove any oxygen or moisture. Twice distilled N, N-bis(trimethylsilyl)methylamine, called TMS here, (Sigma Aldrich) was added to the dried deB-MWW via a vapor phase transfer. The amount of TMS added was determined based on the estimated silanol density of the deB-MWW. The silanol density of $SiO_{2\text{-}(200)}$ was used as an estimation of the zeolite's silanol density. Additionally, the TMS was added in excess at five times the molar equivalent based on the estimated silanol density. The TMS was left to react with the solid at room temperature for 30 min. Next, the material was heated at 60 °C under dynamic vacuum for 1 hr. to remove any unreacted precursor.

To synthesize **V-MWW**, a method called solid-state incorporation (SSI) was modified from literature and used here.[29–31] First, the deB-MWW, which was synthesized and maintained in a moisture and oxygen free environment, is transferred to a glovebox, which has an inert atmosphere of N_2 with $\leq$ 1 ppm of H_2O and O_2. Next, the appropriate amounts of vanadium (III) acetylacetonate ($V(acac)_3$) (Sigma-Aldrich, 97% purity) was added to 100-200 mg batches of the deB-MWW. The two solids were ground together for 10 min with a mortar and pestle. After thorough mixing, the material was transferred to a quartz reactor and sealed while still in the glovebox. The sealed reactor was transferred to a tube furnace where the following heat treatment was carried out using dry gases. As the sample was heated from room temperature to 550 °C at a ramp rate of 1 °C/min., dry N_2 was fed to the reactor. The sample was held at 550 °C for 3 hr under N_2 flow before switching the feed gas to dry O_2 and flowing for another 3 hr. at the same temperature of 550 °C. Resulting samples were called xV-MWW where x is the wt.% loading of vanadium as determined by elemental analysis.

Vanadium on amorphous silica, **V/SiO_2**, was synthesized via incipient wetness impregnation (IWI) according to a literature procedure.[32] Silica-200, in batches of 100-500 mg, was dried overnight at 120 °C before being moved to an inert purge box environment fed with dry N_2. Next, vanadium (V) triisopropoxide oxide (Alfa Aesar, 96% purity) was mixed with a dry isopropanol solvent. The volume of vanadium precursor was determined by the desired vanadium weight loading, and the total volume of solution was determined based on the incipient wetness point of silica which was 1.4 mL/g. After incorporation, the material was calcined in a muffle furnace at a temperature of 550 °C for 3 hr with a ramp rate of 1 °C/min in dry air. The resulting sample was referred to as xV/SiO_2, where x is the weight percent loading of vanadium as determined by bulk elemental analysis.

3.2.2 Materials characterization

Fourier transform **infrared spectroscopy** (IR) was recorded on a Bruker Alpha spectrometer with a 2 cm^{-1} resolution. The sample was mixed with KBr, which does not produce a signal in IR, and pressed into a self-supporting wafer. The resulting spectra were normalized to the silica overtones. **Diffuse reflectance ultraviolet-visible spectroscopy** (DRUV-vis) was collected on an Ocean Optics Maya 200 spectrometer equipped with a UV-vis deuterium/halogen light source, DH-2000-BAL from Mikropack. Samples were loaded onto a $BaSO_4$ background which has no signal in DRUV-vis. All IR and UV-vis were recorded in a glovebox with an N_2 atmosphere and ≤ 1 ppm of H_2O and O_2. All samples were fully dehydrated under dynamic vacuum before measurement.

Raman spectra were recorded on a Renishaw InVia Raman spectrometer with a 785 nm excitation laser equipped with a 1200 L mm^{-1} grating. Spectra were taken at a range of 250-1200 cm^{-1} and a dispersion of 1.36565 cm^{-1} $pixel^{-1}$. All samples were measured at ambient temperature

and atmosphere unless otherwise noted. **Inductively coupled plasma – optical emission spectroscopy** (ICP-OES) was done for the bulk elemental analysis of vanadium and boron loading. Samples were weighed out in 15-20 mg per analyte, and three replicates were measured for each sample. Samples were completely digested in 48% HF before being diluted with 18 MΩ H_2O. Analysis was done on an ICP-OES with all borosilicate components replaced with Teflon equivalents to avoid etching of the glass by the HF. Three wavelengths were averaged for each element measured and the three replicates were used to determine the measurement error.

3.2.3 Catalytic activity

Kinetic measurements were done on a Microactive-Effi reactor in a plug flow configuration. A total of 50-120 mg of catalyst were mixed with an inert diluent of passivated SiC in a mass ratio of 1:2 (catalyst/SiC). The catalyst and SiC was pelletized to 425-600 μm unless otherwise noted in the text. The material was packed in a quartz reactor tube with an inner diameter of 9 mm. The catalyst bed was supported on quartz wool and, the void space was pack with quartz chips of the same 425-600 μm particle size. The reaction was carried out at 480-500 °C with gas composition of 3:6:11 O_2:C_3H_8:N_2 where all gases are ultra-high purity (UHP) grade. A thermocouple that was in contact with the catalyst bed was used to monitor the temperature during reaction. The total volumetric flowrate of gas was varied 20-120 sccm to vary the contact time. The effluent gas from the reactor was analyzed with an online Shimadzu 2010 GC equipped with a thermal conductivity detector (TCD) and flame ionization detector (FID). The carbon balance was closed within ±2%.

3.2.4 Computational methods and kinetic modeling

Unrestricted **density functional theory** (DFT) calculations were performed in Gaussian 16 using the B3LYP function and the triple-ζ valance with polarization (def2tzvp) basis set.[33–36]

Grimme's dispersive D3 correlations were employed to account for the Van der Waals interactions.[37] To verify the absence of imaginary frequencies in local minima and the presence of a single imaginary frequency in transition states, frequencies were computed. All reported energies are enthalpies at 0 K, including zero-point vibrational energy corrections. Biradical systems were treated both as open-shell singlets and triplets. The energy of open-shell singlets was calculated using the broken-symmetry approach as reported by Rozanska.[20] The models of monomeric and oligomeric vanadyl sites supported on a silica support have the two formulas shown in Figure 3.3 (a) $V_1Si_9H_{13}O_{14}$ and (b) $V_2Si_8H_{12}O_{15}$.[22] In the oligomeric model, the two vanadyl groups are near parallel as is the case in V_2O_5(010) which is the natural cleavage plane for V_2O_5 particles, see Figure 3.3 (c). As a benchmark, a cubic silsesquinxane model was used to include two neighboring vanadyl groups which results in a distance of 5.4 Å between the vanadyl oxygens. This distance is much larger than their distance in V_2O_5(010) as shown in Figure 3.3 (c) and (d).

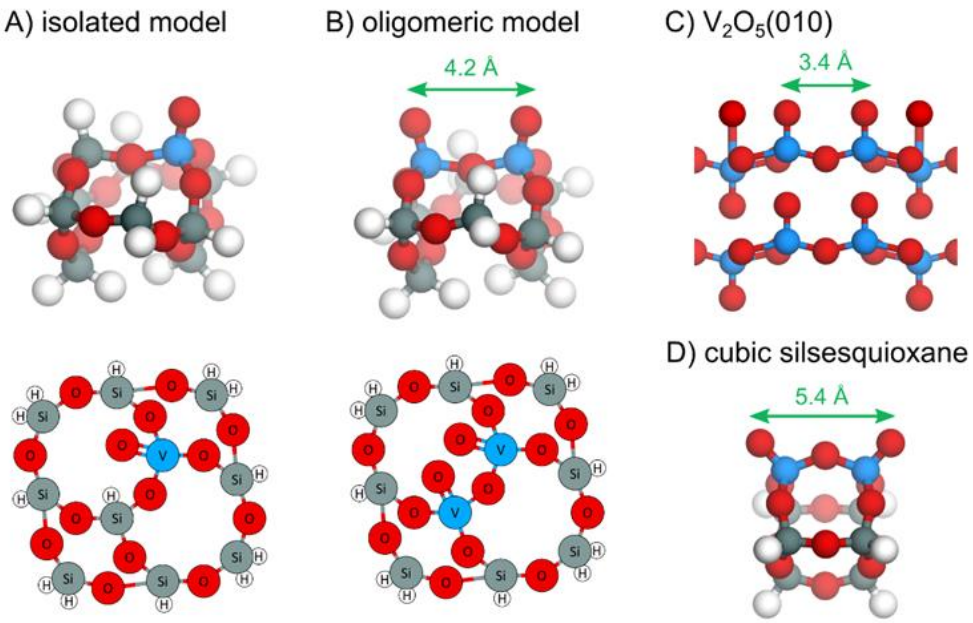

Figure 3.3 DFT-optimized 3D structures of monomeric and oligomeric vanadia on silica. (a) and (b) are the implemented models along with simplified 2D sketches showing the connectivity. (c) Two layers of V_2O_5(010) surface. (d) Cubic silsesquioxane-based model containing two neighboring vanadyl groups. The green arrows represent the distance between two neighboring vanadyl oxygens.

Kinetic modeling was done by calculating Gibbs free energies of reaction (ΔG_{rxn}) and activation ($\Delta G^{\ddagger}$) to find equilibrium constants and rate constants according to transition state theory, respectively. The ideal gas approximation, with contributions from the translational, rotational, and vibrational degrees of freedom, was used to calculate the Gibbs free energies of gas molecules. For the vanadium sites and other adsorbates, Gibbs free energies were calculated using to the harmonic approximation, with contributions from the vibrational degrees of freedom only. The above listed calculations were done using the Python Multiscale Thermochemistry Toolbox (pMuTT). A system of mass balances was written assuming an isothermal, isobaric continuously stirred tank reactor (CSTR) model, and it was solved at steady state using MATLAB's fsolve function.

3.3 Results and discussion

3.3.1 Vanadium zeolite synthesis

As stated above the synthesis of vanadium containing zeolites to evaluate monomeric vs oligomeric vanadyl sites is not new to this work. Previous vanadium-doped zeolite studies have shown how difficult it is to control the incorporation of vanadium into zeolites such that the vanadia are truly isolated.[14,38,39] The previous study reported in Chapter 2 details the characterization of boron doped MCM-22, called B-MWW. This material has primarily isolated boron sites located inside the zeolite framework.[27,40] Using this material as a starting point, the highly structured support with its dispersed boron T-sites can be applied to design the desired vanadia materials.

The deboronation was done at room temperature to maintain the integrity of the zeolite framework while removing the boron sites. ICP-OES determined that the Si/B ratio after acid treatment went from 13 to 1300 indicating that essentially all boron was removed. Additionally, X-ray photoelectron spectroscopy (XPS) showed no signal for boron, and IR in Figure 3.4 (red trace) showed no distinct B-OH peak (3700 cm^{-1}) for deB-MWW. The broad peak in Figure 3.4 between 3700-3100 cm^{-1}, which increased after boron removal, corresponds to hydrogen bonded silanol nests caused partially by defect sites in the framework from the removal of boron sites. In addition to the silanol nest, the zeolite has external framework silanol sites (shoulder at 3745 cm^{-1}) which can act as anchoring sites for a vanadium precursor. To prevent vanadium from anchoring externally and instead direct the precursor to bond in the internal defect sites created by boron removal, a silylating agent is added to cap these external sites. TMS is too large to enter the pores of MWW, so it will selectively cover the external silanol sites but not the internal nests. The silylated materials in Figure 3.4 (black trace) shows the successfully grafted TMS by the C-H

stretch just below 3000 cm^{-1}, and while the shoulder at 3745 cm^{-1} decreased, the broad signal corresponding to the silanol nests still exists showing that the selective grafting to TMS was successful.

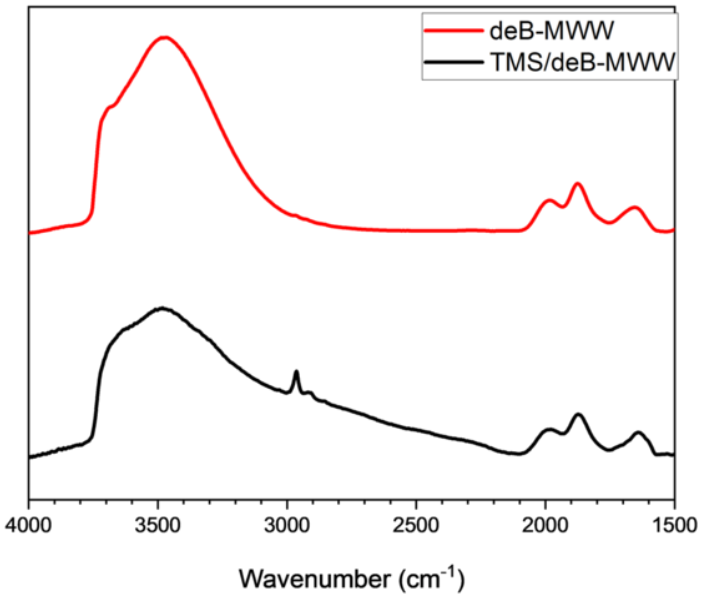

Figure 3.4 Transmission IR of deB-MWW (red trace) and the silylated TMS/deB-MWW (black trace) showing the addition of the silylating agent and reduction in the external silanol groups.

Next, $V(acac)_3$ was added to the TMS/deB-MWW in different amounts via SSI to create V-MWW with different loadings of vanadium. The loadings of 1.3, 2.1, and 2.4 wt.% were confirmed by ICP-OES as shown in Table 3.1. The goal is to synthesize isolated vanadium by replacing the isolated boron sites with vanadium. To achieve this incorporation the vanadium precursor must be able to diffuse into the zeolite channels and cages. This crucial step in the synthesis is limited by the size and mobility of the precursor. After the mechanical incorporation of the $V(acac)_3$, the material cannot simply be treated with a traditional calcination. Instead, the heat treatment under N_2 before switching to O_2 allows for the mobility of the vanadium precursor through the zeolite. While the TMS remains capping external silanol sites, the V^{+3} precursor will

volatilize under the high temperatures and migrate to the open silanol nests to anchor. This heat treatment and calcination method has been shown to work with Sn incorporation to a zeolite, where the precursor was able to properly diffuse into the framework in its reduced state and disperse within the pores. Figure 3.5 shows the consumption of silanol nests after vanadium incorporation which evidences the successful incorporation of vanadium into the defect sites created by removing boron. The 2.1V-MWW shows more consumption of the broad silanol peak when compared to 1.3V-MWW as expected for a higher loading of vanadium. Additionally, 4V/SiO_2 was synthesized using IWI for comparison.

Table 3.1 Bulk elemental analysis results for vanadium doped zeolites and 4V/SiO_2. The error is determined from triplicate measurements of each sample.

Name	**V (wt.%)**
1.3V-MWW	1.29 ± 0.02
2.1V-MWW	2.13 ± 0.03
2.4V-MWW	2.38 ± 0.03
4V/SiO_2	3.84 ± 0.04

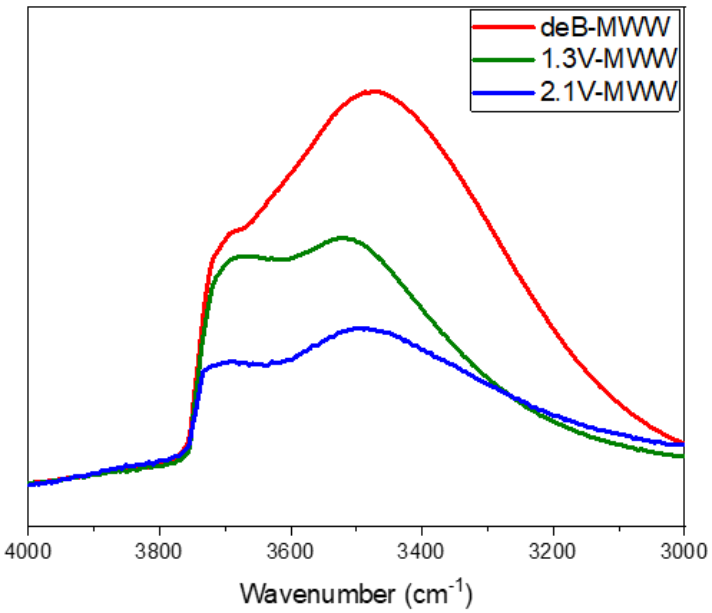

Figure 3.5 Transmission IR spectra of deboronated MWW and vanadium incorporated MWW at loadings of 1.3 wt.% and 2.1 wt.% as labeled.

3.3.2 Characterization of monomeric vs polymeric vanadyl

To confirm the structure of vanadium incorporated into the zeolite, a series of Raman and DRUV-vis experiments were performed on the materials. Raman spectra of the three different V-MWW in Table 3.1 and 4V/SiO_2 exhibit a vanadyl V=O stretch at 1040 cm^{-1} which is a characteristic stretch of dispersed vanadyl sites.[41] Raman analysis also shows that 2.4V-MWW had an additional peak at 998 cm^{-1} which was from V_2O_5 nanoparticles as seen in Figure 3.6. The Raman spectra conclude that 1.3V-MWW, 2.1V-MWW, and 4V/SiO_2 have dispersed vanadyl sites in monomeric and oligomeric configurations in unspecified fractions. The 2.4V-MWW has V_2O_5 nanoparticles which are known to have poor selectivity in propane ODH.

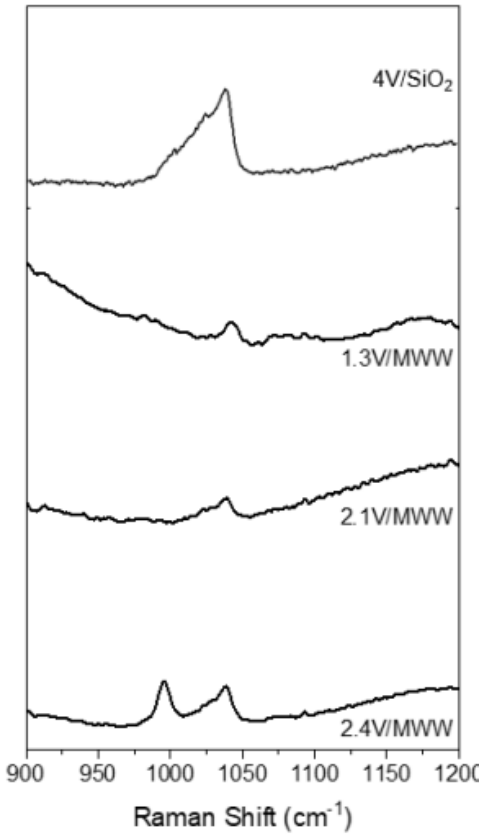

Figure 3.6 Raman spectra taken with a 785 nm laser showing dispersed vanadyl stretch at 1040 cm^{-1} and V_2O_5 vanadyl stretch at 998 cm^{-1}. The vanadium loading and support are listed next to each trace.

To further investigate the vanadium structure in the two lower loading vanadium zeolites, DRUV-vis was done. UV-vis provides information about the local chemical environment of vanadium atoms which allows determination of the aggregation of vanadium atoms since their edge energy changes whether they are monomeric, oligomeric, or nanoparticles. Wachs has done extensive studies on supported vanadia and how the edge energy will change with the vanadyl chain length.[7] Based on these studies the UV-vis of 1.3V-MWW has an edge energy of 3.6 eV which corresponds to what is reported for monomeric VO_4 vanadium species, Figure 3.7. The 2.1V-MWW has an additional shoulder seen in the UV-vis between 350-500 nm. This signal is in the same range as that seen in $4V/SiO_2$ and is assigned to oligomeric or polymeric vanadia. So,

2.1V-MWW has both isolated and small oligomer chain VO_4 species as confirmed by UV-vis. The edge energy for $4V/SiO_2$ is consistent with the vanadia structure known for silica-supported vanadium. The UV-vis of 2.4V-MWW is shown in Figure B.1. While the 2.4V-MWW and $4V/SiO_2$ species do not show a distinct peak for monomeric vanadyl sites, their presence on the support cannot be excluded. Based on all the above spectroscopic data, 1.3V-MWW is classified as having primarily isolated vanadyl sites, 2.1V-MWW and $4V/SiO_2$ have both isolated and oligomeric sites, and 2.4V-MWW has isolated, oligomeric, and nanoparticles of VO_x on the support. Again, the $4V/SiO_2$ serves as a benchmark for vanadium structure characterization and reactivity.

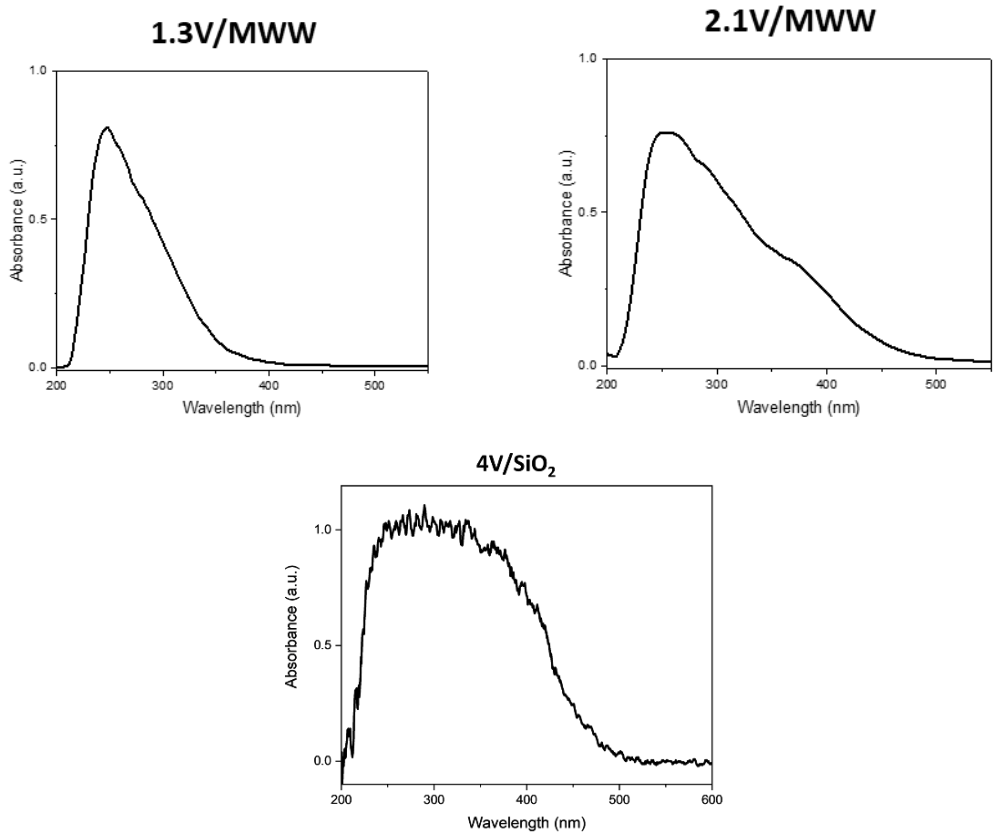

Figure 3.7 Diffuse reflectance ultraviolet visible spectra of 1.3V-MWW, 2.1V-MWW, and 4V/SiO2, which have the edge energies of 3.6, 2.8, and 2.6 eV, respectively.

3.3.3 Catalytic activity

After achieving the successful synthesis of monomeric and oligomeric vanadium species in a zeolite framework, the next step is to analyze the catalytic reactivity of these separate species. The catalytic performance of the above discussed materials was done at 500 °C and is shown in Figure 3.8. The zeolite with primarily isolated vanadyl sites, 1.3V-MWW, exhibited lower activity and propylene selectivity when compared to the other materials. The 2.1V-MWW showed a 9% improvement in propylene selectivity, at 3% propane conversion. This significant improvement in selectivity is attributed to the activity of oligomeric vanadyl species in the 2.1V-MWW. This catalytic data clearly shows that the presence of oligomeric vanadyl species improved the performance of vanadium materials for the ODH of propane. This conclusion is supported by previous studies where Basset and coworkers also observed a decrease in propylene selectivity on their single site VO_x silica material.[11] As expected, $4V/SiO_2$, which has a high fraction of polymeric vanadia, maintained the high selectivity to propylene with enhanced activity. The reactivity of 2.4V-MWW is shown in Figure B.2. This observation of how significantly the presence of oligomeric species impacts ODH performance prompts further investigation into the catalytic cycle over monomeric and oligomeric vanadyl sites. The following section details the computational approach to this investigation.

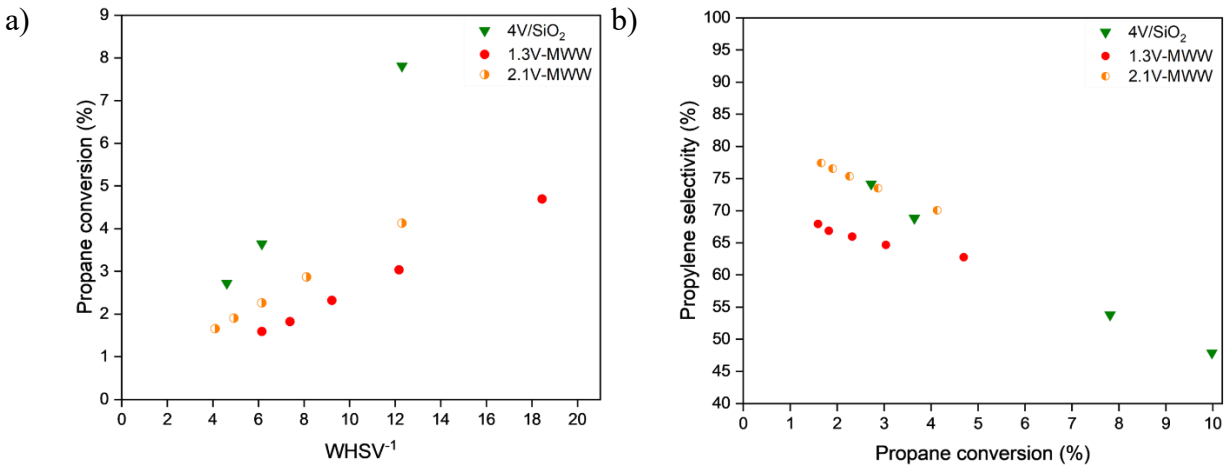

Figure 3.8 Catalytic reactivity results collected at 500 °C with 30% C_3H_8, 15% O_2, and the balance of N_2 with 50-100 mg of catalyst. (a) The rate is shown as propane conversion as a function of inverse weight hourly space velocity ($WHSV^{-1}$), and (b) is the propylene selectivity trend as a function of propane conversion.

3.4 Computational modeling

3.4.1. Reaction Mechanism via DFT

To find the source of the different propylene selectivity between the 1.3V-MWW and 2.1V-MWW, their catalytic cycles and corresponding barriers were modeled via DFT. For simplicity, 1.3V-MWW was modeled as a single vanadyl site (monomeric), and 2.1V-MWW was modeled as two adjacent vanadyl sites bonded through a bridging oxygen atom (dimeric or oligomeric). It is possible that 1.3V-MWW contains a small fraction of oligomeric species, but spectroscopic characterization indicates that it is primarily isolated. As stated previously, 2.1V-MWW likely has a portion of isolated sites, and the oligomers likely vary in length instead of being uniformly dimeric. Knowing the qualifiers, the following mechanisms are modeled to demonstrate the influence of monomeric to oligomeric vanadium which is the key difference in the two zeolite materials. The mechanisms for oxidative dehydrogenation of propane are shown in Scheme 3.1. The catalytic cycles for both models have an overall reaction of $2\ C_3H_8 + O_2 \rightarrow 2\ C_3H_6 + 2\ H_2O$.

First, a hydrogen atom is abstracted from the secondary carbon of propane at a vanadyl site (V^{V}=O) to form an isopropyl radical. This rate-determining step has a calculated activation barrier of 134 kJ/mol (monomeric) and 124 kJ/mol (oligomeric). The oligomeric value is consistent with the reported experimental values and computational results for propane ODH on V/SiO_2 materials. After this step, the vanadyl in both cases is reduced from V^{+5}=O to V^{+4}-OH. The oxygen bridging the vanadium atom and silica support was also considered as a point for abstracting hydrogen, but the barrier for the monomeric model increased by 54 kJ/mol to a total of 188 kJ/mol. This result suggests vanadyl oxygen in the preferred site for hydrogen abstraction. Next, a spin-crossing from the single to triplet state takes place in an endothermic step for only 5 kJ/mol. In the second hydrogen abstraction on V^{+4}-OH, the isopropyl radical is converted to propylene with an activation barrier of 42 kJ/mol (monomeric) and 35 kJ/mol (oligomeric). With this step, water is produced and V^{+4}-OH is reduced further to V^{+3}. The possibility of the neighboring V^{+5}=O activating the isopropyl radical in the dimer model was also considered, and the two pathways have similar barriers. Next, the V^{+3} is oxidized to V^{+5} by the gas phase oxygen and forms a peroxo-vanadium species, V^{+5}-(O-O). The peroxo-species can in turn activate propane to propylene via two consecutive hydrogen abstractions converting the vanadium back to V^{+5}=O. The first of these two abstractions had a barrier of 115 kJ/mol or 97 kJ/mol on the monomeric and dimeric models respectively, and the second abstraction requires 24-28 kJ/mol. A parallel pathway for the peroxo species can activate propylene to propylene oxide with an activation of 73-75 kJ/mol. This propylene oxide route is more favorable for propylene activation than the direct hydrogen abstraction to form an allyl radical, which has barriers of 119 and 109 kJ/mol for the monomeric and dimeric (V^{+5}=O) models, respectively. The propylene oxide route also converts the V^{+5}-(O-O) to V^{+5}=O restoring the vanadyl.

Given the above observations, the higher activity of oligomeric vanadium in 2.1V-MWW may be due to its ability to abstract hydrogen atoms at lower activation energies than the isolated sites. At the same time the activation energy to form propylene oxide from propylene stays relatively the same, resulting in oligomeric vanadia being more selective. The alternative route for converting V^{+5}-(O-O) to V^{+5}=O on oligomeric vanadium active sites leads to this enhanced selectivity to propylene.

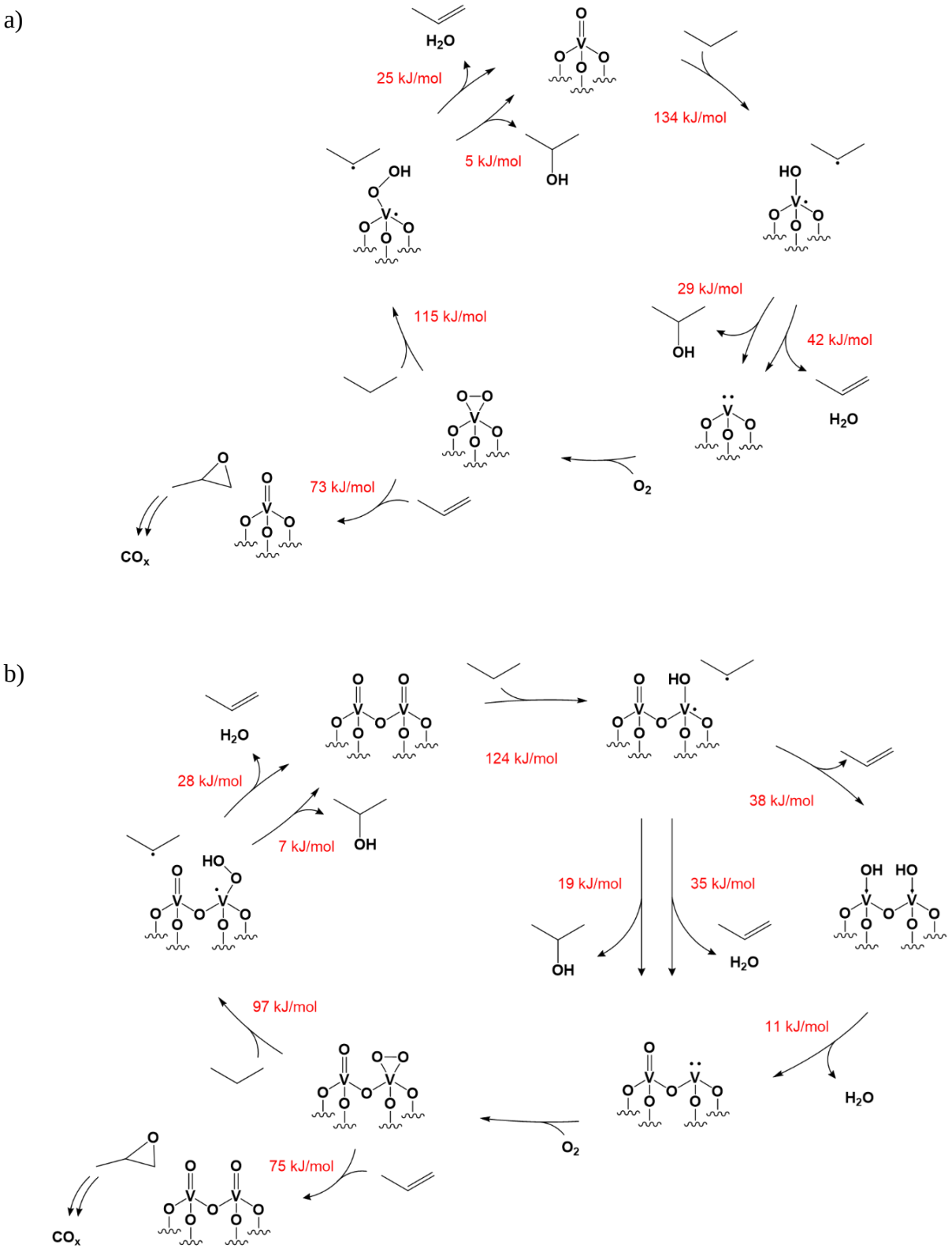

Scheme 3.1 Proposed mechanisms for propane oxidative dehydrogenation reaction cycle occurring over a (a) single vanadyl site and (b) a dimeric vanadyl site. The activation energies are shown next to the different steps and are referenced at 0 K.

3.4.2 Kinetic modeling

The computational results indicated that there were differences in the hydrogen abstraction barriers between the monomeric and dimeric models. To investigate whether this difference could account for the experimental difference in catalytic activity between the two systems, a simplified DFT-derived kinetic model was built to generate the selectivity-conversion trends based on the following mechanistic steps.

1. $V^{V}{=}O + C_3H_8 \rightarrow V^{IV}\text{-}OH + C_3H_7\bullet \rightarrow V^{V}\text{-}(OO) + C_3H_6$ $\quad k = k_1 K_{C3H8/V=O} p_{C3H8} \theta_*$
2. $V^{V}\text{-}(OO) + C_3H_8 \rightarrow V^{IV}\text{-}OOH + C_3H_7\bullet \rightarrow V^{V}{=}O + C_3H_6$ $\quad k = k_2 K_{C3H8/VOO} p_{C3H8} \theta_\#$
3. $V^{V}\text{-}(OO) + C_3H_6 \rightarrow V^{V}{=}O + C_3H_6O$ $\quad k = k_3 K_{C3H6/VOO} p_{C3H6} \theta_\#$

Here k_i is the rate constant of step i, $K_{i/j}$ is the adsorption equilibrium constant of species i on site j, and θ_* and $\theta_\#$ refer to the population of vanadyl and peroxo-vanadium sites, respectively, as fractions of the total vanadium sites. The reactor was modeled as an isothermal, isobaric CSTR (500 °C, 1 bar) with an inlet feed of $C_3H_8/O_2/N_2$ = 6:3:11. A mass balance was also written to conserve the propane, propylene, and vanadium sites. These balances were solved simultaneously at steady state to obtain the propane conversion, corresponding propylene selectivity, and $\theta_\#$ for any space-time yield. The selectivity-conversion trend predicted by the kinetic model, shown in Figure 3.9, replicated the superior performance of the dimeric configuration over the isolated model. The model showed that the oligomeric vanadyl sites had a propylene selectivity 5-7% higher than the monomeric at a propane conversion of 1.5-5%. The oligomeric 2.1V-MWW experimentally had a propylene selectivity 9% higher than the isolated 1.3V-MWW at the same conversion range. While the general trend of the model agreed with the experimental data, the product selectivity of both systems was well overestimated at low conversions. The y-intercept of

the model predicts 100% selectivity to propylene approaching zero conversion which is not consistent with the experimental data if it was extrapolated. This inconsistency showed a limitation in the kinetic model since it did not consider any additional product from propane activation besides propylene. Propylene oxide – the only considered byproduct in the kinetic model – is the result of propylene activation, not propane activation.

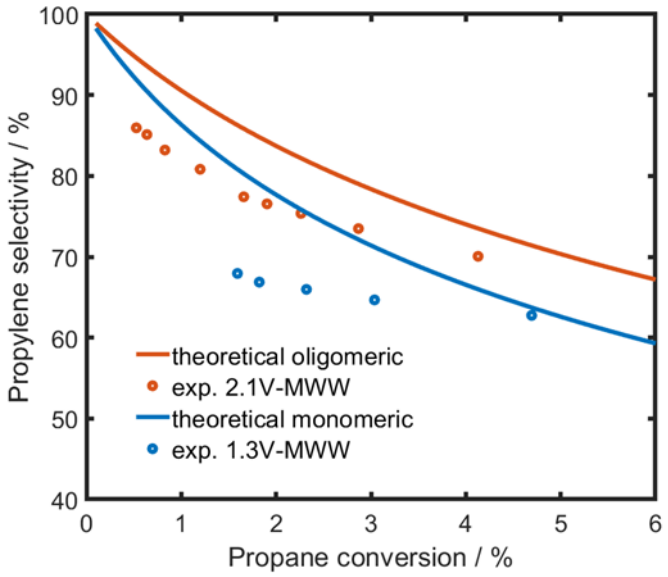

Figure 3.9 Propylene selectivity as a function of propane conversion at 500 °C for 1.3V-MWW and 2.1V-MWW. Solid lines indicate results from the DFT-derived kinetic model, and symbols represent the experimental data.

When considering alternate pathways for propane activation, the formation of isopropanol (IPA) from isopropyl radicals on V^{IV}-OH or V^{IV}-OOH sites was found to be very favorable, Scheme 3.2. Once formed IPA was either reduced to acetone, which then rapidly decomposed to CO_x products, or formed propylene in a dehydration step, Scheme 3.2. This balance between the selectivity of IPA to acetone or propylene could explain the lower selectivity to propylene in the experimental data relative to the implemented kinetic model. Moreover, the model predicted that IPA more readily formed propylene over a dimeric vanadium structure than over the isolated structure, which was in line with the experimental observation that catalysts containing oligomeric sites were more selective to propylene than the ones containing only isolated sites. However, the barriers shown in Scheme 3.2 indicate that vanadium sites preferentially activated IPA to acetone, not propylene. When considering the cycle on the isolated model, Scheme 3.2 (a), the IPA route to acetone was more favorable by at least 17 kJ/mol than its route to propylene. This result implies that isolated vanadia alone could not form propylene as the major product, which was in disagreement with the experimentally observed behavior of 1.3V-MWW. To resolve this disagreement, the hypothesis was that a fraction of the formed IPA was dehydrated to propylene on the acid sites of the support itself. Calculations show that IPA could be dehydrated to propylene on silanol sites with an activation barrier of 179 kJ/mol. Silanol groups have no redox ability, so they only activate IPA to propylene and not to acetone. Our findings indicate that supports are integral parts to the propane ODH catalytic cycle, which encouraged a set of dilution experiments to explore this claim further.

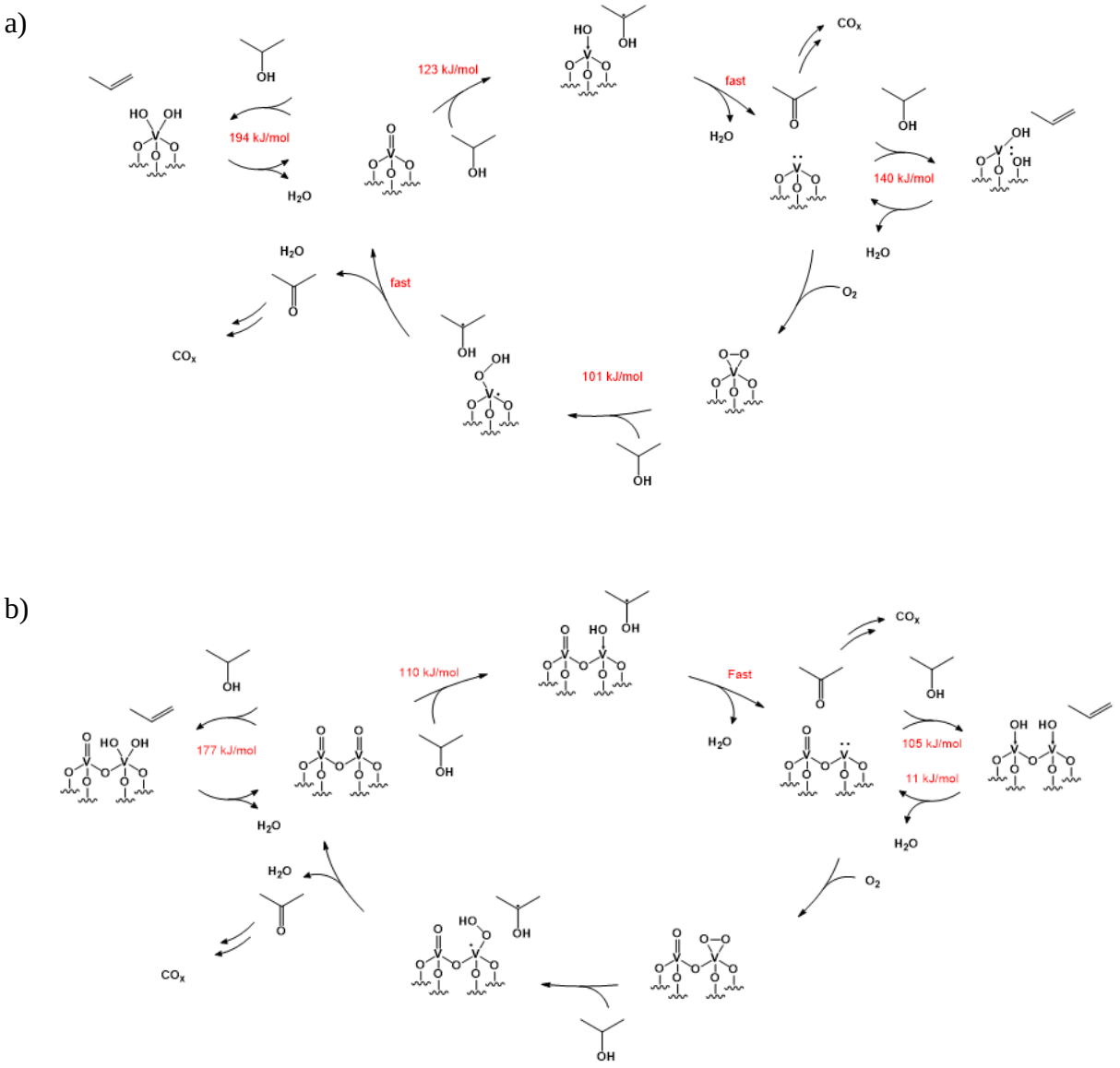

Scheme 3.2 Proposed mechanism for propane oxidative dehydrogenation reaction cycle including isopropanol activation occurring over a (a) single vanadyl site and (b) a dimeric vanadyl site. The activation energies are shown by the different steps and are referenced at activation energy barriers at 0 K.

3.5 Dilution experiments

To further investigate the role of the IPA pathways and the role of supports in the propane ODH catalytic cycle over supported vanadia, a series of dilution experiments were performed with silica supported vanadium to determine the influence of support acidity on IPA activation and propylene selectivity. Wachs reported the difference in IPA conversion over various supports and V_2O_5 showing that the supports with higher acidity have improved selectivity to propylene. Since IPA dehydrates over silanol groups the addition of bare silica to a V/SiO_2 catalyst bed was expected to increase the selectivity to propylene. The materials used in the following experiments were $4V/SiO_2$ (with dispersed oligomeric vanadyl sites) and $8V/SiO_2$ (with nanoparticles of V_2O_5). The vanadium structures on these two materials were confirmed with Raman spectroscopy. This experiment was done using a physical mixture of two different diluents with different acidities. Passivated SiC was used as an inert diluent to benchmark catalyst performance, and bare SiO_2-200 was used as a diluent with mild acidity. The background activity of these two diluents was determined by packing a catalyst bed with each neat diluent and tested at ODH conditions at the highest contact time used in the reactivity experiments. The background activity of SiC and SiO_2 was recorded as less than 1% propane conversion at 480 °C. This low background reactivity ensures that any propane activation seen in the dilution experiments was from the vanadium catalyst and not the diluent.

The current mechanism in Scheme 3.2 shows that the majority of the propane is converted to IPA, which is then converted to acetone or propylene over a vanadium site. The conversion of IPA to acetone, especially on isolated sites, was more favorable than its conversion to propylene. For the propylene selectivity predicted by the model to match the experimental data, the IPA must dehydrate to propylene over acid sites next to the vanadyl sites. Computational results indicate that

silanol sites can convert IPA preferentially to propylene. IPA dehydration to propylene over silica has been studied previously. The addition of bare silica to the supported vanadium catalyst would increase the acidity of the catalyst bed by providing additional silanol sites to dehydrate the IPA formed by the vanadium sites. To test this $8V/SiO_2$ and $4V/SiO_2$ were each mixed with SiO_2 (1:2 by mass). To improve the proximity of the catalyst and diluent, the powders were physically mixed prior to pelletizing unless otherwise noted.

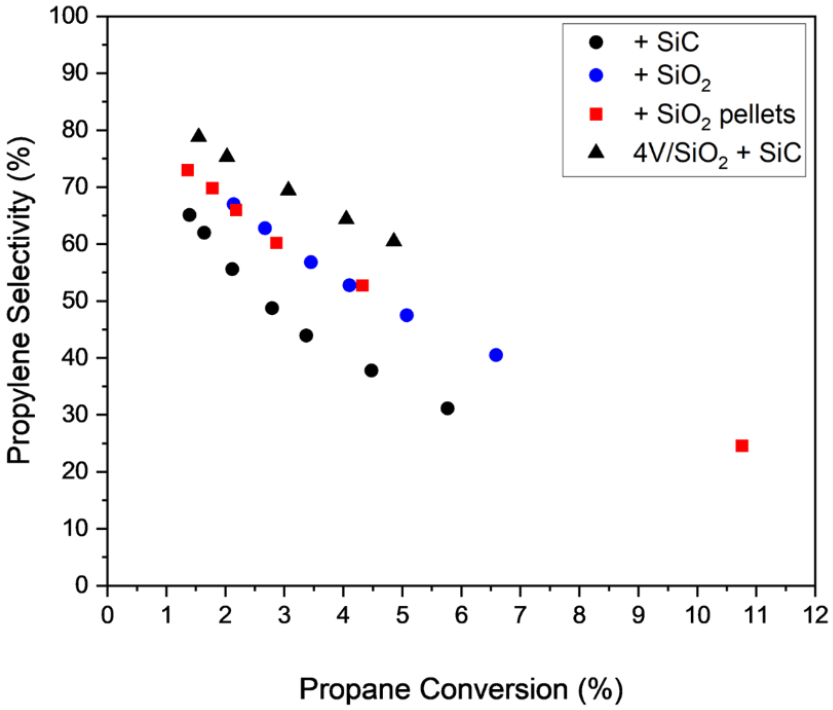

Figure 3.10 Propylene selectivity as a function of propane conversion for $8V/SiO_2$ with labeled diluents and for $4V/SiO_2$. Reactions were done at 480 °C with 30% C_3H_8, 15% O_2, and the balance of N_2 with 100-120 mg catalyst.

Figure 3.10 shows that 8V/SiO_2 (black circles) had lower selectivity than 4V/SiO_2 (black triangles) which was expected since 8V/SiO_2 has vanadium oxide nanoparticles. When the 8V/SiO_2 is mixed with SiO_2 instead of SiC the propylene selectivity increases (blue circles and red squares, Figure 3.10) by 15% at 4.3% propane conversion. This result initially suggests that the addition of IPA dehydration sites increases the selectivity to propylene through the IPA dehydration pathway on the support instead of allowing the IPA to degrade to acetone and CO_x products on vanadium sites. However, when 4V/SiO_2 was mixed with SiO_2 the selectivity did not noticeably increase, Figure 3.11. This lack of improvement in the propylene selectivity could result from the 4V/SiO_2 already having an optimum silanol density, or the improve performance of the 8V/SiO_2 may be falsely attributed to the IPA dehydration pathway on the support and instead be due to redistribution of vanadium on to the bare silica. In the case of 8V/SiO_2 even partial redistribution of the vanadium sites onto the added silica would decrease the fraction of nanoparticles on the original support and create more selective, dispersed vanadyl sites on the silica diluent. These vanadyl sites would then explain or at least contribute to the higher selectivity seen.

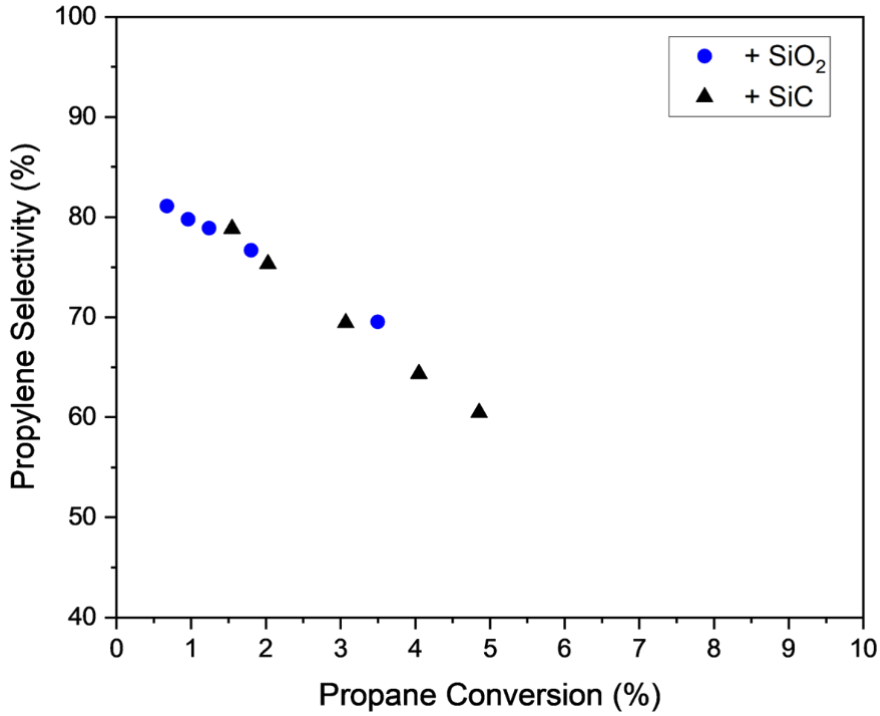

Figure 3.11 Propylene selectivity as a function of propane conversion for $4V/SiO_2$ with labeled diluents. Reactions were done at 480 °C with 30% C_3H_8, 15% O_2, and the balance of N_2 with 70-120 mg catalyst.

To investigate the redistribution hypothesis, Raman analysis of the fresh and spent mixed material was done, shown in Figure 3.12. Prior to reaction the V_2O_5 peak at 998 cm^{-1} was the dominant vanadium feature. After reaction, this feature was still the major feature seen, however, there is evidence of nanoparticle redistribution as shown by the Spent spectrum in Figure 3.12. Here the ratio between vanadyl and nanoparticle is significantly larger than that in the Fresh spectrum indicating vanadia restructuring to have a fraction of more selective vanadyl structures on the support.

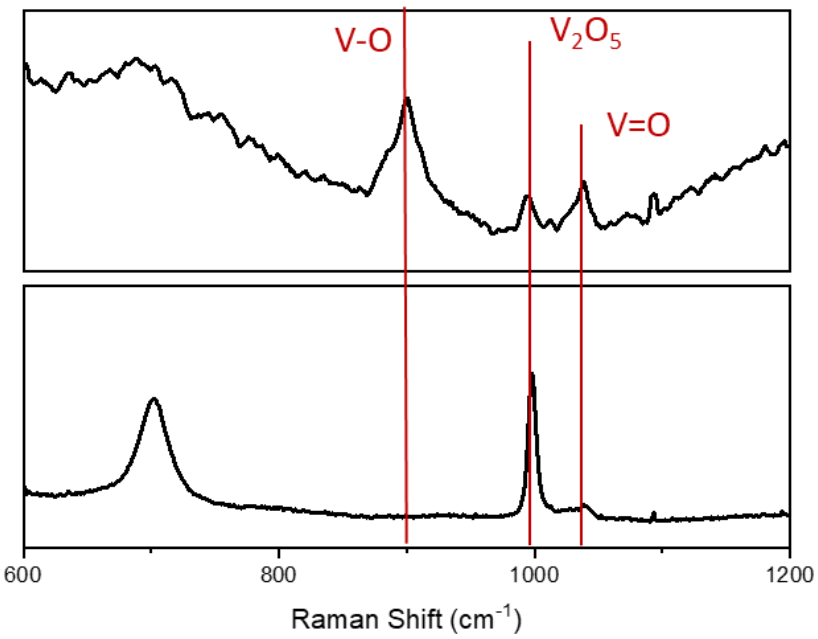

Figure 3.12 Raman Spectra of $8V/SiO_2$ mixed with a SiO_2 diluent before reaction (Fresh) and after reaction (Spent). The peaks for dispersed vanadyl (V=O), vanadium nanoparticles (V_2O_5), and V-O are labeled.

Additionally, the $8V/SiO_2$ + SiO_2 experiment was repeated but with the two materials pelletized separately prior to physical mixing. Reaction results (Figure 3.10, red squares) showed the same improvement in propylene selectivity. Then the silica pellets were separated from the $8V/SiO_2$ pellets and investigated using Raman spectroscopy to determine whether any vanadium species had migrated to the bare support and what the structure was. Figure 3.13 showed that the neat silica support added to the catalyst bed did have dispersed vanadyl sites caused by vanadium redistribution post ODH reaction. The sharp peak at 1093 cm^{-1} is likely the vanadyl overtone. With this evident redistribution and lack of propylene selectivity difference in the $4V/SiO_2$ dilution experiment, the IPA dehydration pathway and the influence of support acidity cannot be directly evidenced by this experiment. Investigation of the IPA pathway and function is still under investigation via more detailed spectroscopic and kinetic studies. Chapter 4 will address further evidence for the IPA pathway.

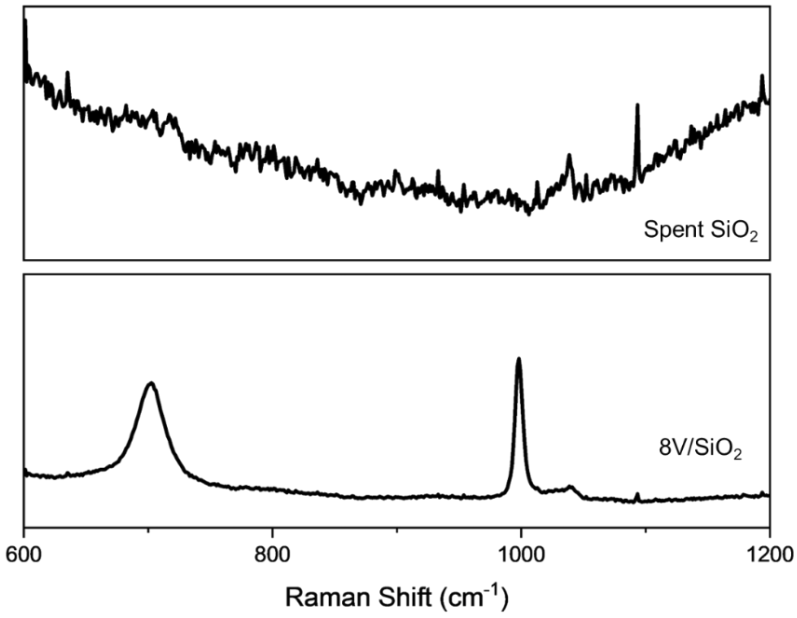

Figure 3.13 Raman spectra showing a vanadyl peak (1038 cm^{-1}). 8V/SiO_2 (bottom trace) was mixed with a separately pelletized SiO_2 diluent and treated under ODH reaction conditions. These SiO_2 pellets were separated from the 8V/ SiO_2 and measured (top trace).

3.6 Conclusions and outlook

In this work, monomeric and oligomeric vanadium species were successfully incorporated into a silicate zeolite framework through the tailored application of a solid-state synthesis. The carefully characterized MWW zeolite was deboronated and then silylated to enable incorporation of vanadium into the framework using $V(acac)_3$ as a precursor. Characterization via ICP-OES, FT-IR, UV-vis, and Raman verified that monomeric and oligomeric vanadyl sites were synthesized in the same zeolite support. Catalytic testing for propane ODH showed that monomeric vanadia is less selective and active for propylene formation than the oligomeric counterpart. This difference in activity suggests that silica supported vanadia benefits form the presence of oligomeric (multiple V=O groups bonded together by bridging oxygen atoms) species on the support. The source of this difference in performance was investigated via DFT and kinetic modeling using monomeric and dimeric vanadyl site models. The resulting kinetic reaction cycles and corresponding activation

barriers showed that dimeric vanadia can activate C-H bonds in propane at a lower activation energy compared to the monomeric model. At the same time, the activation energy to form the byproduct propylene oxide remains similar between the two systems. Kinetic modeling using information gained from the computational study was able to partially replicate the experimental data of the isolated and oligomeric vanadium zeolite. Additional work is needed in the model development to accurately determine the (1) y-intercept of the selectivity-conversion plot, and (2) the exact selectivity values. This can be done with incorporation of additional steps in the simplified cycle presented here and the incorporation of the support functions as an acid site provider for the dehydration step. Particularly, the fate of a likely short-lived IPA molecule is a promising study focus that would not only inform the mechanism but also lead to future development of better propane ODH catalysts.

Here dilution experiments concluded that vanadium redistribution onto a bare silica diluent result in improving the selectivity of a supported vanadium catalyst that has V_2O_5 nanoparticles. This improvement in propane selectivity for supported V_2O_5 was not seen for the same diluent used with oligomeric V/SiO_2. Increasing the acidity of the catalyst bed via a physical addition of silanol sites to improve IPA selectivity to propylene cannot be completely ruled out by this experiment. Redistribution may only play a partial role in the increased selectivity of silica supported V_2O_5, and the oligomeric V/SiO_2 may not see an improvement due to already being at an optimal silanol density and distribution. Going forward, kinetic experiments involving the co-feed of IPA in ODH would inform the pathway of IPA over vanadia materials. Modulation excitation spectroscopy utilizing diffuse reflectance infrared Fourier transform spectroscopy (DRIFTS) and mass spectrometry (MS) could better capture the formation and consumption of IPA and its products during reaction to determine its existence and role in the kinetic cycle.

Additionally, dilution experiments similar to that done with SiC and SiO_2 can be done with materials known as better IPA dehydration catalyst to further improve the catalytic performance of V/SiO_2 and design improved catalysts.

References

1. Rightor, E. G. & Tway, C. L. Global energy & emissions reduction potential of chemical process improvements. *Catal Today* **258**, 226–229 (2015).

2. Dong, S., Altvater, N. R., Mark, L. O. & Hermans, I. Assessment and comparison of ordered & non-ordered supported metal oxide catalysts for upgrading propane to propylene. *Appl Catal A Gen* **617**, 118121 (2021).

3. Sattler, J. J. H. B., Ruiz-Martinez, J., Santillan-Jimenez, E. & Weckhuysen, B. M. Catalytic dehydrogenation of light alkanes on metals and metal oxides. *Chem Rev* **114**, 10613–10653 (2014).

4. Weckhuysen, B. M. & Keller, D. E. Chemistry, spectroscopy and the role of supported vanadium oxides in heterogeneous catalysis. *Catal Today* **78**, 25–46 (2003).

5. Carrero, C. A., Keturakis, C. J., Orrego, A., Schomäcker, R. & Wachs, I. E. Anomalous reactivity of supported V2O5 nanoparticles for propane oxidative dehydrogenation: Influence of the vanadium oxide precursor. *Dalton Transactions* **42**, 12644–12653 (2013).

6. Keller, D. E., De Groot, F. M. F., Koningsberger, D. C. & Weckhuysen, B. M. ΛO 4 Upside Down: A New Molecular Structure for Supported VO 4 Catalysts. (2005) doi:10.1021/jp044539l.

7. Gao, X. & Wachs, I. E. Investigation of Surface Structures of Supported Vanadium Oxide Catalysts by UV−vis−NIR Diffuse Reflectance Spectroscopy. *Journal of Physical Chemistry B* **104**, 1261–1268 (2000).

8. Carrero, C. A., Schloegl, R., Wachs, I. E. & Schomaecker, R. Critical literature review of the kinetics for the oxidative dehydrogenation of propane over well-defined supported vanadium oxide catalysts. *ACS Catal* **4**, 3357–3380 (2014).

9. Grant, J. T., Carrero, C. A., Love, A. M., Verel, R. & Hermans, I. Enhanced Two-Dimensional Dispersion of Group v Metal Oxides on Silica. *ACS Catal* **5**, 5787–5793 (2015).

10. Fu, T., Wang, Y., Wernbacher, A., Schlögl, R. & Trunschke, A. Single-Site Vanadyl Species Isolated within Molybdenum Oxide Monolayers in Propane Oxidation. *ACS Catal* **9**, 4875–4886 (2019).

11. Barman, S. *et al.* Single-Site VOx Moieties Generated on Silica by Surface Organometallic Chemistry: A Way to Enhance the Catalytic Activity in the Oxidative Dehydrogenation of Propane. *ACS Catal* **6**, 5908–5921 (2016).

12. Cheng, M. J., Chenoweth, K., Oxgaard, J., Van Duin, A. & Goddard, W. A. Single-site vanadyl activation, functionalization, and reoxidation reaction mechanism for propane oxidative dehydrogenation on the cubic v 4O10 cluster. *Journal of Physical Chemistry C* **111**, 5115–5127 (2007).

13. Bulánek, R. *et al.* Effect of preparation method on nature and distribution of vanadium species in vanadium-based hexagonal mesoporous silica catalysts: Impact on catalytic behavior in propane ODH. *Appl Catal A Gen* **415–416**, 29–39 (2012).

14. Hidalgo-Carrillo, J. *et al.* Comparative Study of Vanadium Supported on MCM-36 and MCM-22 and Their Catalytic Perfomance in C $_3$ -ODH. *Ind Eng Chem Res* **54**, 2030–2039 (2015).

15. Liu, Y. M., Xie, S. H., Cao, Y., He, H. Y. & Fan, K. N. Synthesis of novel cage-like mesoporous vanadosilicate and its efficient performance for oxidation dehydrogenation of propane. *Journal of Physical Chemistry C* **114**, 5941–5946 (2010).

16. Liu, Y. M. *et al.* Vanadium oxide supported on mesoporous SBA-15 as highly selective catalysts in the oxidative dehydrogenation of propane. *J Catal* **224**, 417–428 (2004).

17. LIU, Y. *et al.* Structure and catalytic properties of vanadium oxide supported on mesocellulous silica foams (MCF) for the oxidative dehydrogenation of propane to propylene. *J Catal* **239**, 125–136 (2006).

18. Liu, Q. *et al.* Design, synthesis and catalytic performance of vanadium-incorporated mesoporous silica KIT-6 catalysts for the oxidative dehydrogenation of propane to propylene. *Catal Sci Technol* **6**, 5927–5941 (2016).

19. Guo, X.-P., Wang, X.-X., Lu, H.-Q. & Liu, Z.-M. Mesoporous sol-gel silica supported vanadium oxide as effective catalysts in oxidative dehydrogenation of propane to propylene. (2023) doi:10.1039/d3ra04024k.

20. Rozanska, X., Fortrie, R. & Sauer, J. Oxidative Dehydrogenation of Propane by Monomeric Vanadium Oxide Sites on Silica Support. *The Journal of Physical Chemistry C* **111**, 6041–6050 (2007).

21. Varzaneh, A. Z., Moghaddam, M. S. & Darian, J. T. Oxidative dehydrogenation of propane over vanadium catalyst supported on nano-HZSM-5. *Petroleum Chemistry* **58**, 13–21 (2018).

22. Rozanska, X., Fortrie, R. & Sauer, J. Size-Dependent Catalytic Activity of Supported Vanadium Oxide Species: Oxidative Dehydrogenation of Propane. *J Am Chem Soc* **136**, 7751–7761 (2014).

23. Rozanska, X., Kondratenko, E. V & Sauer, J. Oxidative dehydrogenation of propane: Differences between N 2 O and O 2 in the reoxidation of reduced vanadia sites and consequences for selectivity. *J Catal* **256**, 84–94 (2008).

24. Goodrow, A. & Bell, A. T. A theoretical investigation of the selective oxidation of methanol to formaldehyde on isolated vanadate species supported on Silica. *Journal of Physical Chemistry C* **111**, 14753–14761 (2007).

25. Haija, M. A. *et al.* Low temperature adsorption of oxygen on reduced V2O3(0 0 0 1) surfaces. *Surf Sci* **600**, 1497–1503 (2006).

26. Molinari, J. E. & Wachs, I. E. Presence of surface vanadium peroxo-oxo umbrella structures in supported vanadium oxide catalysts: Fact or fiction? *J Am Chem Soc* **132**, 12559–12561 (2010).

27. Altvater, N. R. *et al.* B-MWW Zeolite: The Case Against Single-Site Catalysis. *Angewandte Chemie - International Edition* **59**, 6546–6550 (2020).

28. Ren, L. *et al.* Pillared Sn-MWW Prepared by a Solid-State-Exchange Method and its Use as a Lewis Acid Catalyst. *ChemCatChem* **8**, 1274–1278 (2016).

29. Peeters, E. *et al.* Highly Dispersed Sn-beta Zeolites as Active Catalysts for Baeyer− Villiger Oxidation: The Role of Mobile, In Situ Sn(II)O Species in Solid-State Stannation. (2021) doi:10.1021/acscatal.1c00435.

30. Hammond, C., Conrad, S. & Hermans, I. Simple and Scalable Preparation of Highly Active Lewis Acidic Sn-β. *Angewandte Chemie International Edition* **51**, 11736–11739 (2012).

31. Wolf, P., Hammond, C., Conrad, S. & Hermans, I. Post-synthetic preparation of Sn-, Ti- and Zr-beta: A facile route to water tolerant, highly active Lewis acidic zeolites. *Dalton Transactions* **43**, 4514–4519 (2014).

32. Grant, J. T. *et al.* Improved Supported Metal Oxides for the Oxidative Dehydrogenation of Propane. *Top Catal* **59**, 1545–1553 (2016).

33. Weigend, F. Accurate Coulomb-fitting basis sets for H to Rn. *Physical Chemistry Chemical Physics* **8**, 1057–1065 (2006).

34. Weigend, F. & Ahlrichs, R. Balanced basis sets of split valence, triple zeta valence and quadruple zeta valence quality for H to Rn: Design and assessment of accuracy. *Physical Chemistry Chemical Physics* **7**, 3297–3305 (2005).

35. Becke, A. D. Density-functional thermochemistry. III. The role of exact exchange. *J Chem Phys* **98**, 5648–5652 (1993).

36. Frisch, M. J. *et al.* Gaussian 16, Revision C.01. Preprint at (2016).

37. Grimme, S., Antony, J., Ehrlich, S. & Krieg, H. A consistent and accurate ab initio parametrization of density functional dispersion correction (DFT-D) for the 94 elements H-Pu. *Journal of Chemical Physics* **132**, 154104 (2010).

38. Dzwigaj, S. *et al.* Incorporation of vanadium species in a dealuminated β zeolite. *Chemical Communications* **11**, 87–88 (1998).

39. Albuquerque, A., Pastore, H. O. & Marchese, L. Vanadium-modified MCM-22 zeolite. in *Studies in Surface Science and Catalysis* vol. 158 A 901–908 (2005).

40. Dorn, R. W. *et al.* Structure Determination of Boron-Based Oxidative Dehydrogenation Heterogeneous Catalysts With Ultrahigh Field 35.2 T 11 B Solid-State NMR Spectroscopy. *ACS Catal* **10**, 13852–13866 (2020).

41. Shvets, P., Dikaya, O., Maksimova, K. & Goikhman, A. A review of Raman spectroscopy of vanadium oxides. *Journal of Raman Spectroscopy* **50**, 1226–1244 (2019).

Chapter 4: Ternary supported vanadia materials for the improved oxidative dehydrogenation of propane

This chapter will be submitted with the title “Investigating the Synergy between Vanadium Oxide and Tantalum Oxide in Ternary Metal Oxide System for Oxidative Dehydrogenation of Propane”. I collected the kinetic data and contributed to the experimental direction and data interpretation.

4.1 Introduction

The oxidative dehydrogenation (ODH) of propane over supported metal oxides generally follows a Mars-Van Krevelen mechanism where the surface oxygen acts as the oxidant.[1] Vanadium oxide (vanadia) is one of the most studied ODH catalysts. Redox-active vanadia is typically supported on an inert material such as silica (V/SiO_2) as vanadia can change oxidation state from +3 to +5 readily. It is widely accepted that vanadyl (V=O) V^{+5} is responsible for the first C–H activation in the propane ODH kinetic cycle.[2–4] The methylene group hydrogen atom is abstracted from propane by a terminal V=O to form a V^{+4} radical and a propyl radical. Despite extensive studies on vanadium catalyzed ODH, there is ongoing debate on how the second hydrogen abstraction occurs. There are two model mechanisms for this abstraction being (1) a single vanadyl site and (2) two vanadyl sites connected through a V–O–V bond. If a mechanism modeled with only one vanadium site is considered, the second hydrogen abstraction happens on the reduced V^{+4} site to then form V^{+3} and propylene. If the second mechanism with dual vanadyl sites is considered, the two vanadia sites participate in the consecutive hydrogen abstraction steps which is more energetically favorable, as discussed in the previous chapter, Chapter 3. In this dual site case, after the first vanadyl performs a hydrogen abstraction, the second hydrogen abstraction takes place

over the same vanadyl accompanied by removal of water to create vanadium pairs of +3 and +5. As shown in Chapter 3 this pathway has a lower barrier with the removal of water of water.[2]

Once formed, propylene itself can be oxidized by surface oxygen, which lowers the selectivity during the ODH of propane. Propylene oxidation has been studied by computational methods primarily. This reaction forms an oxygenated propylene species such as propylene oxide, acetone, and acrolein.[5] The oxygenated compounds will then be further oxidized into CO and CO_2 products (CO_x). Previous studies are not conclusive on which surface oxygen is responsible for propylene overoxidation to combustion. The previous Chapter 3 argued that peroxo-vanadium is more reactive toward propylene compared to other vanadium species such as V=O, V–O–V, and V–O–Si. This finding suggests that limiting the formation of peroxo-vanadium species could lead to a more selective vanadia-based catalyst. However, Goddard suggested that peroxo-vanadium is multifunctional since this surface species can be used to regenerate adjacent reduced vanadia[6]. The surface peroxo species is generated via the barrierless oxidation of V^{+3} by gas phase oxygen.[7] Multiple studies have described the importance of surface oxygen mobility, as it has been observed to influence the selectivity and activity of vanadia catalysts.[6,8,9]

Surface oxygen mobility can be modified by the incorporation of an additional metal oxide.[10,11] Metal oxides as additives can influence the redox activity, acidity, and local coordination of a catalyst surface which can all be used to explain an improvement in the catalytic performance of vanadium sites. One hypothesis credits the type of surface oxygen with dictating the reaction selectivity.[8] This theory is supported by the interplay of the above stated factors all influencing the surface oxygen's characteristics. The structural identity of the surface oxygen remains inconclusive due to the lack of spectroscopic information on the oxygen species responsible for hydrogen abstraction. Previously, Chapter 3 showed that oxygen for peroxo-vanadium can lead to

overoxidation of propylene due to the strained three-membered ring and the low propylene activation energy to propylene oxide. In this work, the combination of spectroscopic characterization, kinetic studies, and computational results will show that vanadia can reoxidize to active vanadyl or peroxo-vanadia depending on the availability of a nearby oxygen donor. In particular, these donors will be a secondary metal oxide added to the vanadia catalyst to improve propane ODH performance. The secondary metal oxides studied here are TaO_x and NbO_x, both of which will be found to have similar promotional effects.

Tantalum oxide is one oxide that increases both the selectivity of propylene and the activity of supported vanadium oxide catalysts. In the following study, vanadia catalysts synthesized with different loadings of TaO_x were investigated through kinetic and spectroscopic methods including ^{51}V solid-state nuclear magnetic resonance (SSNMR), X-ray photoelectron spectroscopy (XPS), electron paramagnetic resonance (EPR), Raman spectroscopy, X-ray adsorption spectroscopy (XAS), and in-situ diffuse reflectance infrared Fourier transform spectroscopy coupled with mass spectrometry (DRIFTS-MS). Either neat Ta_2O_5 or Ta_2O_5 supported on silica was treated under propane ODH conditions and exhibited poor performance with less than 40% propylene selectivity at 1% propane conversion (comparable to background conversion). On the other hand, TaO_x on a ternary $VO_x/TaO_x/SiO_2$ catalyst exhibited the improved selectivity to propylene of 85% at 3.2% propane conversion when compared to V/SiO_2 (75% propylene selectivity at 3% propane conversion). This reactivity results suggest that while Ta_2O_5 is not the primary active site for propane ODH, it acts as an additive to promote vanadia performance. XPS showed that the V^{+4} increased with increasing Ta_2O_5 loading which could influence the catalytic turnover rate. XAS and ^{51}V SS-NMR showed complex surface structures consisting of VO_x and TaO_x species with some degree of coordination. In addition to the experimental components, a computational DFT

study suggested that oxygen vacancies generated by the secondary metal oxide facilitated oxygen transfer and prevented the formation of unselective peroxo-vanadium species. This computationally driven hypothesis was then supported by oxygen shutoff experiments using operando DRIFTS-MS. While the majority of characterization and mechanistic development focused on the influence of Ta_2O_5 on vanadia, NbO_x was also found to similarly promote the activity and selectivity of vanadia catalysts through preventing the overoxidation of propylene.

4.2 Methods

4.2.1 Material Synthesis

The supported vanadium oxide, tantalum oxide, and niobium oxide catalysts were synthesized using incipient wetness impregnation (IWI).[12] Synthesizes were carried out in a purge box with an inert N_2 atmosphere. To prevent loss of material through static, silica (Aerosil 200, Evonik) was treated with 18 MΩ water then dried in an oven at 120 °C before being ground to a powder. The dried powder was used for the following materials using an incipient wetness point of 1.4 mL/g. A solution of tantalum ethoxide (Sigma Aldrich, 99.8% purity) in dry ethanol (Sigma Aldrich, 99.8% purity) was used for addition of TaO_x. A solution of vanadium oxytriisopropoxide (Alfa Aesar, 96% purity) in dry isopropanol (Sigma Aldrich, 99.5% purity) was used for addition of VO_x. A solution of niobium ethoxide (Sigma Aldrich, 99.88% purity) in dry ethanol (Sigma Aldrich, 99.8% purity) was used for addition of NbO_x. After impregnation of each metal precursor the material was transferred to a muffle furnace where it was calcined under dry air by first holding at 120 °C for 3 hr, ramping to 550 °C at 1 °C/min, and holding at 550 °C for 3 hr. After addition of either tantalum or niobium and calcination, the vanadium was added, and the material was calcined again. The resulting catalysts were named as xV/SiO_2, $xV/yTa/SiO_2$, $xV/zNb/SiO_2$ where

x, y, and x are the weight percent loadings for vanadium, tantalum, and niobium, respectively, as determined by bulk elemental analysis.

4.2.2 Material characterization

Bulk elemental analysis was done by **inductively coupled plasma – optical emission spectroscopy** (ICP-OES) to determine the vanadium, tantalum, and niobium loading. Samples were weighed out in 15-20 mg per analyte, and three replicates were measured for each sample. Samples were completely digested in 48% HF before being diluted with 18 MΩ H_2O. Analysis was done on an ICP-OES with all borosilicate components replaced with Teflon equivalents to avoid etching of the glass by the HF. Three wavelengths were averaged for each element measured and the three replicates were used to determine the measurement error. Specific surface area was determined using the multipoint **Brunauer-Emmett-Teller** (BET) method. Nitrogen physisorption measurements were done at 77 K using a Micromeritics 3-Flex instrument.

Raman measurements were done with Renishaw InVia Raman spectrometer with a 785 nm excitation laser equipped with a 1200 L mm^{-1} grating. Spectra were taken at a range of 250-1200 cm^{-1} and a dispersion of 1.36565 cm^{-1} $pixel^{-1}$. All samples were measured at ambient temperature and atmosphere unless otherwise noted.

X-ray photoelectron spectroscopy (XPS) measurements were taken via Thermo Scientific XPS using a micro-focused monochromated Al K-alpha X-ray source with a flood gun to reduce surface charging of vanadium-containing samples. Samples were measured at room temperature under ultra-high vacuum 10^{-7} mbar. C 1s, O 1s, and V 2p regions were scanned using a 50 eV pass energy, a 50 ms dwell time, a 400 μm spot size, and a 0.2 eV energy step size. The average number of scans per element were adjusted to improve the signal-to-noise. All surface

compositions, and peak integrations and deconvolution were done via the Avantage (Thermo Scientific) software package. All peaks, including the V 2p region were referenced to the adventitious carbon peak at 284.8 eV. It is important to note that referencing V 2p peaks to adventitious carbon can result in slightly higher binding energy shifts. The entire O 1s and V 2p regions were used to fit the V2p peaks. All peaks were fitted with a Shirley background. Fitted peaks were constrained such that the peak height of the 2p1/2 peak is 0.516 times the value of the 2p3/2, a 30% Lorentz-Gaussian convolve mix, and Powell fitting algorithm to achieve FWHM values of approximately 2.1 eV or below and minimize residual values between the computational envelope and empirical data. **X-ray adsorption spectroscopy** (XAS) was measured for X-ray adsorption near edge spectroscopy (XANES) at the Advanced Photon Source – Argonne National Laboratory at Beamline 20 BM. The energy resolution was 1.4 x 10^{-4} eV, and the range of the beamline was 2.1-22.5 keV. The V/Ta/SiO_2 and V/SiO_2 catalysts and reference samples and foils (V_2O_5, V_2O_4, $VO(OAc)_2$, Na_3VO_4 and Ta_2O_5) were pressed into self-supporting wafers inside an inert atmosphere. The wafers were then sealed into a sample holder with Kapton windows. The beam energy and detector were calibrated to the V K edge and Ta L_3 edge using pure foils. Spectra of the silica-supported materials were measured in florescence mode while the spectra of pure materials were measured in transmission mode. Each sample was measured for 1 hr at 3 scans (20 min/scan). Oxidation states were quantified by fitting the XANES spectra using the standards.

4.2.3 Catalytic testing and activation energy measurement

Kinetic measurements were done on a Microactive-Effi reactor in a plug flow configuration. A total of 75-100 mg of catalyst was mixed with an inert diluent of passivated SiC in a mass ratio of 1:2 (catalyst/SiC). The catalyst and SiC were pelletized to 425-600 μm. The material was packed in a quartz reactor tube with an inner diameter of 9 mm. The catalyst bed was

supported on quartz wool and, the void space was packed with quartz chips of the same 425-600 μm particle size. The reaction was carried out at 480-500 °C with gas flowrates of 3:6:11 $O_2/C_3H_8/N_2$ where all gases are ultra-high purity (UHP) grade. A thermocouple that was in contact with the catalyst bed was used to monitor the temperature during reaction. The total volumetric flowrate of gas was varied 20-120 sccm to vary the contact time. The effluent gas from the reactor was analyzed with an online Shimadzu 2010 GC equipped with a thermal conductivity detector (TCD) and flame ionization detector (FID). The carbon balance was closed within ±2%.

To measure propane and propylene activation energy barriers, the catalysts were first heated to 500 °C under 20 sccm with 80% N_2 and 20% O_2. After heating the samples were pretreated under ODH conditions (30% C_3H_8, 15% O_2, 55% N_2) until propane conversion stabilized (8-16 hr). Activation energy experiments for propane were done over a temperature range of 440-480 °C. The reaction started at the highest temperature and data was collected at decreasing temperature setpoints (40-120 mL/min flowrates at each temperature). The activation energy for propylene was measured in the range of 320-380 °C as propylene is more reactive than propane. The rates at each temperature were first measured from high to low temperatures then again from low to high temperatures to avoid error from hysteresis. All reactions took place at ambient pressure, and reactant conversion was kept below 10% at all temperatures.

Reaction rates were computed using product conversion for propane and reactant conversion for propylene. Propane consumption and propylene consumption rates were computed by taking the slope of the contact time versus conversion plot. Propylene production rate was computed by taking the slope of the contact time versus propylene yield plot. Apparent activation energies were computed by taking the slope of the Arrhenius plot. Error bars were generated by randomly sampling the reaction rates from normal distributions centered around the reaction rate

values with standard errors generated from their respective linear regressions. The +/- designator represents two standard deviations in the final Arrhenius slope computed from 100,000 random samples. The propagation of error was also utilized throughout all numeric manipulations.

4.2.4 Oxygen spillover experiments

Oxygen spillover experiments were performed in a homebuilt setup utilizing a Pike DiffusIR chamber as a reactor. The outlet of the reactor was monitored by an Extrel MAX300-CAT mass spectrometer (MS). Each sample was loaded in 15 mg batches and was heated to 500 °C with a ramp rate of 20 °C/min and a hold time of at least 2 hours under 5 sccm of 30% O_2 in Ar (UHP, Airgas). The samples were then cooled to 490 °C and the inlet containing 30% O_2, 30% propane, and 40% Ar was fed to the reactor for at least 1 hour until a steady state was established. Flowrates were varied between the different samples to achieve 5-6% propane conversion. Afterwards, the O_2 feed was switched to N_2 at the same flowrate. Propane conversion and water formation were monitored by measuring m/z = 43 and 18, respectively, in the MS, utilizing the signal of Ar at m/z = 20 as an internal standard.

4.3 Results and discussion

4.3.1 Synthesis and synergy

When considering the synergy between vanadium and tantalum on a silica support, the loading of tantalum is important. In this study the loading of vanadium on silica was maintained at nominal 4 wt.% which is the loading of vanadium on silica near monolayer coverage.[12] As the loading of Ta is increased in the ternary material, the promotional effect can be seen starting at 10 wt.% tantalum, which is near the monolayer loading of tantalum oxide on bare silica, Figure 4.1. The improvement in selectivity is possibly due to the close proximity interaction between vanadia

and TaO_x. To test whether the promotional effect was caused by the sum of selectivity between supported vanadia and supported TaO_x, $18Ta/SiO_2$ was synthesized and tested. Figure 3.1 shows that $18Ta/SiO_2$ was significantly less selective than $4V/SiO_2$ with 40% selectivity to propylene at 1% propane conversion. This poor propane selectivity at low conversion is not seen in the ternary $4V/18Ta/SiO_2$ material when vanadium is deposited on Ta/SiO_2. If the supported vanadia and supported TaO_x were indeed catalyzing propane individually, an intermediate selectivity to propylene would be observed. Instead, there is a promotional effect, and the slope of the selectivity-conversion trend matches that of $4V/SiO_2$ instead of Ta/SiO_2. The vanadia likely bonds with the TaO_x modifying the catalytic activity of both to improve their performance likely via modifying the structure and reaction mechanism of vanadia.

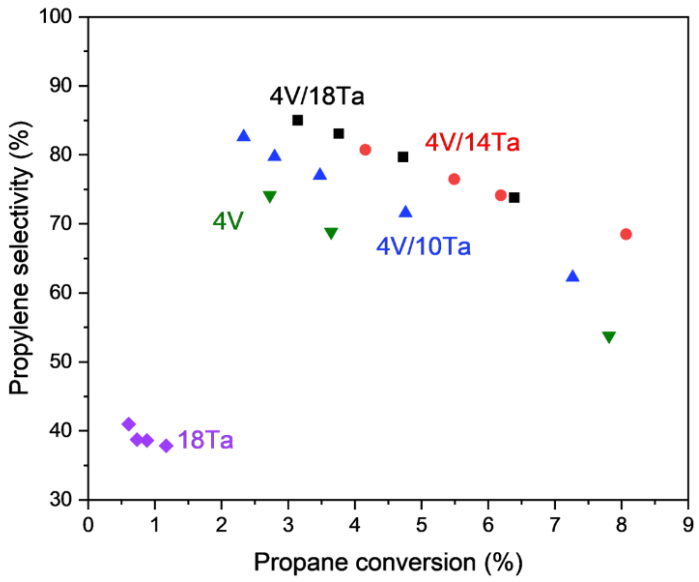

Figure 4.1 Propylene selectivity as a function of propane conversion of labeled V/SiO_2 and $V/Ta/SiO_2$. The reaction was run at 500 °C with 50-100 mg of catalyst and a gas inlet mixture of 30% C_3H_8, 15% O_2, and the balance of N_2.

To further investigate the influence of synthesis on synergy and active site(s) formation, the following materials with vanadium on different supports were synthesized and tested along with mixed catalyst beds for propane ODH. When considering the synthesis of $4V/18Ta/SiO_2$, vanadium is added to the calcined Ta/SiO_2, so one possible active site configuration is vanadium sites bonded to the TaO_x layer. To test whether vanadia on TaO_x is the active site configuration, $0.4V/Ta_2O_5$ and $4V/Ta_2O_5$ were synthesized via IWI. These materials each have dispersed vanadyl and nanoparticles of vanadium respectively. Figure 4.2 shows the low propylene selectivity of both materials relative to the ternary catalyst, indicating that neither configuration of vanadium on TaO_x is the major active species in the $V/Ta/SiO_2$ catalysts. Additionally, a catalyst bed with a physical mixture of $4V/SiO_2$ and $18Ta/SiO_2$ was tested and did not achieve the same propylene selectivity as the ternary catalyst. This result suggests that the active site(s) need to be either at a closer proximity on the same support surface or partially bonded through bridging oxygen for the promotion effect. The influence of site proximity also supports the surface Mars-Van Krevelen mechanism. The above synthesis and mixed bed experiments pointed toward TaO_x changing either the vanadium stie structure or changing the surface mechanism and not a combinatory effect between the two individually supported metal oxides.

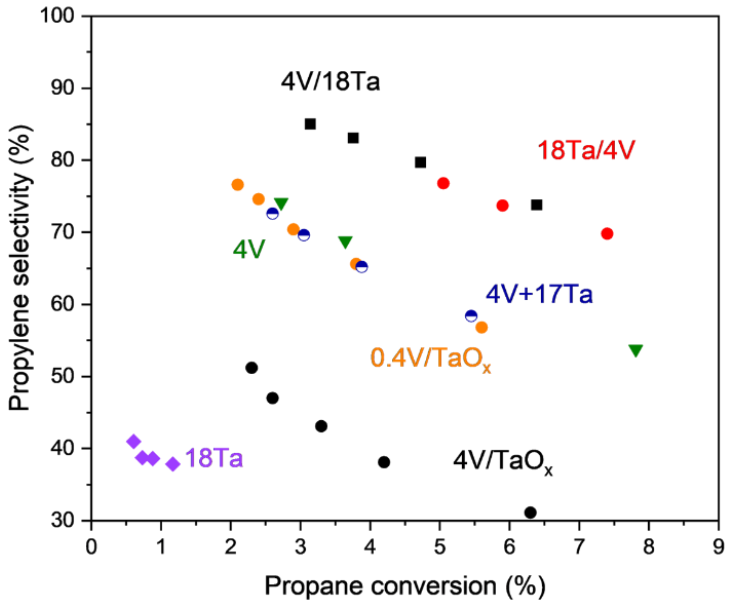

Figure 4.2 Propylene selectivity as a function of propane conversion of labeled V/SiO_2, $V/Ta/SiO_2$, and V/TaO_x. The reaction was run at 500 °C with 50-100 mg of catalyst and a gas inlet mixture of 30% C_3H_8, 15% O_2, and the balance of N_2.

The order of synthesis for $4V/18Ta/SiO_2$ also does not influence the selectivity of propylene. When $18Ta/4V/SiO_2$ was synthesized by first adding vanadium then tantalum to silica, the catalytic performance was the same as that of the original ternary catalyst. This result suggested that vanadium and tantalum likely exist in a co-monolayer of each metal oxide on the silica surface, meaning each metal oxide is bonded to the silica surface with limited interaction with each other instead of the metal oxides creating a mixed metal oxide. The degree of dispersion between the two metal oxides differed due to the calcination temperature. The Tamman temperature of vanadia is 400 °C while that of TaO_x is 900 °C, and the calcination temperature after each impregnation step is 550 °C. Therefore, the vanadia was well dispersed and will come to the same thermodynamically stable state regardless of the order of impregnation in synthesis.[13,14] Tantalum oxide, on the other hand, likely formed small nanoparticles on the catalyst surface as the

calcination temperature does not reach its Tamman temperature. Tantalum may act as promoter for vanadium sites to increase their selectivity and not participate in the ODH mechanism directly.

In addition to varying the vanadium support a series of dilution experiments using a physical mixture of the two metal oxides were done to elucidate the root of the synergy. The tantalum may act as a dehydration catalyst to modify the isopropanol (IPA) pathway (introduced in Chapter 3) and reduce formation of CO_x products. The IPA formed over the vanadyl sites could dehydrate to propylene over tantalum acid sites instead of combusting over vanadia redox sites. Or the tantalum may have modified the electronic structure of the vanadium sites through forming a co-layer on the support. The V/Ta_2O_5 materials showed that vanadium supported on tantalum is not the promoted active site because V/Ta_2O_5 catalysts are not as selective as $4V/18Ta/SiO_2$. Figure 4.3 (a) showed the physical mixture of powdered $4V/SiO_2$ and Ta_2O_5 does improve the propylene selectivity compared to $4V/SiO_2$, however it did not reach the same selectivity as the ternary material made by IWI. Interestingly the selectivity of the physical mixture in Figure 4.3 (a) was higher than that of the physical mixture in Figure 4.2. This difference may have been due to the proximity of the mixed materials. In Figure 4.2 the two catalysts were first pelletized individually then mixed, and in Figure 4.3 the two were mixed as powders then pelletized. If the role of the second metal oxide was to influence the surface mechanism by promoting dehydration of IPA to prevent overoxidation the proximity of the vanadium and tantalum sites could be important, especially if the lifetime of the IPA under ODH reaction conditions was short. The physical mixture in Figure 4.3 (a) still did not reach the propylene selectivity of the ternary one. This difference is likely due to an additional effect that tantalum has on the electronic structure of vanadium from being bonded to or nearby. The combination of these two promotional effects must be investigated

further. Figure 4.3 (b) showed that this promotional effect was not exclusive to tantalum but was observed for niobium as well. This chapter will continue to focus on tantalum.

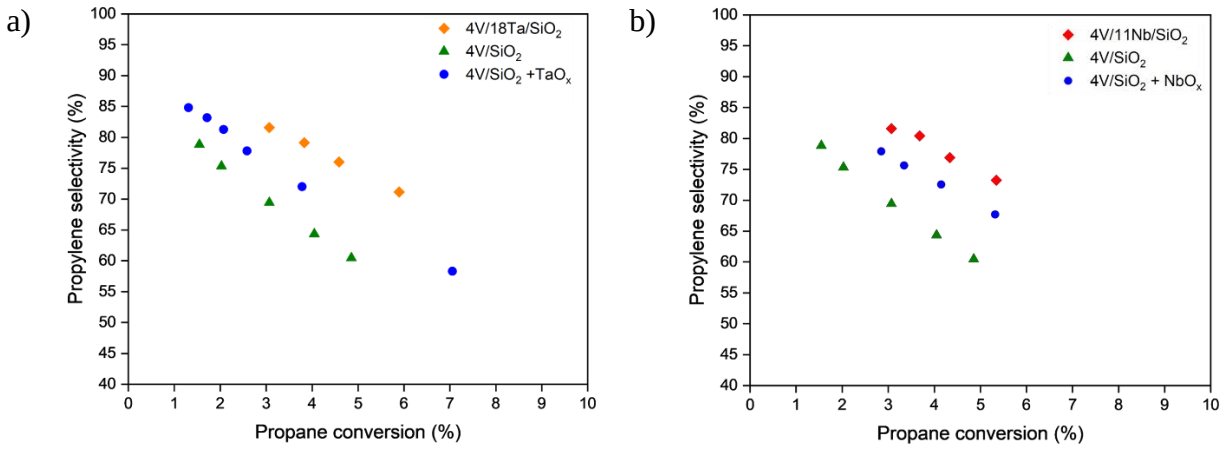

Figure 4.3 Propylene selectivity as a function of propane conversion of labeled $4V/SiO_2$, $4V/18Ta/SiO_2$, $4V/11Nb/SiO_2$, and physical mixtures of $4V/SiO_2$ + Ta_2O_5 and $4V/SiO_2$ + Nb_2O_5. The reaction was run at 480 °C with 50-120 mg of catalyst and a gas inlet mixture of 30% C_3H_8, 15% O_2, and the balance of N_2.

4.3.2 Material Characterization

Silica supported vanadium can form either dispersed vanadyl sites or agglomerated V_2O_5 nanoparticles. As discussed in Chapter 3, the dispersed vanadyl sites are more selective for propane ODH while the nanoparticles lead to deep oxidation of the propylene. The dispersed vanadyl sites on silica have a Raman signal at 1040 cm^{-1} and V_2O_5 has a sharp signal at 998 cm^{-1}.[15] The exact position of the dispersed vanadyl peak will shift depending on the support. Figure 4.4 shows that in all V/SiO_2 and $V/Ta/SiO_2$ catalysts had the same 1040 cm^{-1} peak regardless of the tantalum loading, and no 998 cm^{-1} peak was observed. This result suggested the vanadia is in a dispersed vanadyl stie configuration with no nanoparticles. When pure Ta_2O_5 was measured in Raman, Figure 4.4, broad bands between 450-900 cm^{-1} arising from the Ta–O bonds in the crystal structure.[16] Due to the strong silica vibrations in the supported tantalum materials and the weak signal of TaO_x in the same, these Ta_2O_5 bands could not be distinctly seen. Wachs previously

reported that a ~12 wt.% loading of Ta_2O_5/SiO_2 is monolayer coverage of tantalum oxide on silica (S_{BET} = 332 m^2/g).[17] Therefore, it is reasonable to assume that the ternary $V/Ta/SiO_2$ catalysts made with $SiO_{2\text{-}(200)}$ and a tantalum loading over 12 wt.% have oligomeric TaO_x species. Additionally, a broad signal 920 cm^{-1} was observed in the ternary catalysts with 14 and 18 wt.% tantalum. This signal has been assigned to V^{+4}=O structures which are reduced vanadia with an oxygen vacancy.[18] This assignment was confirmed with XPS analysis.

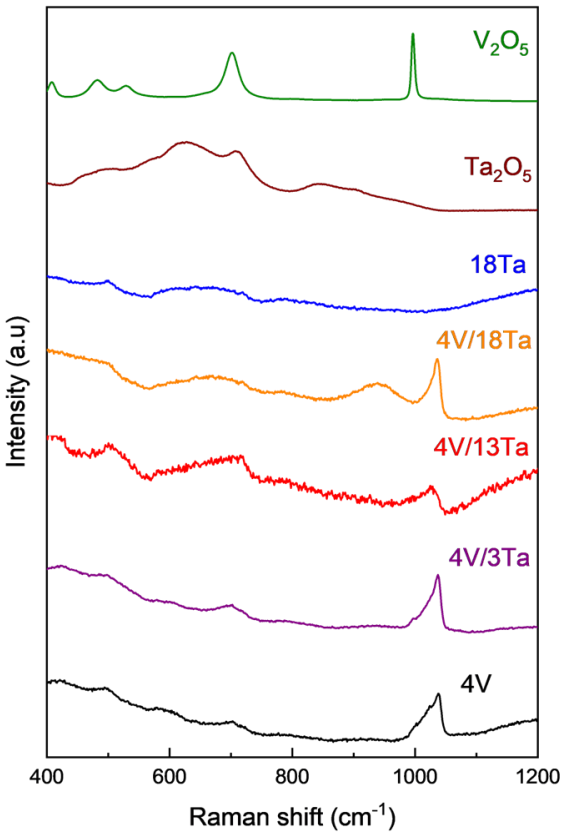

Figure 4.4 Raman spectra of silica supported vanadia, silica supported tantalum, tantalum oxide, and vanadium oxide after calcination. All samples were dehydrated at 500 °C and measured with a 785 nm laser.

To probe any changes in the V 2p electron binding energy when TaO_x was added to the vanadium catalyst, XPS was used. The XPS signal was deconvoluted into three peaks assigned to V^{+3}, V^{+4}, and V^{+5}, Figure 4.5. In the $4V/SiO_2$ material the V^{+3} and V^{+5} peaks make up the experimental trace in approximately equal ratios. When TaO_x was added to the material, the V^{+4} peak increased proportionally to the tantalum loading, and the V^{+3} and V^{+5} peaks were still observed. XPS is a surface measurement technique that measures approximately the top 5 nm of the sample. Therefore, the observations made with XPS were specific to the vanadium oxide surface. Additionally, EPR confirmed the presence of V^{+4} in $4V/SiO_2$ (weak signal intensity) and in $4V/18Ta/SiO_2$ (strong signal and hyperfine splitting), Figure C.1. These observations on V^{+4} could indicate that tantalum was facilitating the reduction of V^{+5} by stabilizing the V^{+4} structure through an electronic effect which then allowed for rapid catalytic cycling of vanadium oxidation states. The rate determining step for propane ODH is the first C–H abstraction which reduces the vanadyl from V^{+5} to V^{+4}, as discussed in the previous chapter. The reducibility of vanadium has been used as a reactivity descriptor, so the reducibility of vanadium being improved by coordination with tantalum could be the source of synergy.[8,9,19] Carrero reported that a vanadium-niobium oxide system was able to stabilize V^{+4} oligomers preferentially over isolated V^{+4}.[10] For this ternary catalyst the addition of tantalum could be similarly stabilizing V^{+4} oligomers over monomers which are the more reactive vanadia structure as explored in Chapter 3.[15]

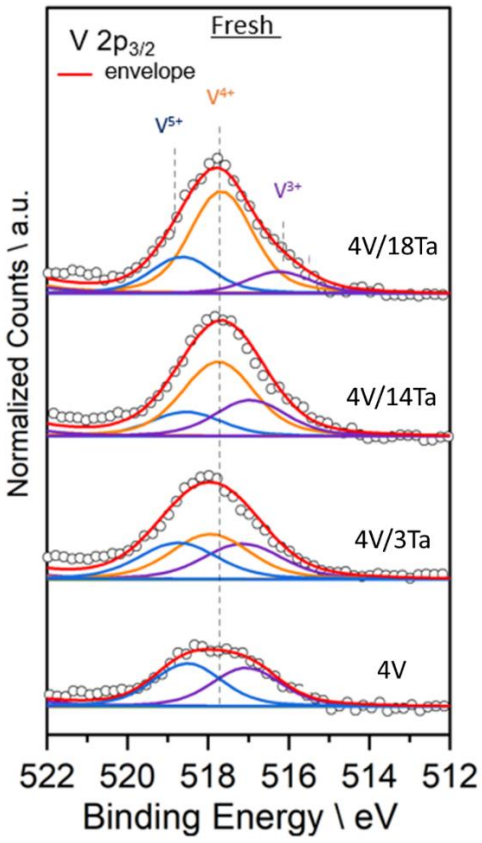

Figure 4.5 XPS spectra of vanadium and tantalum catalysts supported on silica. The red trace is the simulated spectra, and the blue, orange, and purple traces correspond to the V^{+5}, V^{+4}, and V^{+3}, respectively. The experimental spectra are shown with open circles.

Another technique used to examine the $V/Ta/SiO_2$ material was ^{51}V SSNMR. The SSNMR was in agreement with the Raman results. In $4V/SiO_2$ the major peak at -695 ppm was assigned to the dispersed vanadyl site, and the minor peak at -615 ppm represented V_2O_5 as shown in Figure 4.6.[20] In the $4V/18Ta/SiO_2$ material, the -695 peak was still present, but the major peak shifted to -660 ppm indicating a more deshielded ^{51}V nucleus. This shift could represent a larger fraction of (or longer chain) oligomerized vanadyl sites, which are more closely related to V_2O_5 at -615 ppm. Figure C.2 shows the $^{1}H\{^{51}V\}$ D-HMQC projection of $4V/SiO_2$ indicating that the ^{51}V nuclei are nearby to silanol sites. In contrast, the $^{1}H\{^{51}V\}$ D-HMQC projection of $4V/Ta/SiO_2$ showed ^{51}V still near to silanol groups. Although the Raman did not show a distinct V_2O_5 peak, the ^{51}V SSNMR

suggests that tantalum oxide is occupying the silica surface sites and driving the vanadia to aggregate to form polymeric vanadium species. This co-layer of tantalum oxide and vanadium oxide also contains more oxygen vacancies that will alter the surface oxygen availability for the reaction mechanism.

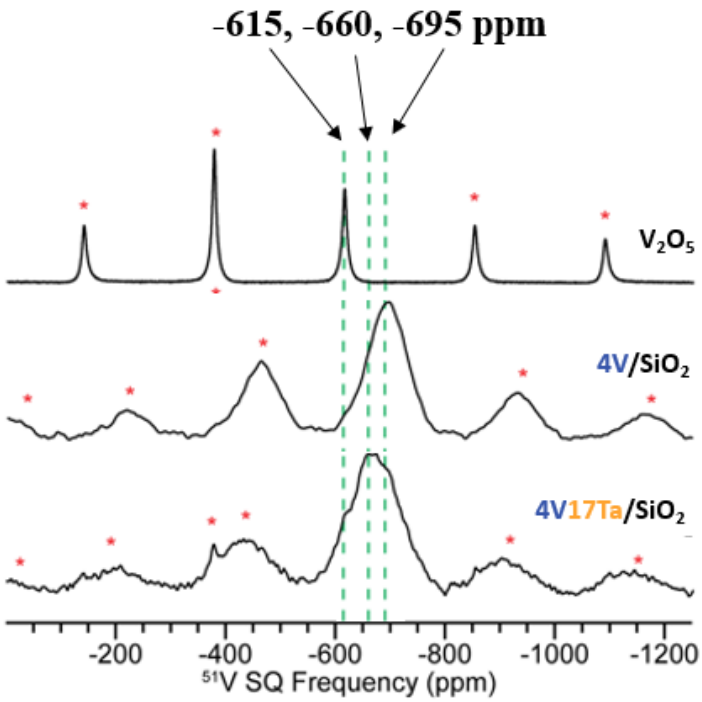

Figure 4.6 ^{51}V SSNMR spectra of $4V/SiO_2$, $4V/18Ta/SiO_2$, and V_2O_5. Vanadium materials were dehydrated at 500 °C prior to measurement. Samples were measured at 25 kHz on a 9.4 T instrument. Sidebands are marked with a red star and are not true peaks.

To derive more detail on the vanadium and tantalum structures, XAS was measured as well using X-ray adsorption near edge spectroscopy (XANES). The K-edge of vanadium represents the dipole-allowed transitions of V^{1s} electrons to V^{4p} states and is used to probe the oxidation state, local symmetry, and structure of vanadium materials.[21] In particular, the local asymmetry and oxidation state of vanadium atoms can be identified by the intensity and pre-edge feature around 5470 eV.[21,22] The height of this pre-edge peak was used to determine the local symmetry of vanadium oxide. An ideal tetrahedron would have an intensity value at 0.8 – 1.0.[23] Figure 4.7 (a) shows this value was between 0.51 and 0.65 suggesting that the surface structure of vanadium oxide resembles that of a distorted tetrahedron.[24] The pre-edge peak intensity increases with increasing loading of the tantalum oxide which suggested that the vanadia trends closer to the tetrahedron configuration. This pre-edge feature moves from 5370.8 eV to 5370.4 eV with increasing loading of tantalum oxide indicating a reduction of the vanadium center which agrees with the XPS and Raman results. Both the pre-edge position and intensity changes facilitate the Ta–O coordination interactions. The while line adsorption around 5480 eV due to the 1s → 4p transitions suggested that the formal oxidation state of vanadium was +5.[21,22]

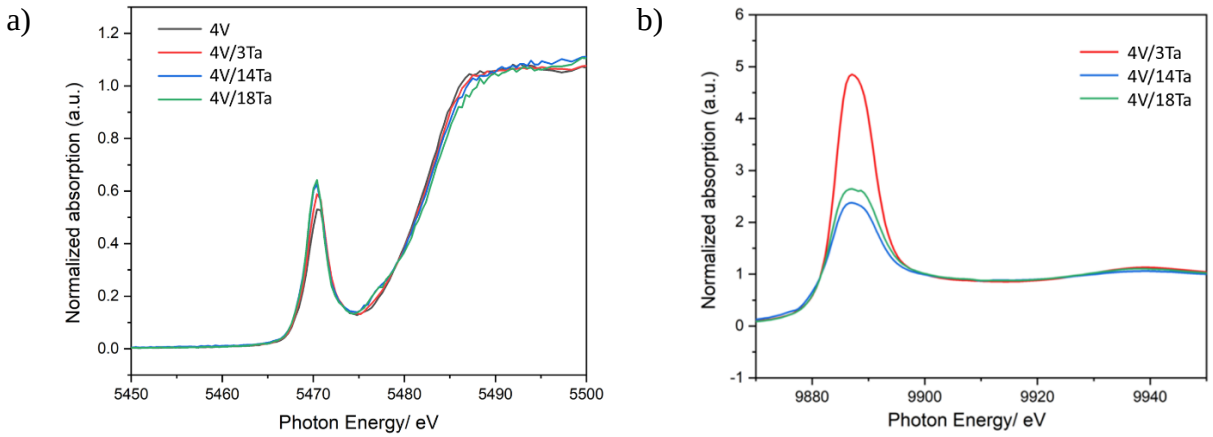

Figure 4.7 X-ray adsorption near edge spectroscopy (XANES) spectra of silica supported vanadium and tantalum catalysts at (a) the V K-edge and (b) the Ta L3 edge.

Along with the V K-edge, the Ta L3 edge was also measured with XANES, Figure 4.7 (b). The white line edge was due to the transition from the core 2p state to the unoccupied Ta 5d state. The L3 edge amplitude was directly correlated to the oxidation state of tantalum.[25] The overall oxidation state of tantalum was lower in the samples with higher tantalum loading, 4V/18Ta/SiO_2 and 4V/14Ta/SiO_2. The exact oxidation state for tantalum was not determined as the XANES results showed only a general mix of oxidation states instead of a specific state. This result suggested that more oxygen vacancies were present at higher tantalum loadings. As mentioned above, these oxygen vacancies could be responsible for greater surface oxygen availability and mobility facilitating the redox cycle.

4.3.3 Kinetic and activation energy experiments

The propane and oxygen reaction orders were determined for $4V/SiO_2$ and $4V/18Ta/SiO_2$ by measuring the propane ODH reaction rate as a function of propane and oxygen partial pressures, respectively, Figure C.3. Both catalysts were first order in propane and zero order in oxygen. This result was consistent with both catalysts following a Mars-Van Krevelen mechanism. The first order with respect to propane indicated that the rate limiting step is propane activation. The reactant orders for $4V/SiO_2$ were consistent with the literature, and it is important to note that $4V/18Ta/SiO_2$ exhibits the same reaction orders. For propane ODH catalysts, the selectivity can be inversely correlated to the difference in the apparent activation energies of propylene and propane ($E_{A2} - E_{A1}$ as shown in Reactions 1 and 2).[26] The larger the difference between these activation energies the higher the propylene selectivity should be. An ODH catalyst must discriminately dehydrogenate propane without combusting propylene.

$$C_3H_8 + 0.5\ O_2 \rightarrow C_3H_6 + H_2O \qquad \text{(Reaction 1)}$$

$$C_3H_6 + O_2 \rightarrow CO_x + H_2O \qquad \text{(Reaction 2)}$$

Next the apparent activation energies of propane and propylene were experimentally determined for $4V/SiO_2$ and $4V/18Ta/SiO_2$. These values are shown in Table 4.1 and clearly show a synergetic effect of the supported vanadium-tantalum ternary catalysts. The activation energies on $4V/SiO_2$ were in agreement with values reported in literature, E_{A1} = 130 kJ/mol and E_{A2} = 40 kJ/mol.[26] The ca. 90 kJ/mol difference in activation energy between propane and propylene results in the preferential combustion of propylene over the desired propane dehydrogenation. In stark contrast, the $4V/18Ta/SiO_2$ propane and propylene were equally likely to be activated since their barriers were similar, E_{A1} = 100 kJ/mol and E_{A2} = 114 kJ/mol. To the best of current knowledge, the ternary $V/Ta/SiO_2$ catalyst is the first supported metal oxide with $E_{A2} > E_{A1}$ for propane ODH.

The effects of similar activation energies were seen in Figure 4.8. When $E_{A1} >> E_{A2}$, the selectivity to propylene increases with increasing temperature as the propane dehydrogenation was accelerated faster than the propylene overoxidation. This scenario holds true for $4V/SiO_2$, Figure 4.8 (a). In contrast, the propylene selectivity-conversion trend was the same over a 60 °C temperature change. This observation indicated that propane and propylene activation barriers are similar confirming their kinetic measurements.

Table 4.1 Apparent propane and propylene activation energies of $4V/SiO_2$ and $4V/18Ta/SiO_2$ with corresponding errors.

	$4V/SiO_2$	**$4V18Ta/SiO_2$**
Propane activation (E_{a1}) [kJ/mol]	130 ± 9	100 ± 10
Propylene activation (E_{a2}) [kJ/mol]	40 ± 8	114 ± 11

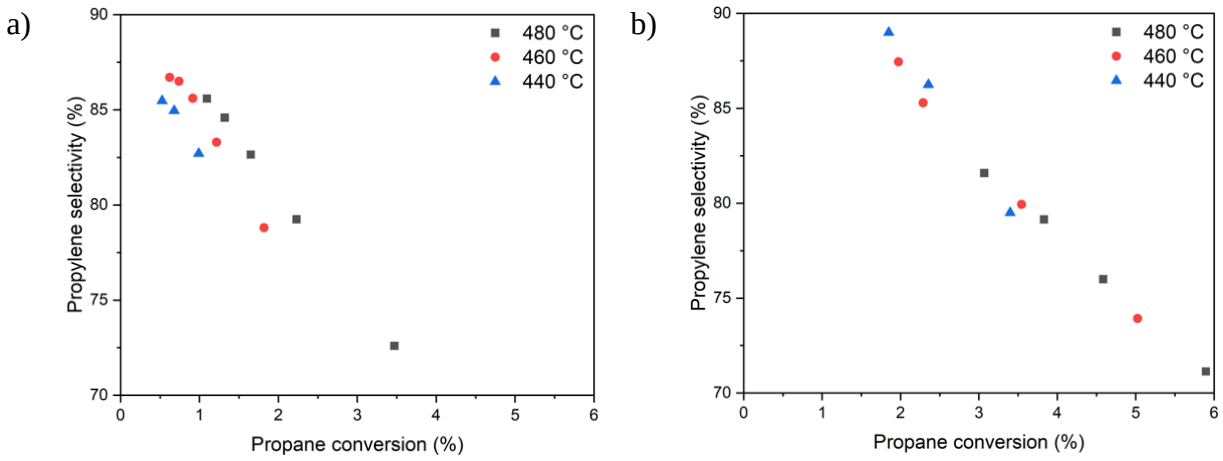

Figure 4.8 Propylene selectivity as a function of propane conversion for a) $4V/SiO_2$ and b) $4V/18Ta/SiO_2$ at the labeled reaction temperatures. 50-100 mg of catalyst was used, and the inlet gas feed was 30% C_3H_8, 15% O_2, and the balance of N_2.

4.3.4 Oxygen Spillover

The previous section determined that the propylene activation energy changes significantly with the addition of tantalum oxide to the silica supported vanadium catalysts. As shown previously in Chapter 3 the catalytic cycle can go through a peroxo-vanadium pathway that will lower the propylene selectivity. These two observations may indicate that the tantalum is lowering the concentration of peroxo- species by way of oxygen spillover. To test this theory $4V/SiO_2$ and $4V/18Ta/SiO_2$ were tested in an IR cell equipped as a reactor. Each catalyst was treated under propane ODH conditions until they reached steady state conditions at 5-6% propane conversion. Next the oxygen feed was turned off and the reaction products were monitored for the following 90 min using the MS, Figure 4.9. To maintain the same total gas flowrate over the catalyst the flowrate of oxygen that was turned off was replaced with the same volumetric flowrate of nitrogen. Figure 4.9 (a) showed that the rate of propane consumption over $4V/18Ta/SiO_2$ is above zero for ca. 20 min longer than the propane consumption of $4V/SiO_2$, indicating that $4V/18Ta/SiO_2$ was more capable of activating propane when the oxygen feed was turned off possibly due to more available oxygen on its surface. To confirm this observation and further illustrate the spillover effect more clearly, the water signal was monitored in the MS after turning off the oxygen feed, Figure 4.9 (b). The water is a product of propane ODH and in this experiment did not come from either pre-adsorbed water on the catalyst or as an impurity in the gas feed since the materials were pretreated at 500 °C and the feed gases are ultra-high purity grade. Therefore, any water observed was a result of propane oxidative dehydrogenation, which is in agreement with the propane consumption rate in Figure 4.9 (a). In Figure 4.9 (b) the oxygen signal immediately dropped to baseline, and the water was formed well after the oxygen shutoff. Notably, the $4V/18Ta/SiO_2$ maintained water production for 61 min after oxygen shutoff, while $4V/SiO_2$ produced water for only about half that time at 32 min. After the catalyst depleted the remaining gas phase oxygen for

the vanadium redox cycle, the oxygenated surface would then serve as the source of oxygen for the ODH cycle. After the surface was depleted of available oxygen the reaction cycle would then stop or switch to non-oxidative dehydrogenation (DH). DH would result in coke formation and a completely different mechanism not of interest in this study. Since the propane consumption in Figure 4.9 (a) did not increase over the recorded time period after oxygen shutoff, no direct propane DH was observed. Additionally, the cutoffs for propane consumption (a) and water production cutoff were at approximately the same total time from oxygen shutoff, 45 min for $4V/SiO_2$ and 75 min for $4V/18Ta/SiO_2$. This observation indicated that these behaviors were the result of the same oxygen spillover behavior. This experiment showed that the ternary $4V/18Ta/SiO_2$ catalyst had more available surface oxygen for propane ODH in comparison to $4V/SiO_2$, which may lower the rate of peroxo-vanadium formation and improve the propylene selectivity.

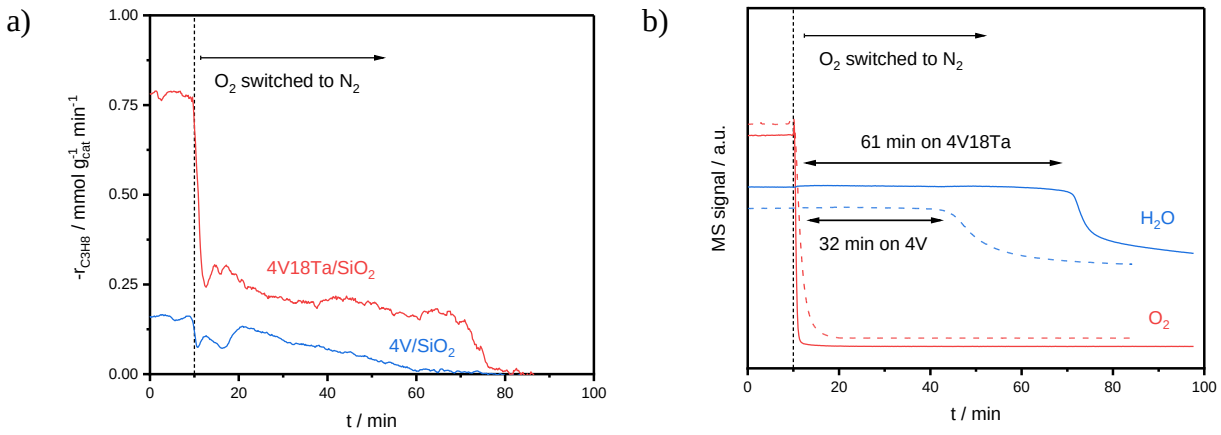

Figure 4.9 Oxygen spillover experiments shown as (a) the rate of propane consumption for $4V/SiO_2$ (blue trace) and $4V/18Ta/SiO_2$ (red trace) and (b) the MS signal of water (blue traces) and oxygen (red traces) for $4V/SiO_2$ (dotted line) and $4V/18Ta/SiO_2$ (solid line) with respect to time. Reaction conditions were 490 °C with an intel gas composition of 30% C_3H_8, 30% O_2, and the balance of Ar.

4.3.5 Reaction Mechanism

Based on the above kinetic and spectroscopic observations, the following mechanistic interpretations have been made for the ternary V/Ta/SiO_2 catalyst. (1) Dispersed vanadyl sites are the main active phase instead of the tantalum oxide phase which has a low independent selectivity. (2) Raman, XPS, XAS, and the oxygen spillover experiments show that oxygen vacancies increase with the addition of tantalum oxide. (3) ^{51}V SSNMR indicates a co-layer of vanadium oxide and tantalum oxide with proximate silanol sites. (4) The activation energy for propylene is much higher for V/Ta/SiO_2 than for V/SiO_2. Based on these observations, the tantalum oxide is likely improving the propylene selectivity by increasing the concentration of oxygen vacancies. Tantalum may be hindering propylene combustion by changing the oxygen species adjacent to vanadium. As discussed in Chapter 3, the peroxo-vanadium species activates propylene by donating an oxygen atom to the propylene to make propylene oxide (E_A = 75 kJ/mol). In contrast, the vanadyl breaks the C–H bond of propylene (E_A = 124 kJ/mol). The oxygen vacancies may be created and stabilized by the interaction between tantalum oxide and vanadium oxide species that will limit the formation of unselective peroxo-vanadium sites. The suggested mechanism is shown in Scheme 4.1 with the influence of the proposed reactions sites.

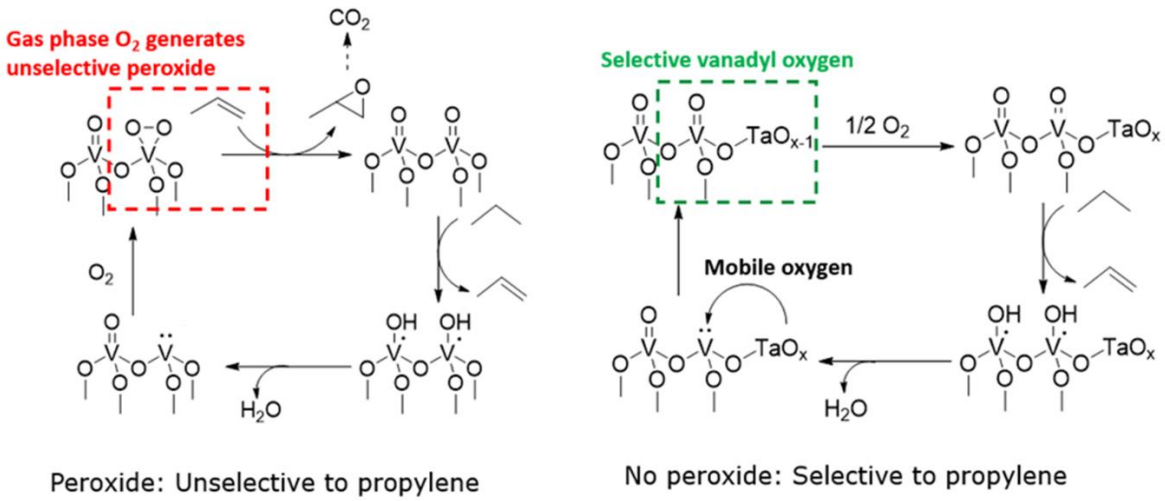

Scheme 4.1 Proposed propane ODH mechanisms comparing the activity for $4V/SiO_2$ and $4V/18Ta/SiO_2$.

4.4 Summary

In this work, silica supported vanadium and tantalum catalysts are shown to be more selective and active than silica supported vanadium catalysts. Specifically, the addition of tantalum oxide increases the activation energy of propylene combustion pathway which limits the formation of CO_x products. Reactivity experiments confirm that the tantalum oxide supported on silica is not independently responsible for the improved propylene selectivity, since Ta/SiO_2 materials do not match the selectivity of the ternary material. The general ODH mechanism of the ternary material also follows that of Mars-van Krevelen with a propane order of 1 and oxygen reaction of 0. XANES and ^{51}V SSNMR indicate a co-layer of tantalum oxide and vanadium oxide exists on the surface, and oxygen spillover experiments show that more surface oxygen is available in the ternary material compared to the vanadium supported on silica. Therefore, while the mechanism follows the same rate determining steps in a surface mechanism, the oxygen environment is modified by the presence of tantalum atoms. As a result, the vanadia forms more oligomeric

species with access to surface oxygen from TaO_x enhancing the oxidant availability for the redox cycle and limiting unselective reoxidation pathways.

To further investigate the synergy of vanadium and tantalum, computational and synthesis studies are underway. Density functional theory (DFT) studies can be used to investigate the adsorption and activation energies of propane and propylene on the ternary material. These computational studies would show the influence of individual mechanistic steps over the two metal oxides. The influence and existence of the IPA pathway have also not been thoroughly investigated in this chapter. This pathway may be a key step in understanding not only this ternary material, but also the overall ODH mechanism over vanadium-containing catalysts. Additionally, further studies can be done on the synthesis of other ternary materials that would improve the performance of vanadium to make the catalyst more efficient and economical in production and performance. For example, niobium oxide has a similar effect when applied as tantalum was in this study, and niobium is less expensive than tantalum. By finding the fundamental source of the improved performance in propane ODH, these findings can then be applied to designing the next best catalyst.

References

1. Doornkamp, C. & Ponec, V. The universal character of the Mars and Van Krevelen mechanism. *J Mol Catal A Chem* **162**, 19–32 (2000).

2. Rozanska, X., Fortrie, R. & Sauer, J. Size-Dependent Catalytic Activity of Supported Vanadium Oxide Species: Oxidative Dehydrogenation of Propane. *J Am Chem Soc* **136**, 7751–7761 (2014).

3. Rozanska, X., Fortrie, R. & Sauer, J. Oxidative Dehydrogenation of Propane by Monomeric Vanadium Oxide Sites on Silica Support. *The Journal of Physical Chemistry C* **111**, 6041–6050 (2007).

4. Sattler, J. J. H. B., Ruiz-Martinez, J., Santillan-Jimenez, E. & Weckhuysen, B. M. Catalytic dehydrogenation of light alkanes on metals and metal oxides. *Chem Rev* **114**, 10613–10653 (2014).

5. Liu, J., Mohamed, F. & Sauer, J. Selective oxidation of propene by vanadium oxide monomers supported on silica. *J Catal* **317**, 75–82 (2014).

6. Cheng, M. J., Chenoweth, K., Oxgaard, J., Van Duin, A. & Goddard, W. A. Single-site vanadyl activation, functionalization, and reoxidation reaction mechanism for propane oxidative dehydrogenation on the cubic v 4O10 cluster. *Journal of Physical Chemistry C* **111**, 5115–5127 (2007).

7. ROZANSKA, X., KONDRATENKO, E. & SAUER, J. Oxidative dehydrogenation of propane: Differences between N2O and O2 in the reoxidation of reduced vanadia sites and consequences for selectivity. *J Catal* **256**, 84–94 (2008).

8. Kim, H. Y., Lee, H. M., Pala, R. G. S., Shapovalov, V. & Metiu, H. CO oxidation by rutile TiO2(110) doped with V, W, Cr, Mo, and Mn. *Journal of Physical Chemistry C* **112**, 12398–12408 (2008).

9. Beck, B. *et al.* Partial oxidation of ethanol on vanadia catalysts on supporting oxides with different redox properties compared to propane. (2012) doi:10.1016/j.jcat.2012.09.008.

10. Moncada, J., Adams, W. R., Thakur, R., Julin, M. & Carrero, C. A. Developing a Raman Spectrokinetic Approach to Gain Insights into the Structure-Reactivity Relationship of Supported Metal Oxide Catalysts. *ACS Catal* **8**, 8976–8986 (2018).

11. Fu, T., Wang, Y., Wernbacher, A., Schlögl, R. & Trunschke, A. Single-Site Vanadyl Species Isolated within Molybdenum Oxide Monolayers in Propane Oxidation. *ACS Catal* **9**, 4875–4886 (2019).

12. Grant, J. T., Carrero, C. A., Love, A. M., Verel, R. & Hermans, I. Enhanced Two-Dimensional Dispersion of Group v Metal Oxides on Silica. *ACS Catal* **5**, 5787–5793 (2015).

13. Wachs, I. E. Catalysis science of supported vanadium oxide catalysts. *Dalton Transactions* **42**, 11762–11769 (2013).

14. Wachs, I. E., Chen, Y., Jehng, J. M., Briand, L. E. & Tanaka, T. Molecular structure and reactivity of the Group V metal oxides. *Catal Today* **78**, 13–24 (2003).

15. Carrero, C. A., Schloegl, R., Wachs, I. E. & Schomaecker, R. Critical literature review of the kinetics for the oxidative dehydrogenation of propane over well-defined supported vanadium oxide catalysts. *ACS Catal* **4**, 3357–3380 (2014).

16. Krishnan, R. R., Gopchandran, K. G., MahadevanPillai, V. P., Ganesan, V. & Sathe, V. Microstructural, optical and spectroscopic studies of laser ablated nanostructured tantalum oxide thin films. *Appl Surf Sci* **255**, 7126–7135 (2009).

17. Chen, Y., Fierro, J. L. G., Tanaka, T. & Wachs, I. E. Supported tantalum oxide catalysts: Synthesis, physical characterization, and methanol oxidation chemical probe reaction. *Journal of Physical Chemistry B* **107**, 5243–5250 (2003).

18. Lee, S. H. *et al.* Raman spectroscopic studies of amorphous vanadium oxide thin films. *Solid State Ion* **165**, 111–116 (2003).

19. Dong, S., Altvater, N. R., Mark, L. O. & Hermans, I. Assessment and comparison of ordered & non-ordered supported metal oxide catalysts for upgrading propane to propylene. *Appl Catal A Gen* **617**, 118121 (2021).

20. Jaegers, N. R. *et al.* Investigation of Silica-Supported vanadium oxide catalysts by high-field 51V magic-angle spinning NMR. *Journal of Physical Chemistry C* **121**, 6246–6254 (2017).

21. Horrocks, G. A. *et al.* Vanadium K-Edge X-ray Absorption Spectroscopy as a Probe of the Heterogeneous Lithiation of V2O5: First-Principles Modeling and Principal Component Analysis. *Journal of Physical Chemistry C* **120**, 23922–23932 (2016).

22. Chaurand, P. *et al.* New methodological approach for the vanadium K-edge X-ray absorption near-edge structure interpretation: Application to the speciation of vanadium in oxide phases from steel slag. *Journal of Physical Chemistry B* **111**, 5101–5110 (2007).

23. Wong, J., Lytle, F. W., Messmer, R. P. & Maylotte, D. H. K-edge absorption spectra of selected vanadium compounds. *Phys Rev B* **30**, 5596 (1984).

24. Keller, D. E., Koningsberger, D. C. & Weckhuysen, B. M. Elucidation of the molecular structure of hydrated vanadium oxide species by X-ray absorption spectroscopy: correlation between the V···V coordination number and distance and the point of zero charge of the support oxide. *Physical Chemistry Chemical Physics* **8**, 4814–4824 (2006).

25. Tsuchiya, T. *et al.* X-Ray absorption, photoemission spectroscopy, and Raman scattering analysis of amorphous tantalum oxide with a large extent of oxygen nonstoichiometry. *Physical Chemistry Chemical Physics* **13**, 17013–17018 (2011).

26. Carrero, C. *et al.* High performance (VOx)n–(TiOx)m/SBA-15 catalysts for the oxidative dehydrogenation of propane. *Catal Sci Technol* **4**, 786–794 (2014).

Chapter 5: Summary and Outlook

5.1 Summary

This dissertation reported on the directed synthesis of both boron-based and vanadium oxide catalysts to create defined sites and further the understanding of their roles in propane oxidative dehydrogenation (ODH). A combination of synthesis, spectroscopic characterization, kinetic studies, and computation work was applied to these catalytic systems, as illustrated in Figure 5.1.[1] The resulting observations can then be used to develop the understanding of these processes and direct the future work to improve their performance. The effective integration of the different techniques bridges the gap between execution of research techniques and developing a multidimensional understanding of the systems in question.

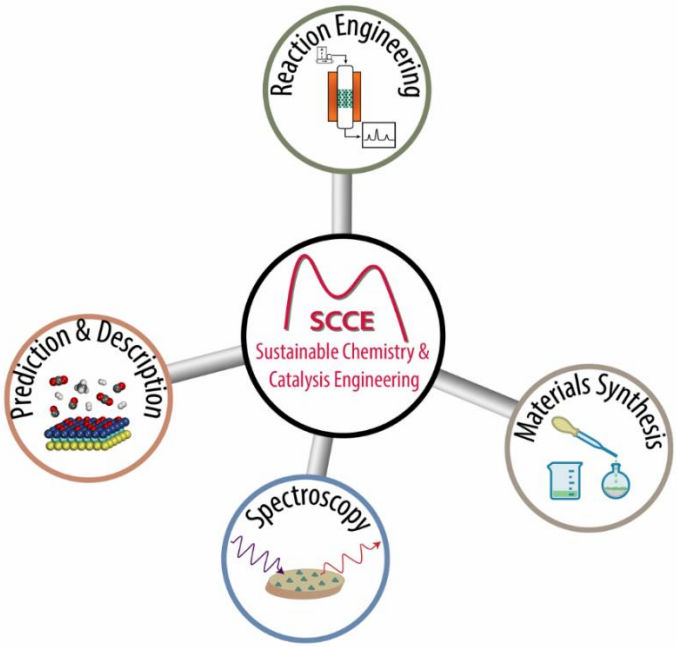

Figure 5.1 Illustration of the different branches of study that are crucial combine for understanding heterogeneous catalysis.[1]

In Chapter 2, the goal was to determine whether isolated BO_3 boron sites are active sites for propane ODH. Active boron-based catalyst had previously been shown to have an oxidized boron surface layer, and the large distribution of boron oxide (BO_x) species contains both isolated and agglomerated boron species. By using a borosilicate zeolite framework, a material with stable and isolated BO_3 sites was synthesized.[2] These sites were extensively characterized using solid-state NMR to accurately identify their structure and surrounding chemical environment. Catalytic testing showed that these isolated sites were not active for propane ODH.[3] This result showed that propane ODH does not occur over a single site, but instead the mobility and aggregated structure of BO_x sites are important to the reaction mechanism. Chapter 3 builds on the knowledge of Chapter 3 to use the well characterized borosilicate framework and apply it to the synthesis and study of vanadium oxide (VO_x) catalysts for propane ODH. Both monomeric and oligomeric VO_x catalysts were successfully synthesized in the zeolite framework. Their catalytic activities are distinct as identified through kinetic testing which confirms the importance of active site dispersion at the molecular level. The experimental results lead to the development of a computational model on the reaction mechanism. The difference in propylene selectivity over oligomeric and monomeric VO_x sites is likely due to the distinct catalytic cycles. Oligomeric sites have higher selectivity since they are able to perform hydrogen abstractions at activation energies up to 18 kJ/mol lower than isolated sites. Isolated VO_x sites preferentially go through a peroxo-vanadium surface configuration which leads to unselective formation of propylene oxide. Chapter 4 reported on the effect of tantalum oxide (TaO_x) on silica supported vanadium oxide catalysts using spectroscopic characterization and kinetic testing. Tantalum oxide improves the rate and propylene selectivity of vanadium oxide catalysts. This promotional effect appears to occur by tantalum increasing the availability of surface oxygen. The availability and mobility of surface oxygen is a

crucial component of the catalytic redox cycle. The presence of tantalum also significantly increases the activation energy of propylene likely through decreasing the concentration of the unselective peroxo-vanadium species proposed in Chapter 3.

5.2 Outlook

The results of Chapter 2 and previous works on boron literature point to the importance of a dynamic BO_x phase that forms and transforms during reaction.[4–6] In-situ and operando studies that combine spectroscopic and kinetic capabilities to see the evolution of the boron surface structures during reaction could gain insights into the active phase. Development of an operando system could reveal a wealth of knowledge on the boron oxide formation. After formation, the role and interaction of the different surface oxygenates with the gas phase oxygen are not fully known. Knowledge on these aspects of the reaction mechanism would direct catalyst development to create a more productive boron catalyst for propane ODH. Synthesis based studies could then focus on tailoring the boron structure to form the most active sites in the most economical way possible. Activated carbon supports have already been shown as active and inexpensive for propane ODH.[7] Encapsulation synthesis method could also be applied using mesoporous or similarly structured materials to capitalize on the unique active phase formed no boron materials. For example, h-BN monolith materials have already been shown as efficient materials for propane ODH.[8]

Chapters 3 and 4 developed the mechanistic understanding of supported vanadium oxide catalysts. The pathway to isopropyl alcohol was proposed in Chapter 3. Further investigation into the validity of this pathway and its potential influence on the reaction mechanism is needed. The addition of an efficient IPA dehydration material to the vanadium catalyst could improve the overall catalytic performance. More synthesis and kinetic experiments are needed to investigate this area. The existence of peroxo-vanadium pathway is not a new to vanadium literature.[9] Here

computational results showed the influenced of the peroxo- species in monomeric and isolated models. In the ternary catalyst with VO_x and TaO_x on silica, the tantalum was proposed to limit the peroxo-vanadium species to improve the propylene selectivity. Computational modeling for this pathway on the ternary catalyst is currently under way to support or refute the peroxo-vanadium theory. Chapter 4 also proposed that TaO_x species improve the surface oxygen availability for vanadium reoxidation. This theory is also under investigation using DFT calculations. Finally, it will be important to broaden the scope of what additives are tested for ternary vanadium oxide catalysts. Chapter 4 showed that the addition of Ta or Nb to supported vanadium oxide improved catalytic performance. These are materials that change the acidity and redox ability of the catalyst surface. If the influence of surface acidity can be determined without significantly impacting redox ability and vice versa, a better vanadium catalyst can be designed by taking the best aspects of each additive. Verification or contradiction of the above-described ideas will provide the next step in understanding the vanadium catalyzed ODH mechanism. The future directions are summarized in the list below as questions for research directions.

1. Through what pathways does boron oxide on an active catalyst form and which is the most efficient?
2. Can the formation of the oxyfunctionalized boron surface be optimized through controlled synthesis of boron materials?
3. Can the addition of an isopropyl alcohol dehydrogenation active material be added to a vanadium oxide based catalyst to improve its performance in propane ODH?
4. What is the role of peroxo-vanadium species in the catalytic cycle of ternary $V/Ta/SiO_2$ catalysts for propane ODH?

5. Can a non-redox additive positively influence the reactivity of vanadium oxide ODH catalysts?

The insights gained in this dissertation have opened direction for future research to build upon the findings shown here and lead to further advancements in the field of oxidative dehydrogenation of propane.

References

1. Research | Hermans Research Group. https://hermans.chem.wisc.edu/research.
2. Altvater, N. R. *et al.* B-MWW Zeolite: The Case Against Single-Site Catalysis. *Angewandte Chemie - International Edition* **59**, 6546–6550 (2020).
3. Dorn, R. W. *et al.* Structure Determination of Boron-Based Oxidative Dehydrogenation Heterogeneous Catalysts With Ultrahigh Field 35.2 T 11 B Solid-State NMR Spectroscopy. *ACS Catal* **10**, 13852–13866 (2020).
4. Love, A. M. *et al.* Probing the Transformation of Boron Nitride Catalysts under Oxidative Dehydrogenation Conditions. *J Am Chem Soc* **141**, 182–190 (2019).
5. Love, A. M. *et al.* Synthesis and Characterization of Silica-Supported Boron Oxide Catalysts for the Oxidative Dehydrogenation of Propane. *Journal of Physical Chemistry C* **123**, 27000–27011 (2019).
6. Zhang, Z., Jimenez-Izal, E., Hermans, I. & Alexandrova, A. N. Dynamic Phase Diagram of Catalytic Surface of Hexagonal Boron Nitride under Conditions of Oxidative Dehydrogenation of Propane. *Journal of Physical Chemistry Letters* **10**, 20–25 (2019).
7. Mark, L. O. *et al.* Highly Selective Carbon-Supported Boron for Oxidative Dehydrogenation of Propane. *ChemCatChem* **13**, 3611–3618 (2021).
8. Agbi, T. *et al.* 3D-Printed Boron Nitride Catalytic Monoliths for Oxidative Dehydrogenation of Propane. *Top Catal* **1**, 1–9 (2023).
9. Molinari, J. E. & Wachs, I. E. Presence of surface vanadium peroxo-oxo umbrella structures in supported vanadium oxide catalysts: Fact or fiction? *J Am Chem Soc* **132**, 12559–12561 (2010).

Appendix A: Supporting information for Chapter 2

All experimental parameters for the following figures can by found in the following reference.[1,2]

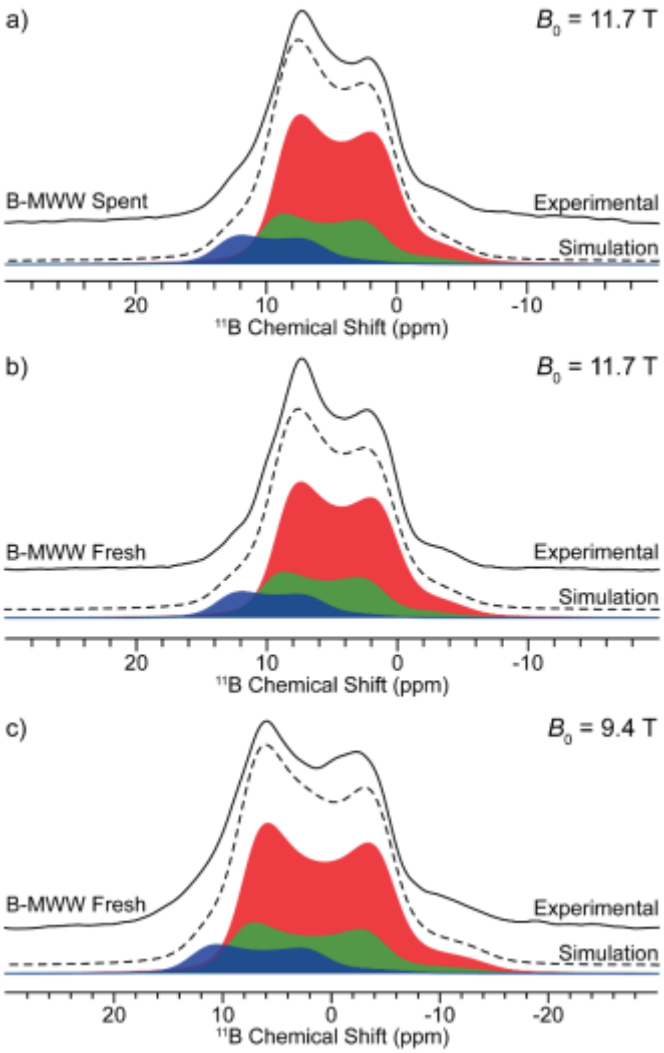

Figure A.1 Comparison of 1D ^{11}B MAS SSNMR spectra of Fresh and Spent B-MWW at different magnetic fields of 9.4 T and 11.7 T as labeled. The solid lines are experimental spectra, and the dotted lines are the simulated spectra made up of the individually shaded sites.

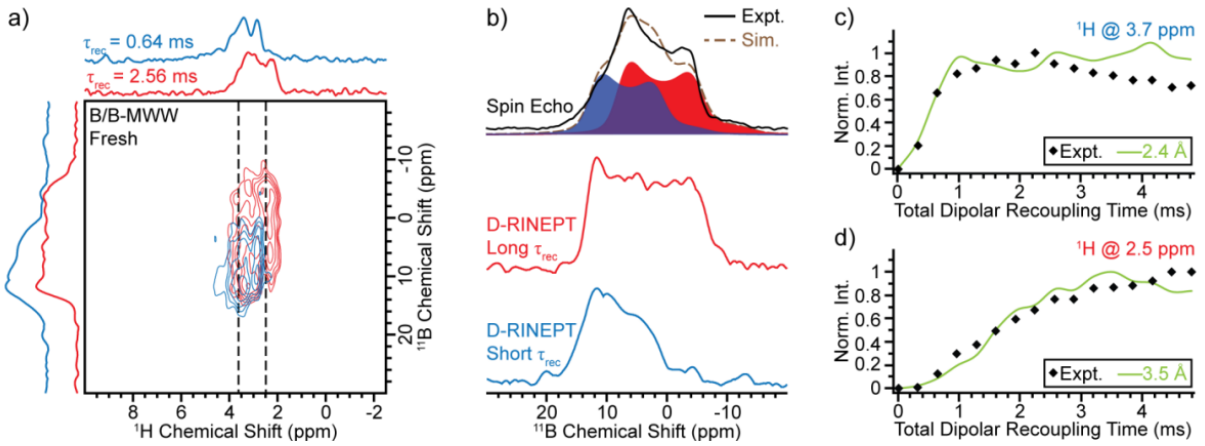

Figure A.2 (a) 2D $^{11}B \rightarrow {}^{1}H$ D-RINEPT spectra of fresh B/B-MWW acquired with 0.64 ms and 2.56 ms (blue and red respectively) of heteronuclear dipolar recoupling time. (b) The black solid line is the 1D ^{11}B spin echo NMR spectrum. The red and blue traces are the projections for the 2D $^{11}B \rightarrow {}^{1}H$ D-RINEPT spectra taken with 0.64 ms and 2.54 ms (blue and red respectively) of total heteronuclear dipolar recoupling time. The dashed lines in (a) correspond to the dipolar recoupling buildup curves for the ^{1}H slices at (c) 3.7 ppm and (d) 2.5 ppm. The solid lines are the numerical SIMPSON simulations for the experimental points (black diamonds). The simulations for heteronuclear dipolar couplings correspond to the $^{1}H - {}^{1}B$ inter-nuclear distances. Spectra were recorded at 9.4 T with 25 kHz MAS.

Table A.2 ^{11}B parameters for the analytical simulations for the B-MWW, fresh B/SiO_2, and spent B/SiO_2. All fits have C_Q = 2.5 MHz and η = 0.

Catalyst	D_{iso} (^{11}B) (ppm)	Population (%)
B-MWW	10.7	32.5
	12.0	16.7
	13.0	19.0
	13.8	11.1
	15.2	10.2
	16.8	5.4
	18.2	5.1
Fresh B/SiO_2	9.4	8.9
	10.8	20.4
	12.1	12.5
	13.7	30.0
	15.5	13.5
	16.7	12.0
	18.2	2.7
Spent B/SiO_2	8.9	8.5
	10.3	22.6
	11.5	18.9
	12.9	16.0
	13.8	15.3
	15.2	9.2
	16.6	9.5

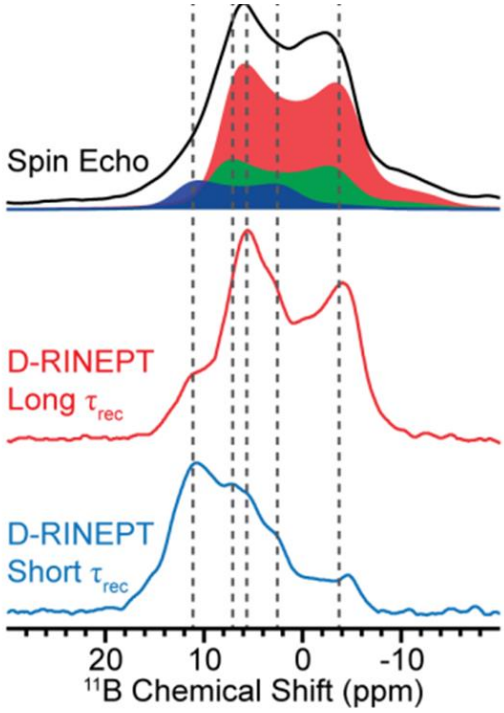

Figure A.3 Top black trace is a ^{11}B spin echo NMR of B-MWW. The red and blue traces are the 2D $^{11}B \rightarrow ^{1}H$ D-RINEPT spectra projections taken at 0.64 ms and 2.56 ms of total recoupling time (blue and red respectively). The dashed lines show that the horns of the shaded simulated sites match the horns of the blue and red projections. All spectra were recorded at 9.4 T with 25 kHz MAS.

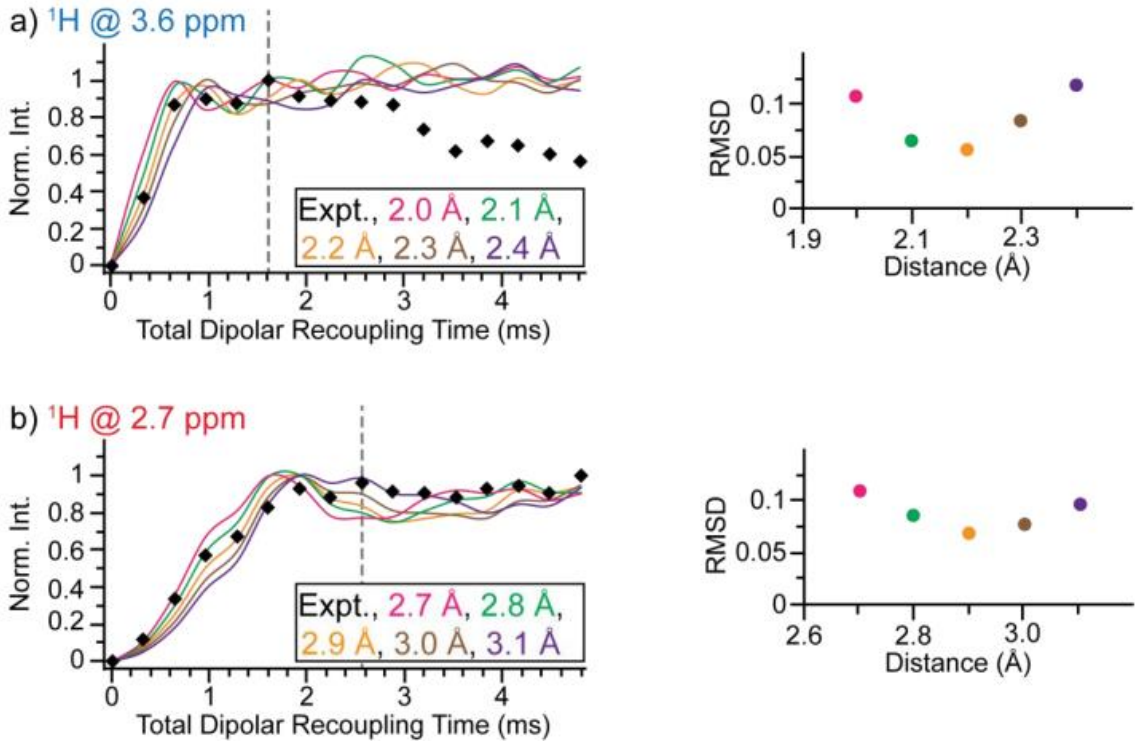

Figure A.4 2D $^{11}B \rightarrow {}^{1}H$ D-RINEPT dipolar recoupling buildup curves for the ^{1}H spectra at (a) 3.6 ppm and (b) 2.7 ppm. The corresponding RMSD plots for the numerical simulations with different internuclear distances. The solid lines are the different numerical SIMPSON simulations for the experimental points (black diamonds). The grey line is the duration of heteronuclear dipolar recoupling used for calculating the RMSD plots. For (a) used points from 0 to 1.6 ms and (b) used points from 0 to 2.56 ms.

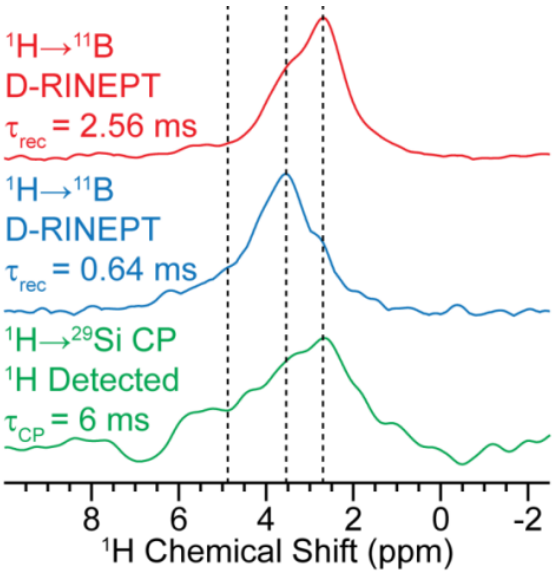

Figure A.5 Spectra of B-MWW fresh spectra for $^{1}H\{^{29}Si\}$ CPMAS (green) and the proton projections from the 2D $^{11}B \rightarrow ^{1}H$ D-RINEPT spectra acquired with 0.64 ms (blue) and 2.56 ms (red) of total heteronuclear dipolar recoupling time.

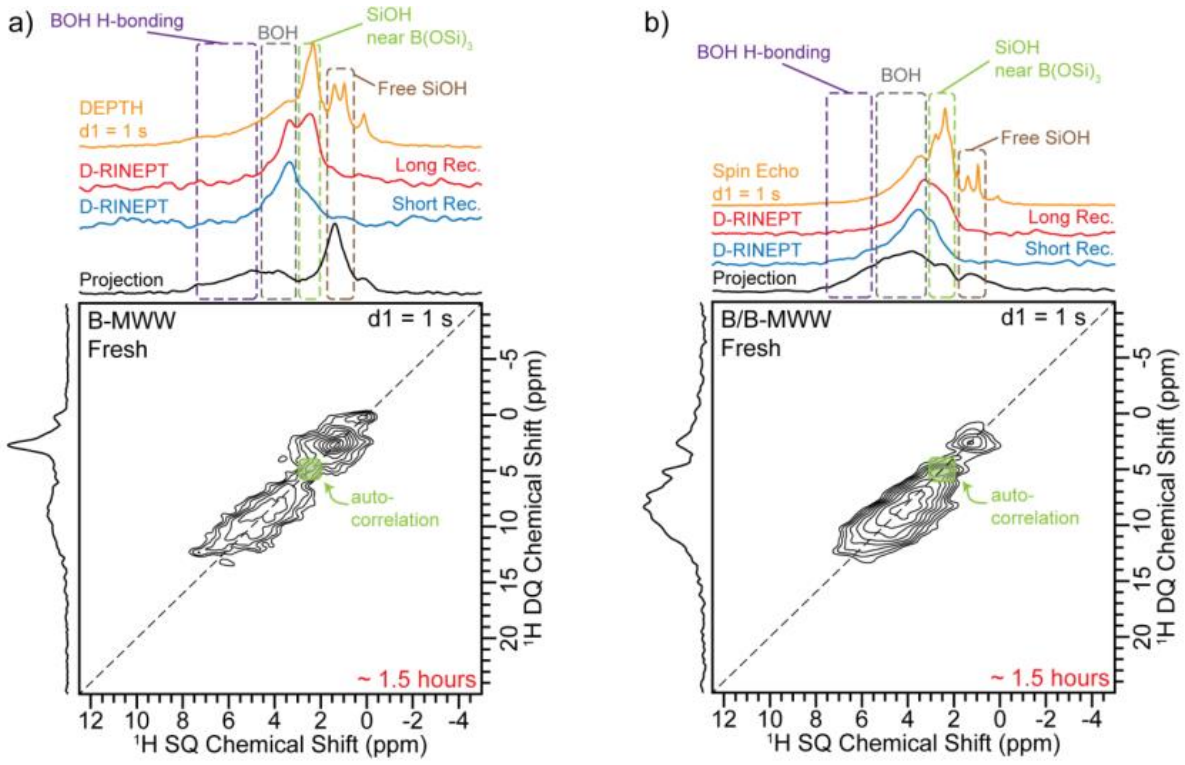

Figure A.6 ^{1}H DQ-SQ spectra of (a) B-MWW and (b) B/B-MWW. Spectra were acquired at 9.4 T with 25 kHz MAS. ^{1}H spin echo spectra and ^{11}B → ^{1}H D-RINEPT projections are shown above the DQ-SQ projections to better illustrate the shift regions.

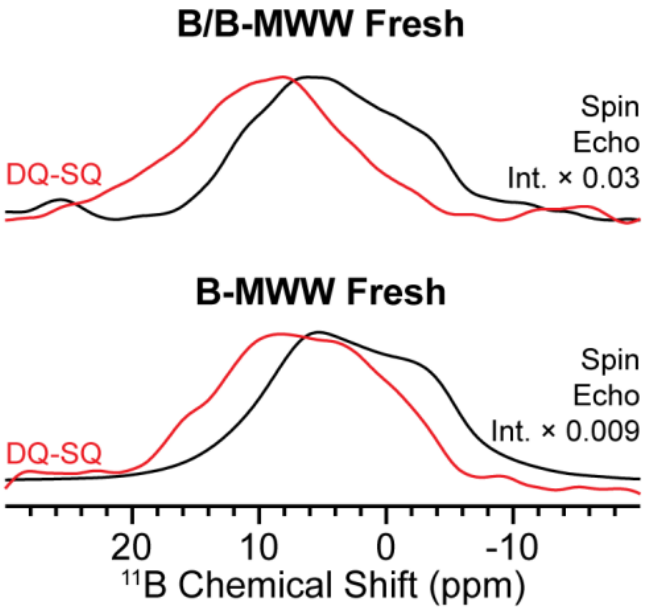

Figure A.7 1D ^{11}B dipolar double-quantum-single-quantum (DQ-SQ) in red and ^{11}B spin echo spectra in black of B/B-MWW and B-MWW. The black traces were scaled to match the DQ-SQ spectra, and the scaling factor is shown on the figure. All spectra were acquired at 9.4 T with 25 kHz MAS.

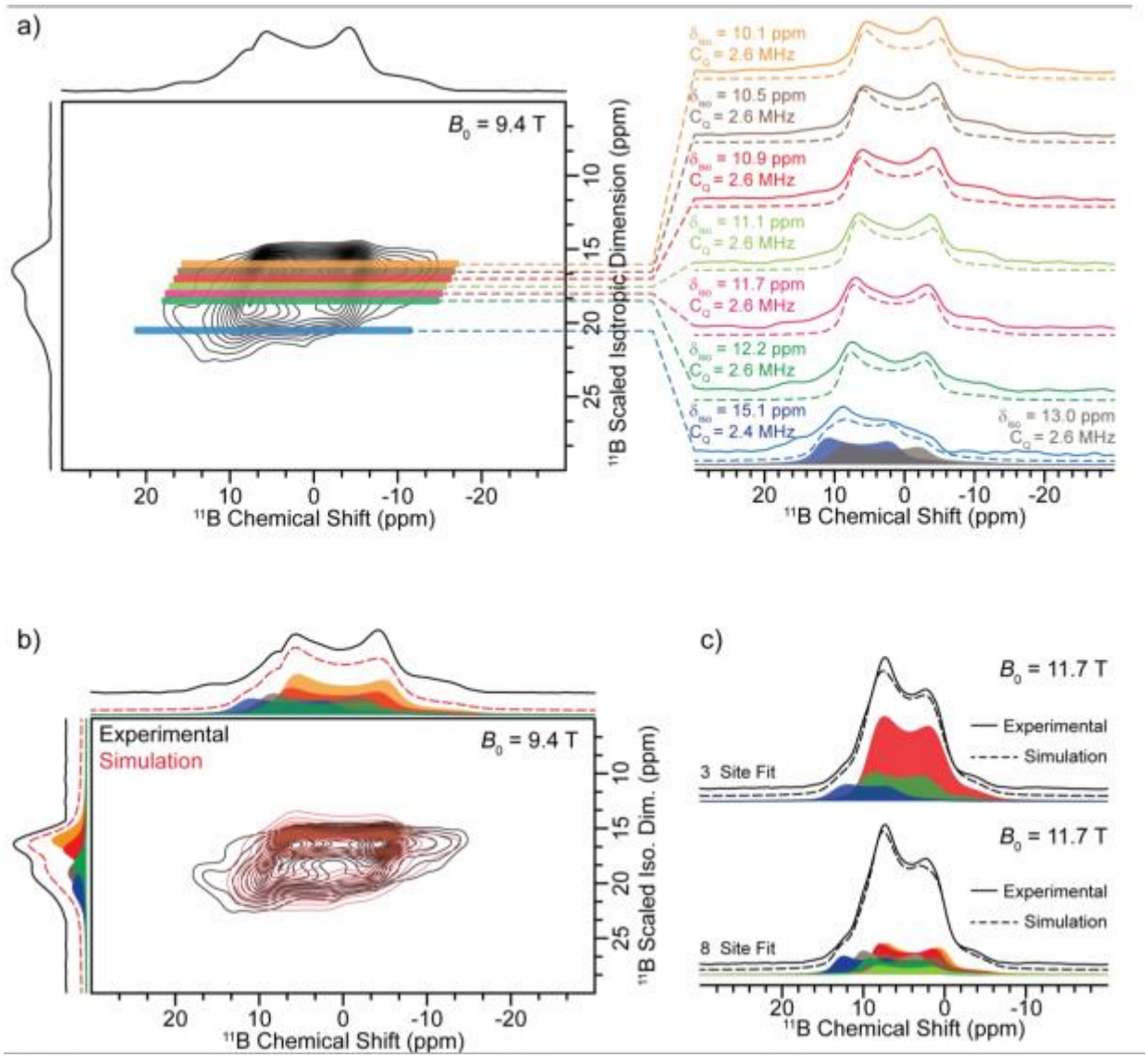

Figure A.8 (a) 2D ^{11}B triple-quantum MQMAS spectrum of B-MWW recorded at 9.4 T with 25 kHz MAS. Slices were from the indirect dimension for determining the ^{11}B chemical shift and quadrupolar coupling constant. The asymmetry parameter (η) was 0 for all fits. (b) Simulated ^{11}B MQMAS laid over the experimental spectrum. (c) Comparison of the ^{11}B analytical simulations using three sites and eight sites (as shown in a). Both simulations match well to the experimental spectrum and illustrate the distribution in the ^{11}B shift as expected.

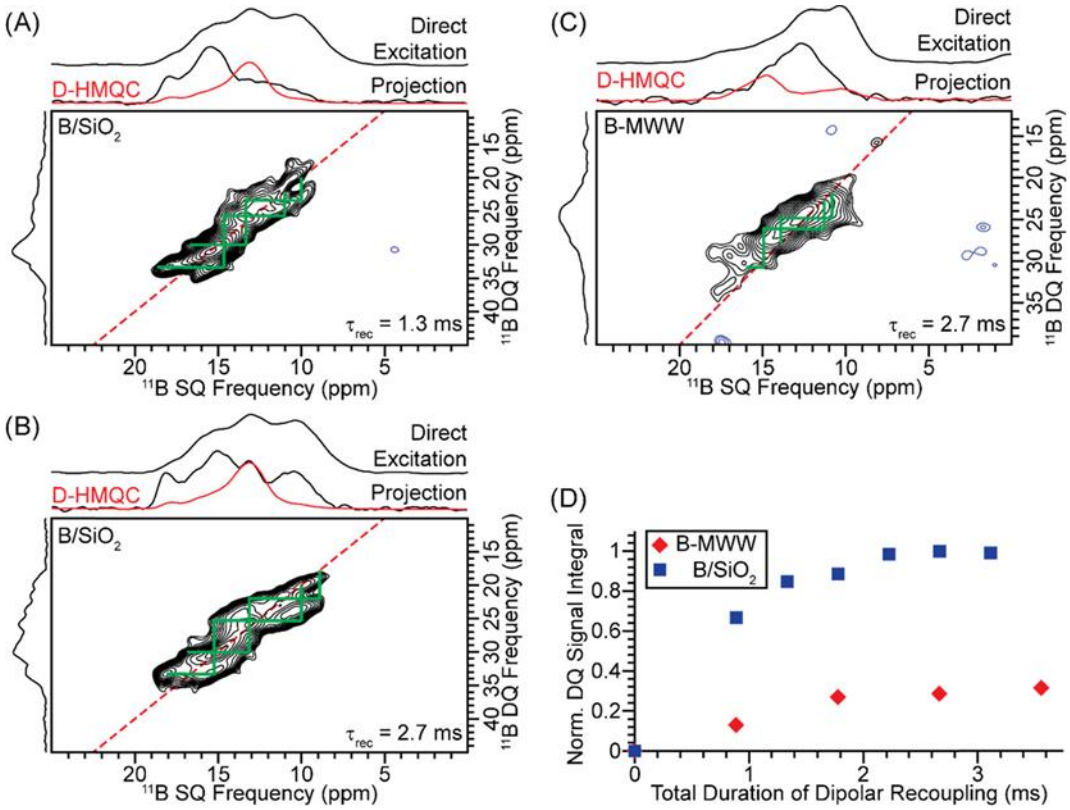

Figure A.9 2D ^{11}B dipolar DQ-SQ NMR spectra of (a, b) B/SiO_2 and (c) B-MWW recorded at 35.2 T with 18 kHz MAS and 1.3 ms (a) or 2.7 ms (b, c) of total homonuclear dipolar recoupling time. The 1D direct excitation ^{11}B is the black trace and $^{11}B\{^1H\}$ D-HMQC NMR is the red trace. Both are overlaid above the 2D SQ projections. The green lines show the boron species correlations, and the dashed red lines show the autocorrelation. The normalized 1D ^{11}B DQ-SQ (d) integration is plotted as a function of the total homonuclear dipolar recouping time duration for B-MWW and B/SiO_2 as indicated.

References

1. Altvater, N. R. *et al.* B-MWW Zeolite: The Case Against Single-Site Catalysis. *Angewandte Chemie - International Edition* **59**, 6546–6550 (2020).

2. Dorn, R. W. *et al.* Structure Determination of Boron-Based Oxidative Dehydrogenation Heterogeneous Catalysts With Ultrahigh Field 35.2 T 11 B Solid-State NMR Spectroscopy. *ACS Catal* **10**, 13852–13866 (2020).

Appendix B: Supporting information for Chapter 3

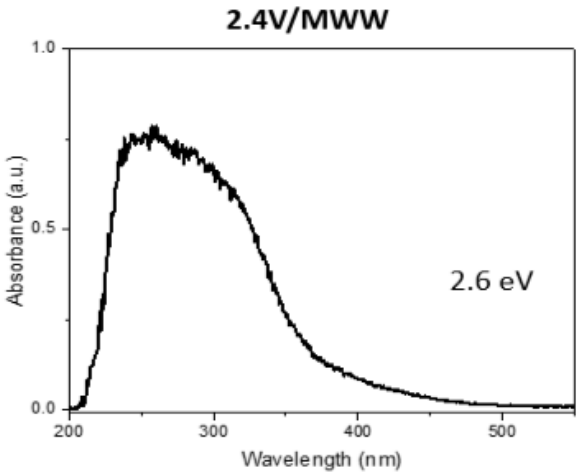

Figure B.1 Diffuse reflectance ultraviolet visible spectra of 2.4V-MWW. The edge energy is 2.6 eV at the shoulder above 400 nm indicating the presence of some V_2O_5 which is consistent with Raman measurements.

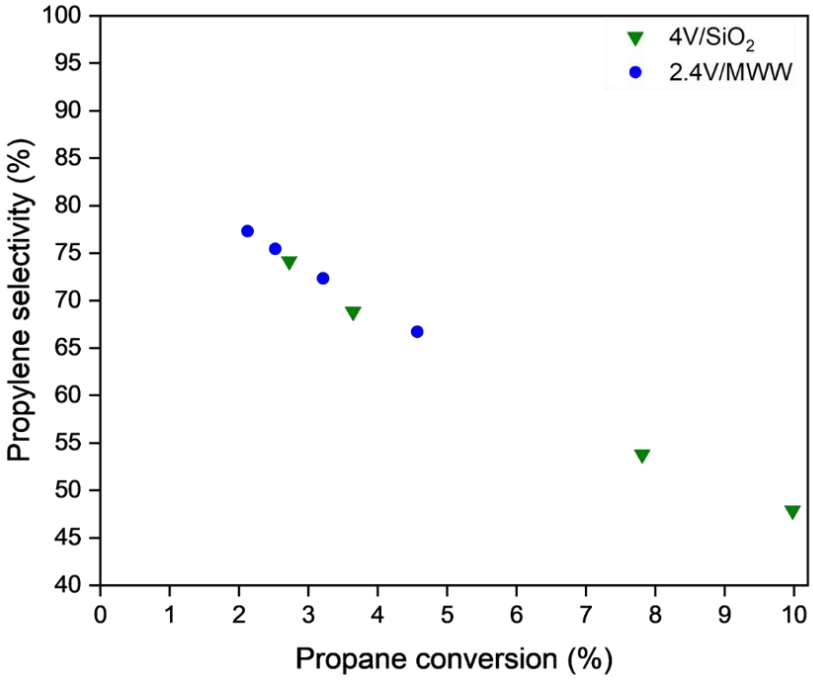

Figure B.2 Propane selectivity as a function of conversion for 2.4V-MWW and 4V/SiO_2. Propane ODH results collected at 500 °C with 30% C_3H_8, 15% O_2, and the balance of N_2 with 50-100 mg of catalyst.

Appendix C: Supporting information for Chapter 4

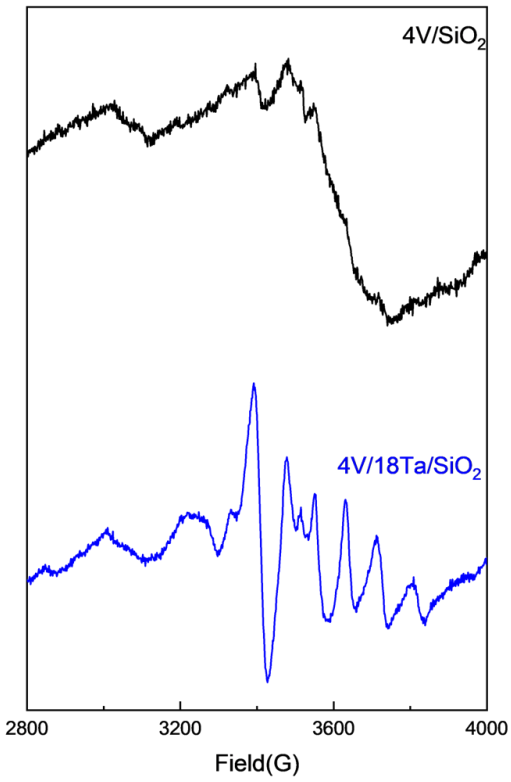

Figure C.1 EPR spectra of $4V/SiO_2$ and $4V/18Ta/SiO_2$ taken after material was dehydrated at 120 °C under vacuum.

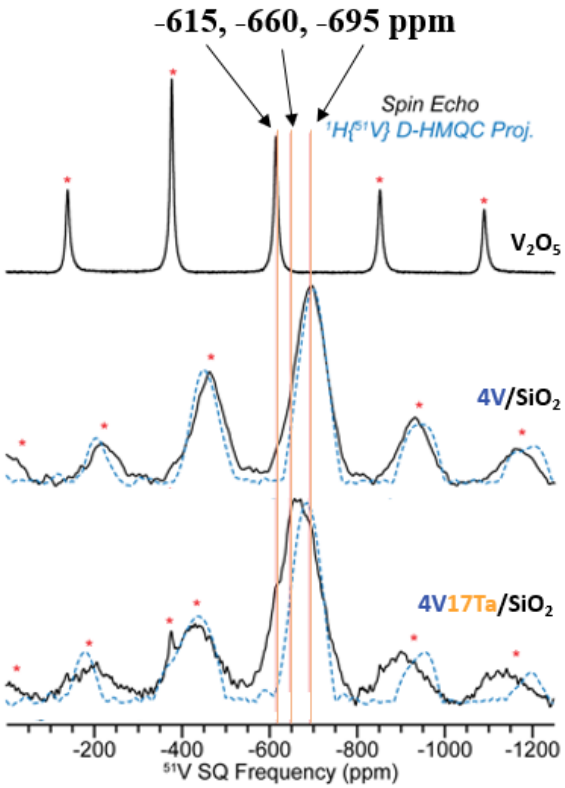

Figure C.2 ^{51}V SSNMR spin echo (black trace) and ^{1}H{^{51}V} D-HMQC projection (blue dotted trace) of 4V/SiO_2, 4V/18Ta/SiO_2, and V_2O_5. Vanadium materials were dehydrated at 500 °C prior to measurement. Samples were measured at 25 kHz on a 9.4 T instrument. Sidebands are marked with a red star and are not true peaks.

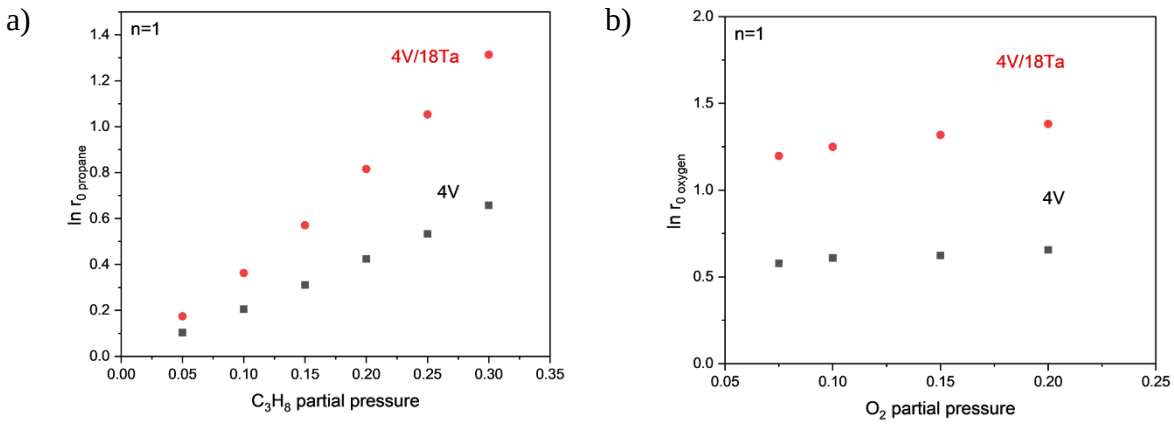

Figure C.3 (a) reaction order of propane measured as a function of propane partial pressure at constant oxygen partial pressure, and (b) reaction order of oxygen measured as a function of oxygen partial pressure at constant propane partial pressure. Rates were measured at 500 °C with 50-100 mg of catalyst.